

AFRL-PR-WP-TR-2004-2027

**SCIENTIFIC RESEARCH IN
AIRCRAFT
MECHANICAL/THERMAL
TECHNOLOGY**



Dr. Scott K. Thomas, Dr. Kirk L. Yerkes, R. Michael Castle, Richard C. Lykins, Joel T. Lauer, Jonathon P. Kuhns, Travis E. Michalak, and Zachary J. Osborn

**Wright State University
Department of Mechanical and Materials Engineering
3640 Colonel Glenn Highway
Dayton, OH 45435-0001**

DECEMBER 2003

Final Report for 21 August 1998 – 20 August 2003

Approved for public release; distribution is unlimited.

STINFO FINAL REPORT

**PROPULSION DIRECTORATE
AIR FORCE MATERIEL COMMAND
AIR FORCE RESEARCH LABORATORY
WRIGHT-PATTERSON AIR FORCE BASE, OH 45433-7251**

20040427 168

NOTICE

USING GOVERNMENT DRAWINGS, SPECIFICATIONS, OR OTHER DATA INCLUDED IN THIS DOCUMENT FOR ANY PURPOSE OTHER THAN GOVERNMENT PROCUREMENT DOES NOT IN ANY WAY OBLIGATE THE U.S. GOVERNMENT. THE FACT THAT THE GOVERNMENT FORMULATED OR SUPPLIED THE DRAWINGS, SPECIFICATIONS, OR OTHER DATA DOES NOT LICENSE THE HOLDER OR ANY OTHER PERSON OR CORPORATION; OR CONVEY ANY RIGHTS OR PERMISSION TO MANUFACTURE, USE, OR SELL ANY PATENTED INVENTION THAT MAY RELATE TO THEM.

THIS REPORT IS RELEASABLE TO THE NATIONAL TECHNICAL INFORMATION SERVICE (NTIS). AT NTIS, IT WILL BE AVAILABLE TO THE GENERAL PUBLIC, INCLUDING FOREIGN NATIONS.

THIS TECHNICAL REPORT HAS BEEN REVIEWED AND IS APPROVED FOR PUBLICATION.

/s/

KIRK L. YERKES
Project Engineer
Energy Storage & Thermal Sciences Branch

/s/

JOHN K. ERBACHER
Acting Chief
Energy Storage & Thermal Sciences Branch

/s/

CYNTHIA A. OBRINGER
Deputy Chief
Power Division

Do not return copies of this report unless contractual obligations or notice on a specific document require its return.

REPORT DOCUMENTATION PAGE					<i>Form Approved</i> OMB No. 0704-0188	
The public reporting burden for this collection of information is estimated to average 1 hour per response, including the time for reviewing instructions, searching existing data sources, gathering and maintaining the data needed, and completing and reviewing the collection of information. Send comments regarding this burden estimate or any other aspect of this collection of information, including suggestions for reducing this burden, to Department of Defense, Washington Headquarters Services, Directorate for Information Operations and Reports (0704-0188), 1215 Jefferson Davis Highway, Suite 1204, Arlington, VA 22202-4302. Respondents should be aware that notwithstanding any other provision of law, no person shall be subject to any penalty for failing to comply with a collection of information if it does not display a currently valid OMB control number. PLEASE DO NOT RETURN YOUR FORM TO THE ABOVE ADDRESS.						
1. REPORT DATE (DD-MM-YY) December 2003		2. REPORT TYPE Final		3. DATES COVERED (From - To) 08/21/1998 – 08/20/2003		
4. TITLE AND SUBTITLE SCIENTIFIC RESEARCH IN AIRCRAFT MECHANICAL/THERMAL TECHNOLOGY				5a. CONTRACT NUMBER F33615-98-1-2844		
				5b. GRANT NUMBER		
				5c. PROGRAM ELEMENT NUMBER 62203F		
6. AUTHOR(S) Dr. Scott K. Thomas, Dr. Kirk L. Yerkes, R. Michael Castle, Richard C. Lykins, Joel T. Lauer, Jonathon P. Kuhns, Travis E. Michalak, and Zachary J. Osborn				5d. PROJECT NUMBER 3145		
				5e. TASK NUMBER 20		
				5f. WORK UNIT NUMBER C5		
7. PERFORMING ORGANIZATION NAME(S) AND ADDRESS(ES) Wright State University Department of Mechanical and Materials Engineering 3640 Colonel Glenn Highway Dayton, OH 45435-0001				8. PERFORMING ORGANIZATION REPORT NUMBER		
9. SPONSORING/MONITORING AGENCY NAME(S) AND ADDRESS(ES) Propulsion Directorate Air Force Research Laboratory Air Force Materiel Command Wright-Patterson AFB, OH 45433-7251				10. SPONSORING/MONITORING AGENCY ACRONYM(S) AFRL/PRPS		
				11. SPONSORING/MONITORING AGENCY REPORT NUMBER(S) AFRL-PR-WP-TR-2004-2027		
12. DISTRIBUTION/AVAILABILITY STATEMENT Approved for public release; distribution is unlimited.						
13. SUPPLEMENTARY NOTES						
14. ABSTRACT <p>This final report describes the progress to date on six individual projects. "The Effect of Working Fluid Inventory on Performance of Revolving Helically-Grooved Heat Pipes" is related to an experimental analysis of working fluid inventory and its effects on the capillary limit of grooved heat pipes. "Fully-Developed Laminar Flow in Trapezoidal Grooves with Shear Stress at the Liquid-Vapor Interface" concerns the effects of geometry and interfacial shear stress on the pressure drop in trapezoidal grooves. "Fully-Developed Laminar Flow in Sinusoidal Grooves" is similar to the above, except that the sinusoidal grooves typically seen in micro-etching are examined. "Micro Capillary Pumped Loop Testing" deals with the design, manufacture and calibration of an experimental facility for testing capillary pumped loops embedded in silicon wafers. "Design and Testing of a Thermodynamic Filling Station for Miniature Heat Pipes" concerns a novel filling procedure for miniature heat pipes. "Acceleration Testing of Three Raytheon Heat Pipes using the AFRL/PRPS Centrifuge Table" deals with the performance of heat pipes under various acceleration conditions, which were imposed by the centrifuge table located in Bldg. 71-B H-Bay in Area B of Wright-Patterson AFB.</p>						
15. SUBJECT TERMS Micro capillary pumped loop, heat pipe fill station, centrifugal testing, heat pipe analysis, flow of liquid in grooves						
16. SECURITY CLASSIFICATION OF:			17. LIMITATION OF ABSTRACT: SAR	18. NUMBER OF PAGES 166	19a. NAME OF RESPONSIBLE PERSON (Monitor) Dr. Kirk L. Yerkes	
a. REPORT Unclassified	b. ABSTRACT Unclassified	c. THIS PAGE Unclassified			19b. TELEPHONE NUMBER (Include Area Code) (937) 255-5721	

Contents

1	The Effect of Working Fluid Inventory on the Performance of Revolving Helically-Grooved Heat Pipes	1
1.1	Abstract	1
1.2	Introduction	1
1.3	Determination of Heat Pipe Working Fluid Inventory	4
1.4	Heat Pipe Filling Station	9
1.5	Experimental Setup	10
1.6	Results and Discussion	13
1.7	Conclusions	16
1.8	Nomenclature	16
1.9	References	18
2	Fully-Developed Laminar Flow in Trapezoidal Grooves with Shear Stress at the Liquid-Vapor Interface	34
2.1	Abstract	34
2.2	Introduction	34
2.3	Mathematical Model	38
2.4	Numerical Model	39
2.5	Results and Discussion	41
2.5.1	Parametric Analysis	41
2.5.2	Semi-Analytical and Two-Point Numerical Solutions for \bar{v}^*	43
2.5.3	Effect of Groove Fill Ratio	44
2.5.4	Capillary Limit Analysis for a Revolving Helically-Grooved Heat Pipe	46
2.6	Conclusions	49
2.7	Nomenclature	50
3	Fully-Developed Laminar Flow in Sinusoidal Grooves	71
3.1	Abstract	71
3.2	Introduction	71

3.3	Mathematical Model	72
3.4	Numerical Model	74
3.5	Results and Discussion	75
3.6	Semi-Analytical Solution for $\overline{v^*}$	75
3.7	Conclusions	79
3.8	Nomenclature	79
3.9	References	81
3.10	Appendix	82
3.10.1	Equation of the circular meniscus	82
3.10.2	Determination of the maximum meniscus contact angle	85
3.10.3	Determination of the hydraulic diameter	86
4	Micro Capillary Pumped Loop Testing	97
4.1	Abstract	97
4.2	Experimental Setup	97
4.2.1	Calibration	100
4.2.2	Uncertainty Analysis	104
4.3	Summary and Future Work	105
4.4	Nomenclature	110
5	Design and Testing of a Thermodynamic Filling Station for Miniature Heat Pipes	119
5.1	Abstract	119
5.2	Introduction	119
5.3	Analytical Model	121
5.4	Experimental Setup	123
5.5	Results and Discussion	124
5.6	Conclusions and Future Directions	125
5.7	References	125
5.8	Nomenclature	126

6 Acceleration Testing of Three Raytheon Heat Pipes using the AFRL/PRPS Centrifuge Table	132
6.1 Abstract	132
6.2 Experimental Setup	132
6.3 Experimental Procedure	134
6.4 Results and Discussion	136
6.5 Conclusions	138

List of Figures

1 Photomicrograph of the helical groove geometry.	20
2 Schematic of the helical pitch measurement technique: (a) Major components; (b) Cross-sectional view of sprung pin engaging a helical groove.	21
3 Specific volume of ethanol versus temperature: (a) Saturated liquid; (b) Saturated vapor.	22
4 Schematic of the heat pipe filling station.	23
5 Thermocouple locations and relevant lengths.	24
6 Steady-state temperature distributions for $ \vec{a}_r = 0.01\text{-g}$, $G = 1.0$: (a) Inboard; (b) Outboard; (c) Top; (d) Bottom.	25
7 Thermal resistance versus heat transport: (a) $G = 0.5$; (b) $G = 1.0$; (c) $G = 1.5$	26
8 Capillary limit versus radial acceleration comparison of present model and Thomas et al. (1998).	27
9 Comparison of present model and experimental capillary limit data versus radial acceleration: (a) $G = 0.5$; (b) $G = 1.0$; (c) $G = 1.5$	28
10 Temperatures within the evaporator section versus transported heat for $ \vec{a}_r = 0.01\text{-g}$: (a) $x = 54.0\text{ mm}$; (b) $x = 92.1\text{ mm}$; (c) $x = 130\text{ mm}$; (d) $x = 168\text{ mm}$	29
11 Temperatures within the evaporator section versus transported heat for $ \vec{a}_r = 10.0\text{-g}$: (a) $x = 54.0\text{ mm}$; (b) $x = 92.1\text{ mm}$; (c) $x = 130\text{ mm}$; (d) $x = 168\text{ mm}$	30

12	Heat transfer coefficients within the evaporator section versus transported heat for $ \vec{a}_r = 0.01\text{-g}$: (a) $x = 54.0$ mm; (b) $x = 92.1$ mm; (c) $x = 130$ mm; (d) $x = 168$ mm.	31
13	Heat transfer coefficients within the evaporator section versus transported heat for $ \vec{a}_r = 10.0\text{-g}$: (a) $x = 54.0$ mm; (b) $x = 92.1$ mm; (c) $x = 130$ mm; (d) $x = 168$ mm.	32
14	Ratio of liquid volume to total groove volume versus saturation temperature.	33
15	Flow of liquid in a trapezoidal groove: (a) Coordinate system; (b) Solution domain.	56
16	Dimensionless velocity fields for laminar flow in trapezoidal grooves ($\beta = 1.0$, $\phi = 10^\circ$, $\theta = 45^\circ$): (a) $\tau_{lv}^* = 5.0$ (cocurrent flow); (b) $\tau_{lv}^* = 0.0$; (c) $\tau_{lv}^* = -0.1$ (countercurrent flow).	57
17	\overline{v}^* versus τ_{lv}^* for laminar flow in trapezoidal grooves ($\beta = 1.0$): (a) $\theta = 0^\circ$; (b) $\theta = 30^\circ$; (c) $\theta = 60^\circ$	58
18	Po versus τ_{lv}^* for laminar flow in trapezoidal grooves ($\beta = 1.0$): (a) $\theta = 0^\circ$; (b) $\theta = 30^\circ$; (c) $\theta = 60^\circ$	59
19	\dot{V}^* versus τ_{lv}^* for laminar flow in trapezoidal grooves ($\beta = 1.0$): (a) $\theta = 0^\circ$; (b) $\theta = 30^\circ$; (c) $\theta = 60^\circ$	60
20	\overline{v}^* versus τ_{lv}^* for laminar flow in trapezoidal grooves ($\phi = 30^\circ$): (a) $\theta = 0^\circ$; (b) $\theta = 30^\circ$; (c) $\theta = 60^\circ$	61
21	\overline{v}^* , Po and \dot{V}^* versus θ for laminar flow in trapezoidal grooves ($\phi = 30^\circ$, $\tau_{lv}^* = 5.0$).	62
22	\overline{v}^* , Po and \dot{V}^* versus θ for laminar flow in trapezoidal grooves ($\beta = 1.0$, $\tau_{lv}^* = 5.0$).	63
23	Semi-analytical and two-point numerical solutions for \overline{v}^* : (a) Definition of parameters; (b) Force balance on the liquid in a trapezoidal groove.	64
24	Numerical and semi-analytical solution comparison: (a) $-\tau_{lv,0}^*$ versus ϕ for $\beta = 1.0$ (from Fig. 17); (b) $-\tau_{lv,0}^*$ versus β for $\phi = 30^\circ$ (from Fig. 20); (c) Normalized mean velocity versus normalized shear stress at the liquid-vapor interface (from Figs. 17 and 20).	65

25	Effect of groove fill ratio on liquid flowing in a trapezoidal groove: (a) Parametric analysis (to scale, $h = 0.03831$ cm, $w = 0.03445$ cm, $\theta = 14.62^\circ$); (b) Definition of variables prior to bifurcation of the liquid; (c) Definition of variables after bifurcation of the liquid.	66
26	Effect of groove fill ratio: (a) Radius of curvature of the liquid-vapor interface; (b) Mean velocity parameter; (c) Volumetric flow rate parameter.	67
27	Maximum heat transport predicted by the closed-form solution versus groove fill ratio (Straight axial grooves, no body forces, $T_{\text{sat}} = 40^\circ\text{C}$): (a) Ethanol; (b) Water.	68
28	Maximum heat transport versus groove fill ratio for several working temperatures (Ethanol): (a) $ \vec{a}_r = 0.0\text{-g}$; (b) $ \vec{a}_r = 10.0\text{-g}$	69
29	Maximum heat transport versus radial acceleration: (a) $A_l/A_g = 0.5$; (b) $A_l/A_g = 1.0$	70
30	Grooves chemically etched in glass (Courtesy of D. Liepmann, University of California at Berkeley).	88
31	Flow of liquid in a sinusoidal groove: (a) Definition of geometric parameters; (b) Dimensionless solution domain.	89
32	Dimensionless velocity fields for laminar flow in a sinusoidal groove ($\beta = 0.5$, $w_l^*/2 = 0.25$, $\phi = 25^\circ$): (a) $\tau_{lv}^* = 2.0$ (cocurrent flow); (b) $\tau_{lv}^* = 0.0$; (c) $\tau_{lv}^* = -0.1$ (countercurrent flow).	90
33	Variation of the flow variables with shear stress at the liquid-vapor interface for various values of meniscus contact angle ($\beta = 0.5$, $w_l^*/2 = 0.25$, $P^* = 1.15245$): (a) Mean velocity; (b) Volumetric flow rate; (c) Poiseuille number.	91
34	Variation of the flow variables with groove fill ratio for various values of groove aspect ratio ($\tau_{lv}^* = 0.0$, $\phi = 0^\circ$): (a) Mean velocity; (b) Volumetric flow rate; (c) Poiseuille number.	92
35	Semi-analytical solution for \bar{v}^* : (a) Definition of parameters; (b) Force balance on the liquid in a sinusoidal groove.	93

36	Comparison of the semi-analytical solution with numerical data ($\beta = 0.5$, $w_l^*/2 = 0.25$): (a) Countercurrent vapor shear stress required for $\bar{v}^* = 0$; (b) Normalized mean velocity versus normalized shear stress at the liquid-vapor interface.	94
37	Definition of geometric parameters.	95
38	Determination of the cross-sectional area of the liquid.	96
39	Variations of the basic μ CPL design.	111
40	Schematic of μ -CPL test setup.	112
41	Mounting fixture for the μ CPL.	113
42	Photograph of the copper calorimeter.	114
43	Photograph showing thermocouples adhered to the back of the μ CPL wafer with vacuum epoxy. The stainless steel fill tube is on the left-hand side. . . .	115
44	CO ₂ laser calibration: (a) Typical calorimeter temperature increase trace (LCS = 10%); (b) Typical laser power measurement traces (LCS = 10%); (c) Heat rates versus LCS (Data points in square brackets were taken when the borosilicate glass melted on the wafer).	116
45	Temperature responses of a typical thermocouple, the resistance temperature detector, and the recirculating chiller bath.	117
46	Temperature reading obtained during calibration (Thermocouple 201): (a) Temperature obtained by RTD vs. temperature reading from TC201; (b) Error obtained when substituting raw data into the linear best-fit equation for TC201.	118
47	Schematic of the heat pipe filling station: (a) Current system; (b) System incorporating a standard filling station.	128
48	Thermodynamic heat pipe filling station.	129
49	Critical orifice plate: (a) Internal design; (b) Installation in the filling station. . . .	130
50	Mass of liquid in the heat pipe at State 2 versus initial liquid charge ($m_{a, hp} = 0$, $P_{vc,1} = 30$ mTorr, $T_1 = 25^\circ\text{C}$, $P_{atm} = 10^5$ Pa).	131
51	Close-up view of the heat pipe assembly mounted to the centrifuge table. . . .	140
52	Placement of the heat pipe assembly on the centrifuge table ($R = 44.5$ inches). . . .	141

53	Typical start-up test results for $a_r = 5.0$ -g: (a) 3IHP (RAY33); (b) 6IHP (RAY22); (c) 9IHP (RAY9).	142
54	Temperature differences between the evaporator and adiabatic sections for the start-up tests.	143
55	Typical burst test results for $a_r = 5.0$ -g: (a) 3IHP (RAY28); (b) 6IHP (RAY16); (c) 6IHP (RAY17); (d) 9IHP (RAY2).	144
56	Temperature differences between the evaporator and adiabatic sections for the burst tests.	145
57	Start-up response characteristics.	146

List of Tables

1	The geometric variable values associated with the working fluid inventory. . .	7
2	The calculated total mass of the working fluid inventory.	8
3	Helically-grooved heat pipe specifications.	10
4	Maximum uncertainties of measured and calculated values.	13
5	Specifications of the heat pipe test article examined by Castle et al. [1]. . .	55
6	Poiseuille number versus sinusoidal duct aspect ratio: Comparison of the present solution with that given by Shah (1975).	74
7	Mean velocity, Poiseuille number and volumetric flow rate versus shear stress at the liquid-vapor interface for various values of meniscus contact angle ($\beta = 0.5$, $w_l^*/2 = 0.25$, $P^* = 1.15245$).	76
8	Wetted perimeter, mean velocity, Poiseuille number and volumetric flow rate versus groove fill ratio for various values of groove aspect ratio ($\tau_{lv}^* = 0.0$, $\phi = 0^\circ$).	77
9	Laser calibration data.	107
10	Laser calibration data, continued.	108
11	Laser calibration data, continued.	109
12	Thermocouple calibration equations: $T_{\text{actual}} = mT_{\text{reading}} + b$ (Valid ranges: TCs 201–210, $10^\circ\text{C} \leq T_{\text{reading}} \leq 95^\circ\text{C}$; TCs 211 and 212, $10^\circ\text{C} \leq T_{\text{reading}} \leq 40^\circ\text{C}$).	110

13	Heat pipe filling station volume data ($V_{vc} = 514.3 \text{ in}^3 = 8.428 \times 10^{-3} \text{ m}^3$, $V_m = 1.591 \text{ in}^3 = 2.607 \times 10^{-5} \text{ m}^3$, $V_{hp} = 0.047 \text{ in}^3 = 7.702 \times 10^{-7} \text{ m}^3$, $V_t = 8.455 \times 10^{-3} \text{ m}^3$).	133
14	Temperature differences between the evaporator and adiabatic sections for the start-up tests (Fig. 54).	147
15	Temperature differences between the evaporator and adiabatic sections for the burst tests (Fig. 56).	148
16	Start-up response characteristics (Fig. 57).	149

Abstract

This final report describes the progress to date on six individual projects.

1. "The Effect of Working Fluid Inventory on the Performance of Revolving Helically-Grooved Heat Pipes" is related to an experimental analysis of working fluid inventory and its effects on the capillary limit of grooved heat pipes.
2. "Fully-Developed Laminar Flow in Trapezoidal Grooves with Shear Stress at the Liquid-Vapor Interface" concerns the effects of geometry and interfacial shear stress on the pressure drop in trapezoidal grooves.
3. "Fully-Developed Laminar Flow in Sinusoidal Grooves" is similar to the above, except that the sinusoidal grooves typically seen in micro-etching are examined.
4. "Micro Capillary Pumped Loop Testing" deals with the design, manufacture and calibration of an experimental facility for testing capillary pumped loops embedded in silicon wafers. A description of the current experimental setup and the details of the calibration of the laser controller and the calibration of the thermocouples are provided. The second project is entitled,
5. "Design and Testing of a Thermodynamic Filling Station for Miniature Heat Pipes," which concerns a novel filling procedure for miniature heat pipes. The experimental setup and procedure is described, which involves a vacuum chamber within an environmental chamber. A thermodynamic analysis of the process is provided, and the results are compared to the experimental data. The final project of this report is entitled,
6. "Acceleration Testing of Three Raytheon Heat Pipes using the AFRL/PRPS Centrifuge Table". The objective of this project was to determine the performance of heat pipes under various acceleration conditions, which were imposed by the centrifuge table located in Bldg. 71-B H-Bay in Area B of Wright-Patterson AFB. Information on the experimental setup, experimental procedure, and an analysis of the results are provided.

1 The Effect of Working Fluid Inventory on the Performance of Revolving Helically-Grooved Heat Pipes

1.1 Abstract

The results of a recently completed experimental and analytical study showed that the capillary limit of a helically-grooved heat pipe (HGHP) was increased significantly when the transverse body force field was increased. This was due to the geometry of the helical groove wick structure. The objective of the present research was to experimentally determine the performance of revolving helically-grooved heat pipes when the working fluid inventory was varied. This report describes the measurement of the geometry of the heat pipe wick structure and the construction and testing of a heat pipe filling station. In addition, an extensive analysis of the uncertainty involved in the filling procedure and working fluid inventory has been outlined. Experimental measurements include the maximum heat transport, thermal resistance and evaporative heat transfer coefficient of the revolving helically-grooved heat pipe for radial accelerations of $|\vec{a}_r| = 0.0, 2.0, 4.0, 6.0, 8.0,$ and 10.0-g and working fluid fills of $G = 0.5, 1.0$ and 1.5 . An existing capillary limit model was updated and comparisons were made to the present experimental data.

1.2 Introduction

Helically-grooved heat pipes (HGHPs) have potential applications in the thermal management of rotating equipment such as aircraft alternators, large-scale industrial electric motors, and spinning satellites. In two recent studies (Klasing et al., 1999; Thomas et al., 1998), the performance of revolving HGHPs was investigated. It was found that the capillary limit increased with the strength of the acceleration field perpendicular to the heat pipe axis. In order to move HGHPs closer to application, knowledge must be gained concerning the sensitivity of the capillary limit to working fluid fill amount, since variations in the fill amount are inevitable during the manufacture of these devices. Very few studies were available concerning the effect of working fluid fill on the performance of axially-grooved heat pipes, but those found have been outlined below. In addition, synopses of the two aforementioned studies on revolving HGHPs have also been provided.

Brennan et al. (1977) developed a mathematical model to determine the performance of an axially-grooved heat pipe which accounts for liquid recession, liquid-vapor shear interaction and puddle flow in a 1-g acceleration environment. The model considered three distinct flow zones: the grooves unaffected by the puddle, the grooves that emerge from the puddle, and the grooves that are submerged by the puddle. The model for the puddle consisted of satisfying the equation of motion for the puddle and the continuity equation at the puddle-groove interface, and was solved by a fourth-order Runge-Kutta integration method with self-adjusting step sizes. The assumptions made by the model for the puddle were uniform heat addition and removal with a single evaporator and a single condenser section, and one-dimensional laminar flow in the puddle. The transport capability of the grooves unaffected by the puddle and the grooves extending beyond the puddle were approximated by a closed-form solution with laminar liquid and vapor flow. The working fluids used for the experiment were methane, ethane and ammonia. Brennan et al. (1977) stated that the mathematical model agreed well with the experimental data for ideally filled and overfilled heat pipes, but some differences were noted for underfilled heat pipes. In general, it was found for ideally filled heat pipes the predicted transported heat was higher than that measured. Also, this discrepancy was more significant for lower operating temperatures. In addition, it was found during the experiments that the maximum transported heat increased with fill volume.

Vasiliev et al. (1981) performed a series of experiments on an aluminum axially-grooved heat pipe which was overfilled and ideally filled. The width and height of the grooves were $w = 0.123$ mm and $h = 0.7$ mm, respectively, with an overall heat pipe length of $L_t = 80.0$ cm. The working fluids were acetone and ammonia. Vasiliev et al. showed that the temperature difference from the evaporator to the adiabatic regions increased at a much slower rate with increasing overfills. This was attributed to a thin film of liquid emerging from the overfill pool wetting the upper grooves. Vasiliev et al. stated that this thin film was lifted over the grooves by capillary forces due to microroughness on the groove surface. A mathematical model was developed for low temperature axially-grooved heat pipes to estimate heat pipe performance for 0-g and 1-g applications. The mathematical model was a set of boundary-value problems applied to each groove and was solved by a numerical

iteration method. The model was based on pressure balance equations and mass continuity written for a single groove. The temperature of the vapor in the adiabatic region was an input parameter, and the vapor pressure gradient was assumed to be one-dimensional. In addition, the liquid-vapor shear stress was assumed to be constant, and the starting liquid film thickness was of the same order of magnitude as the groove microroughness. Very good agreement was reported between the mathematical model and experimental transported heat results for ideally filled and overfilled heat pipes under gravity.

Thomas et al. (1998) presented experimental data obtained from a helically-grooved copper heat pipe which was tested on a centrifuge table. The heat pipe was bent to match the radius of curvature of the table so that uniform transverse (perpendicular to the axis of the heat pipe) body forces field could be applied along the entire length of the pipe. The steady-state performance of the curved heat pipe was determined by varying the heat input ($Q_{in} = 25$ to 250 W) and centrifuge table velocity (radial acceleration $|\vec{a}_r| = 0.01$ to 10 -g). It was found that the capillary limit increased by a factor of five when the radial acceleration increased from $|\vec{a}_r| = 0.01$ to 6 -g due to the geometry of the helical grooves. A model was developed to calculate the capillary limit of each groove in terms of centrifuge table angular velocity, the geometry of the heat pipe and the grooves, and the temperature-dependent working fluid properties. The agreement between the model and the experimental data was satisfactory.

Klasing et al. (1999) developed a mathematical model to determine the operating limits of a revolving helically-grooved straight heat pipe. The capillary limit calculation required an analysis of the total body force imposed by rotation and gravity on the liquid along the length of the helical grooves. The boiling and entrainment limits were calculated using methods described by Faghri (1995). It was found that the capillary limit increased significantly with rotational speed due to the helical geometry of the heat pipe wick structure. The maximum heat transport was found to be a function of angular velocity and tilt angle from horizontal. In addition, a minimum value of angular velocity was required to obtain the benefits of the helical groove geometry.

The first objective of the present study was to determine the sensitivity of the performance of revolving HGHPs to the working fluid fill amount. This required a precise knowledge of

the geometry of the heat pipe and helical grooves. In addition, a precision filling station was constructed and calibrated to determine the uncertainties involved in the filling procedure. The copper-ethanol heat pipe was tested on a centrifuge table at Wright-Patterson AFB (AFRL/PRPG) to determine the capillary limit, thermal resistance and evaporative heat transfer coefficient for fill ratios of $G = 0.5, 1.0$ and 1.5 , and radial accelerations of $|\vec{a}_r| = 0.01, 2.0, 4.0, 6.0, 8.0$ and 10.0 -g. The second objective of the present study was to improve the existing analytical capillary limit model developed by Thomas et al. (1998) using the above-mentioned geometric measurements and by using improved equations for the working fluid properties.

1.3 Determination of Heat Pipe Working Fluid Inventory

The objective of this analysis was to determine the working fluid inventory of a HGHP, which consists of the mass of liquid in the grooves and the mass of vapor in the vapor space. Since the heat pipe is a closed container under saturation conditions, the total mass of working fluid in the heat pipe is given by

$$m_t = m_v + m_l = \frac{V_{vs}}{v_v} + \frac{GV_{gr}}{v_l} \quad (1)$$

where $G = V_l/V_{gr}$ is the ratio of the volume of liquid to total groove volume. The volume of the vapor space is

$$V_{vs} = \frac{\pi}{4} D_{vs}^2 L_t + V_{gr}(1 - G) \quad (2)$$

The second term in eqn. (2) accounts for the increase or decrease in the vapor space volume when the parameter G is varied. The total volume of the grooves is

$$V_{gr} = L_{gr} N_{gr} A_{gr} \quad (3)$$

A cross-sectional view of a typical helical groove in the experimental test article is shown in Fig. 1. The cross-sectional area of the trapezoidal groove accounts for the differing side angles.

$$A_{gr} = wh + \frac{1}{2} h^2 (\tan \theta_1 + \tan \theta_2) \quad (4)$$

The total length of each groove is

$$L_{gr} = L_t \left[\left(\frac{2\pi r_h}{p} \right)^2 + 1 \right]^{\frac{1}{2}} \quad (5)$$

The radius of the helix is given by

$$r_h = \frac{1}{2} (D_{vs} + h) \quad (6)$$

The helical pitch is the distance through which the helix makes one revolution around its radius.

$$p = \frac{2\pi(s - s_1)}{(\phi - \phi_1)} \quad (7)$$

The helix angle ϕ corresponds to s , which is the distance traveled along the centerline of the heat pipe.

In order to calculate the working fluid inventory for the HGHP, measurements of the appropriate geometric parameters were made. In addition, an extensive uncertainty analysis was performed to determine the uncertainties of both the measured and calculated variables used in finding the working fluid inventory.

The physical variables given in eqn. (4) for the cross-sectional area of the grooves have been measured. A sample of the HGHP container was set in an epoxy resin mold, polished, and examined under a microscope with 50 \times magnification. Computer software was used to make bitmap pictures of ten different grooves and a microscopic calibration scale. These pictures were then analyzed to determine the geometric values shown in Fig. 1. Since the corners at the top of the land between grooves were not well defined, a special procedure was established to determine the geometry of the grooves. First, lines were drawn along the bottom and sides of each groove. Then, a line was drawn across the bottom of the land between grooves, as shown in Fig. 1. This line was then transposed to the top of the land. The intersections between this line and the lines along the sides of the groove were defined as the upper corners of the groove. Note that the two lines along the land tops are at different angles due to the radius of curvature of the heat pipe container. The angles θ_1 and θ_2 , and the height and width of the groove h and w were found using a bitmap picture of the microscopic calibration scale as described by Castle (1999).

An optical comparator was used to determine the vapor space diameter of the heat pipe container sample. The cross hairs of the optical comparator were carefully aligned with the top of the land between grooves on the left edge of the pipe. The comparator table was then moved until the land tops on the right edge of the pipe were aligned with the cross hairs.

The diameter of the heat pipe vapor space was the distance of the table movement.

The helical groove pitch was found using a vertical milling machine and an angular displacement transducer. The heat pipe container material was originally 1 m long. Approximately one-half was used to form the heat pipe, and the other half was used to determine the pitch. The rotation angle ($\phi - \phi_1$) and the corresponding distance along the centerline of the heat pipe ($s - s_1$) has been found as shown in Fig. 2(a). A heat pipe holding device was constructed from two angle aluminum uprights mounted to the table of a vertical milling machine. Precision alignment blocks were attached to the undersides of the uprights to engage one of the grooves in the milling machine table for improved alignment. Nylon bushings were placed in the uprights to center both the heat pipe container and the shaft, which was concentric with the heat pipe container. A small pin was made from a 1.58 mm (0.0625 in) dowel pin, where one end was ground to 0.26 mm to fit in the base of the helical groove. This sprung pin was set in a hole in the shaft where it engaged one of the grooves, as shown in Fig. 2(b). An angular displacement transducer was mounted onto another piece of angle aluminum. A vertical 6.35 mm (0.25 in) dowel pin was placed in the angle aluminum to align with the angular displacement transducer shaft. The dowel pin was held by a collet installed in the milling machine spindle in order to fix the location of the displacement transducer. The shaft of the transducer was linked to the shaft within the heat pipe by three set screws. As the milling machine table moved the pipe over the stationary shaft, the pin followed the helical groove, causing the shaft to rotate. The angular displacement transducer measured this rotation. A multimeter was used to measure the output voltage of the angular displacement transducer. The distance of the table movement was ($s - s_1$), which was read from the milling machine display unit. The transducer output voltage was measured over 10 cm lengths for ten different groups. Backlash errors were avoided by not reversing the table movement while taking data. The pitch was calculated using eqn. (7) at a point in the center of each 10 cm length. An average of 88 values were used to calculate the helical pitch.

Using the analysis given by Miller (1989), the root-sum-square uncertainties for the groove cross-sectional area, helical pitch, helix radius, groove length, groove volume, vapor space volume, and total mass of the working fluid inventory have been calculated. The

Table 1: The geometric variable values associated with the working fluid inventory.

Measured Values	
h	0.03831 ± 0.00076 cm
w	0.03445 ± 0.0010 cm
θ_1	$15.44^\circ \pm 0.91^\circ$
θ_2	$13.80^\circ \pm 0.96^\circ$
D_{vs}	1.359 ± 0.005 cm
L_t	43.8 ± 0.084 cm
Calculated Values	
A_{gr}	$1.703 \times 10^{-3} \pm 6.0 \times 10^{-5}$ cm ²
p	135.8 ± 5.9 cm
r_h	0.6992 ± 0.0025 cm
L_{gr}	43.82 ± 0.84 cm
V_{gr}	3.73 ± 0.13 cm ³

measured and calculated uncertainties for all geometric variables presented are shown in Table 1.

A literature survey was completed to determine the specific volumes of ethanol vapor and liquid at various saturation temperatures, as shown in Fig. 3. This information was needed to determine the total mass and uncertainty of the working fluid inventory $m_t \pm \Delta m_t$. While existing texts report these properties (Faghri, 1995; Peterson, 1994, Lide and Kehiaian, 1994; Carey, 1992; Schlunder, 1983; Ivanovskii et al., 1982), it was found that most simply referred to previous sources. Therefore, the data shown in Fig. 3 represent information gathered from primary sources that cannot readily be traced further. In Fig. 3(a), the available data for the specific volume of liquid in the range of $T_{sat} = 0$ to 100°C are relatively scattered. Vargaftik (1975) stated that the ethanol used was 96% pure by volume, with water making up most of the other 4%. Ethanol is aggressively hygroscopic, so special procedures are required for further purification as outlined by Timmermans (1950) concerning anhydrous ethanol. Since the data by Timmermans (1950) and TRC (1983) are nearly coincident, it is believed that the data reported by TRC (1983) are also for anhydrous ethanol. Dunn and Reay (1978) do not provide information concerning purity. Therefore, the Vargaftik (1975) data and the Dunn and Reay (1978) data have been discarded in Fig. 3(a). In Fig. 3(b), the deviation of the Dunn and Reay (1978) data for the specific volume of vapor is significant. Therefore,

Table 2: The calculated total mass of the working fluid inventory.

G	m_t (g)	Δm_t (g) Calculated	Δm_d (g) Filling Station
0.5	1.47	$\pm 3.6\%$	$\pm 5.0\%$
1.0	2.92	$\pm 3.7\%$	$\pm 2.9\%$
1.5	4.38	$\pm 3.6\%$	$\pm 1.9\%$

the Dunn and Reay (1978) data has been discarded in Fig. 3(b). Polynomial curve fits from $0 \leq T_{\text{sat}} \leq 100^\circ\text{C}$ have been obtained for the data shown in Figs. 3(a) and 3(b) for the specific volumes of liquid and vapor ethanol. These curve fits have been evaluated at room temperature to determine the proper values to be used in the uncertainty analysis, since the heat pipe was filled at room temperature. Information concerning the uncertainty of the original data was not available. Therefore, the uncertainties of these properties have been estimated to be the maximum variance of the data from the curve fits ($\Delta v_l = 3.5 \times 10^{-8} \text{ m}^3/\text{kg}$, $\Delta v_v = 0.39 \text{ m}^3/\text{kg}$). The specific volumes of liquid and vapor ethanol (m^3/kg) as functions of saturation temperature ($^\circ\text{C}$) are shown below for the range $0 \leq T_{\text{sat}} \leq 100^\circ\text{C}$

$$v_l = \exp(a_0 + a_1 T_{\text{sat}} + a_2 T_{\text{sat}}^2 + a_3 T_{\text{sat}}^3 + a_4 T_{\text{sat}}^4)/1000 \quad (8)$$

$$v_v = \exp(b_0 + b_1 T_{\text{sat}} + b_2 T_{\text{sat}}^2 + b_3 T_{\text{sat}}^3 + b_4 T_{\text{sat}}^4)/1000 \quad (9)$$

where the coefficients are

$$\begin{aligned} a_0 &= 0.2153 & b_0 &= 10.35 \\ a_1 &= 1.049 \times 10^{-3} & b_1 &= -6.375 \times 10^{-2} \\ a_2 &= -1.345 \times 10^{-8} & b_2 &= 1.735 \times 10^{-4} \\ a_3 &= 2.025 \times 10^{-8} & b_3 &= 5.714 \times 10^{-7} \\ a_4 &= -5.474 \times 10^{-11} & b_4 &= -6.003 \times 10^{-9} \end{aligned}$$

The total mass of the working fluid inventory m_t and the associated uncertainty Δm_t for the range of fill values are given in Table 2.

1.4 Heat Pipe Filling Station

A filling station has been constructed which is capable of placing a low-temperature working fluid (i.e., water, ethanol, methanol) into a heat pipe without also introducing ambient air (Fig. 4). The station consisted of a manifold of valves and interconnecting stainless steel tubing, a working fluid reservoir, a dispensing burette, a vacuum pump, and a container of compressed dry nitrogen gas. Previous experience with filling stations showed that long runs of horizontal tubing could cause significant filling errors due to vapor bubbles within the tubing. To address this problem, the manifold was constructed such that the interconnecting tubing runs were very short (on the order of 2 cm). In addition, the tubes which intersect the main vertical tube between valves 2 and 5 (Fig. 4) were offset from each other and ran at a diagonal from the main tube. Again, the purpose of this design was to reduce the possibility of vapor bubbles adhering to the tubing walls, thus causing errors in the fill amount. However, it is likely that some vapor still does adhere to the tubing, so certain procedures were carried out during filling to eject as much vapor as possible. For instance, the 1 psig relief valve over valve 1 was cycled on and off several times. In addition, valves 2 and 5 were cycled on and off while noting the meniscus displacement within the dispensing burette. If the meniscus was displaced more than 0.06 cm^3 , vapor was probably trapped within the valve. The valve in question was then cycled until the bubble was ejected.

To fill the heat pipe, the container was first evacuated to a pressure of 10^{-6} Torr using a turbomolecular vacuum pump. The sealed pipe was then connected to the filling station at valve 5. The working fluid was frozen and thawed repeatedly to reduce the amount of dissolved air within the fluid. The entire filling station was then evacuated by a roughing pump, except the working fluid reservoir. After evacuation, the liquid working fluid was drawn up into the dispensing burette and into all interconnecting tubing. After noting the height of the meniscus, the desired amount of working fluid was metered into the heat pipe by carefully opening the heat pipe fill valve 8. The difference in height of the liquid column was related to the dispensed mass of working fluid.

During initial testing of the filling station, it was found that the mass of working fluid dispensed into the heat pipe container was different than what was indicated by the dis-

Table 3: Helically-grooved heat pipe specifications.

Working fluid	Ethanol
Working fluid charge	$m_t = 1.47, 2.92$ and 4.38 g
Evaporator length	$L_e = 15.2 \pm 0.16$ cm
Adiabatic length	$L_a = 8.2 \pm 0.16$ cm
Condenser length	$L_c = 15.2 \pm 0.16$ cm
Tube outside diameter	$D_o = 1.588 \pm 0.005$ cm
Tube wall thickness	$t_w = 0.0757$ cm
Radius of curvature	$R = 1.22$ m
Wall/wick materials	Copper
Wick structure	Helical grooves
Number of Grooves	$N_{gr} = 50$
Heater element	Nichrome heater tape
Fill valve	Nupro B-4HW bellows valve
Calorimeter	1/8 in. OD coiled copper tubing

pensing burette. Therefore, a rigorous calibration of the filling station was undertaken to determine a correlation between the change in volume read by the dispensing burette and the change in mass of a receiving burette attached at valve 5, which was measured using a precision scale. The total uncertainty of the working fluid inventory dispensed by the heat pipe filling station Δm_d is given in Table 2.

1.5 Experimental Setup

The purpose of the experiment was to examine the steady-state performance of a helically-grooved copper-ethanol heat pipe under various heat inputs and transverse body force fields using a centrifuge table located at Wright-Patterson AFB (AFRL/PRPG). Specifically, the amount of working fluid was varied ($G = 0.5, 1.0$ and 1.5) to determine the effects of under/overfilling on the capillary limit, thermal resistance and evaporative heat transfer coefficient of the HGHP. To ensure uniform radial acceleration fields over the length of the heat pipe, the pipe was bent to match the radius of curvature of the centrifuge table ($R = 1.22$ m). Physical information concerning the heat pipe is given in Table 3. It should be noted that the total helix angle was very small: Each groove rotated through an angle of approximately 2.03 rad (116 arc degrees) over the length of the pipe. The heat pipe was mounted to a

platform overhanging the edge of the horizontal centrifuge table. This allowed the heat pipe to be positioned such that the radius of curvature was equivalent to the outermost radius of the centrifuge table. Insulative mounting blocks were used to ensure that the heat pipe matched the prescribed radius as closely as possible. The horizontal centrifuge table was driven by a 20-hp dc motor. The acceleration field near the heat pipe was measured by a triaxial accelerometer. The acceleration field at the centerline of the heat pipe radius was calculated from these readings using a coordinate transformation.

A pressure-sensitive nichrome heater tape with an aluminized backing was uniformly wound around the circumference of the evaporator section for heat input. Power was supplied to the heat pipe evaporator section by a power supply through power slip rings to the table. While the current reading could be made directly using a precision ammeter, the voltage across the electric heater had to be measured on the rotating table because of the voltage drop between the control room and the table. Therefore, the voltage at the heater was obtained through the instrumentation slip ring assembly and read by a precision multimeter.

The calorimeter consisted of a length of 1/8 in. OD copper tubing wound tightly around the condenser section. The size of the tubing was chosen to be small to minimize the effects of acceleration on the performance of the calorimeter. Thermal grease was used between the heat pipe and the calorimeter to decrease contact resistance. Type T thermocouples were inserted through brass T-branch connectors into the coolant inlet and exit streams, and a high-resolution digital flow meter was used to measure the mass flow rate of the coolant (50% by mass ethylene glycol/water mixture). The mass flow rate was controlled using a high-pressure booster pump, which aided the low-pressure pump in the recirculating chiller. The percentage of ethylene glycol was measured periodically during testing using a precision hydrometer to ensure that the mixture did not change. The temperature of the coolant was maintained at a constant setting by the recirculating chiller. Coolant was delivered to the centrifuge table via a double-pass hydraulic rotary coupling. The mass flow rate was constant for all experiments. Values of the specific heat of ethylene glycol/water mixtures were obtained from ASHRAE (1977), which were in terms of percent ethylene glycol by weight and temperature. The average temperature between the calorimeter inlet and outlet was used to evaluate the specific heat. The specific heat did not vary appreciably during

testing since it is a weak function of temperature.

Heat pipe temperatures were measured by Type T surface-mount thermocouples, which were held in place using Kapton tape. Mounting locations for the thermocouples are shown in Fig. 5. A short unheated length next to the evaporator end cap was instrumented with thermocouples specifically for accurate thermal resistance measurements. In addition, groups of four thermocouples were arranged around the circumference of the heat pipe at stations in the evaporator section for local heat transfer coefficient information. Temperature signals were conditioned and amplified on the centrifuge table. These signals were transferred off the table through the instrumentation slip ring assembly, which was completely separate from the power slip ring assembly to reduce electronic noise. Conditioning the temperature signals prior to leaving the centrifuge table eliminated difficulties associated with creating additional junctions within the slip ring assembly. Temperature and acceleration signals were collected using a personal computer with data logging software. Since a shortage of thermocouple channels existed on the centrifuge table, a series of three electrical relays were engaged to read one set of thermocouples, and disengaged to read the other set.

Since the heat pipe assembly was subjected to air velocities due to the rotation of the table (up to $11 \text{ m/s} = 25 \text{ mi/hr}$), efforts were made to reduce convective heat losses from the exterior of the heat pipe. A thin-walled aluminum box was fabricated to fit around the heat pipe. Ceramic wool insulation was placed inside the box and around the heat pipe through three small doors on the top of the box. This insulation/box arrangement provided an effective barrier to convective losses from the heat pipe to the ambient.

The helically-grooved copper-ethanol heat pipe was tested in the following manner. The recirculating chiller was turned on and allowed to reach the setpoint temperature, which was measured at the calorimeter inlet. The centrifuge table was started from the remote control room at a slow constant rotational speed to prevent damage to the power and instrumentation slip rings. In this case, the radial acceleration was less than $|\vec{a}_r| < 0.01\text{-g}$. In all cases, the centrifuge table rotated in a clockwise direction as seen from above. Power to the heater was applied ($Q_{\text{in}} = 10 \text{ W}$) and the heat pipe was allowed to reach a steady-state condition. The power to the heater was then increased to $Q_{\text{in}} = 20 \text{ W}$ and again the heat pipe was allowed to reach a steady-state condition. This was repeated until the maximum allowable

Table 4: Maximum uncertainties of measured and calculated values.

Measured Values	
Coolant mass flow rate	$\Delta\dot{m}_c = \pm 0.05 \text{ g/s}$
Heater voltage	$\Delta V = \pm 0.5 \text{ V}$
Heater current	$\Delta I = \pm 0.1 \text{ A}$
Radial acceleration	$\Delta a_r = \pm 0.1\text{-g}$
Calorimeter inlet temperature	$\Delta T_{\text{in}} = \pm 0.07 \text{ K}$
Calorimeter outlet temperature	$\Delta T_{\text{out}} = \pm 0.08 \text{ K}$
Evaporator end cap temperature	$\Delta T_{\text{eec}} = \pm 0.09 \text{ K}$
Condenser end cap temperature	$\Delta T_{\text{cec}} = \pm 0.11 \text{ K}$
Calculated Values	
Heat input	See Fig. 6
Heat transported	$\Delta Q_t = \pm 3.2 \text{ W}$
Thermal resistance	See Fig. 7
Heat transfer coefficient	See Figs. 12 and 13

evaporator temperature was reached ($T_{w,\text{max}} = 100^\circ\text{C}$). After all data had been recorded the power to the heater was turned off, and the heat pipe was allowed to cool before shutting down the centrifuge table.

Using the analysis given by Miller (1989), the uncertainties for all of the measured and calculated values for the experimental data are presented in Table 4.

1.6 Results and Discussion

The objective of this experiment was to determine the steady-state performance of a revolving helically-grooved heat pipe as a function of the working fluid inventory. The heat input, radial acceleration and working fluid fill were varied as follows: $Q_{\text{in}} = 10$ to 180 W , $|\vec{a}_r| = 0.01$ to 10-g , and $G = 0.5, 1.0$ and 1.5 . Thermocouples on the inboard, outboard, top, and bottom sides of the heat pipe (Fig. 5) were used to determine the axial and circumferential temperature distributions. Typical steady-state temperature distributions for the heat pipe for $G = 1.0$ at $|\vec{a}_r| = 0.01\text{-g}$ are shown in Fig. 6. For low power input levels, the temperature distribution was uniform. As the power input increased, the temperatures within the evaporator and the short unheated section adjacent to the evaporator increased significantly, indicating a partial dryout situation. Since the coolant temperature and flow

rate were constant for all tests, the adiabatic and condenser temperatures increased slightly with input power. Figure 7 shows the thermal resistance versus transported heat over the entire range of radial acceleration for each fill level. In Fig. 7(a) the thermal resistance was quite high, which indicates that the heat pipe was partially dried out for $G = 0.5$, even at the lowest power input levels. However, the thermal resistance decreased significantly as the radial acceleration increased, showing that the capillary pumping ability of the helical grooves increased. For $G = 1.0$ and 1.5 , the thermal resistance decreased and then increased with transported heat when dryout commenced. The $G = 1.5$ fill tests showed dryout occurring only for $|\vec{a}_r| = 0.01$ and 2.0 -g. Dryout was not reached for $G = 1.5$ with $|\vec{a}_r| = 4.0, 6.0, 8.0$ and 10.0 -g due to reaching the maximum allowable heater temperature. The capillary limit was considered to be reached when the thermal resistance began to increase.

Thomas et al. (1998) presented a mathematical model which predicted the capillary limit of a helically-grooved heat pipe subjected to a transverse body force. This model accounted for the geometry of the heat pipe and the grooves (including helix pitch), body force field strength, and temperature-dependent working fluid properties. This model was updated to include the improved measurements of the wick geometry and working fluid properties. Castle (1999) provides a detailed comparison of the present model and that given by Thomas et al. (1998). The capillary limit versus radial acceleration is given in Fig. 8 for various working temperatures with the Thomas et al. (1998) model and the present model. The capillary limit increased steadily with radial acceleration and working temperature. The present model shows a significantly lower prediction for the capillary limit when compared to the Thomas model due to the improved geometric measurements and working fluid property equations.

Figure 9 shows a comparison of the experimental data and present analytical model for the capillary limit of a revolving helically-grooved heat pipe. In the legend of this figure, No Dryout and Partial Dryout refer to the experimental data. No attempt was made to maintain a constant adiabatic temperature during the experiments. Therefore, the working fluid temperature in the model was set to the adiabatic temperature found experimentally. For $G = 0.5$, the heat pipe operated successfully only for $|\vec{a}_r| \geq 8.0$ -g. In Fig. 9(b) ($G = 1.0$), the capillary limit increased significantly with radial acceleration. With the heat pipe

overfilled by 50% ($G = 1.5$), the capillary limit increased dramatically, showing the effect that overfilling has on performance. The agreement of the analytical model was very good for $G = 1.0$ as expected. For $G = 0.5$, the model overpredicted the experimental data because it was assumed that the grooves were completely filled. For $G = 1.5$, the model underpredicted the data due to the assumption that no liquid communication occurred between the grooves.

Temperatures within the evaporator section are shown in Figs. 10 and 11 for $|\vec{a}_r| = 0.01\text{-g}$ and 10.0-g , respectively. In general, the temperatures within the evaporator increased with transported heat. In addition, the wall temperatures decreased with G for a given heat transport due to the fact that more grooves were active. The temperatures along the length of the evaporator section can be tracked by examining the case for $G = 1.0$. Near the evaporator end cap, the temperatures departed those for $G = 1.5$ at approximately $Q_t = 15$ W (Fig. 10(a)). At $x = 92.1$ mm (Fig. 10(b)), this departure was delayed until approximately $Q_t = 25$ W, and at $x = 168$ mm (Fig. 10(d)), the data for $G = 1.0$ and 1.5 were nearly coincident. This behavior shows that the grooves were essentially full near the adiabatic section, and proceeded to dry out closer to the evaporator end cap, as expected. Dryout for the $G = 1.5$ case can be seen in Fig. 10(a) where the temperatures converged to nearly the same value around the circumference. It should be noted that the temperatures around the circumference were relatively uniform for $|\vec{a}_r| = 0.01\text{-g}$. Evaporator temperatures for $|\vec{a}_r| = 10.0\text{-g}$ are shown in Fig. 11. In comparison to $|\vec{a}_r| = 0.01\text{-g}$, the evaporator temperatures were in general lower due to the improved pumping ability of the helical grooves under increased radial acceleration. In addition, the temperatures tended to overlap over a greater range of heat transport values. In contrast to $|\vec{a}_r| = 0.01\text{-g}$, the evaporator temperature variation was greater around the circumference at higher Q_t , but no pattern was distinguishable in the data.

Local heat transfer coefficient data versus heat transport is shown in Figs. 12 and 13 for $|\vec{a}_r| = 0.01\text{-g}$ and 10.0-g . Overall, the values for h_e were very low for $G = 0.5$ due to the fact that most of the grooves were dried out. As the percent fill increased from $G = 0.5$ to $G = 1.0$, the heat transfer coefficient increased significantly. For $|\vec{a}_r| = 0.01\text{-g}$ (Fig. 12), h_e increased and then decreased with transported heat. This trend was also reported by Vasiliev et al. (1981) for an aluminum axially-grooved heat pipe with acetone as the working

fluid. For $G = 1.0$ and 1.5 , the heat transfer coefficient near the evaporator end cap (Fig. 12(a)) decreased until all of the values around the circumference converged. Closer to the adiabatic section, the heat transfer coefficient values around the circumference had not yet converged, showing these portions to still be active. For $|\vec{a}_r| = 10.0\text{-g}$ (Fig. 13), the values of h_e were significantly more uniform around the circumference and along the axial direction, even during a dryout event ($G = 1.0$, Fig. 13(a)). In addition, the heat transfer coefficient seems to be more constant with respect to the transported heat compared to $|\vec{a}_r| = 0.01\text{-g}$. During the experiments, the heat pipe working temperature was not constant, which resulted in changes in the specific volume of the liquid and vapor of the working fluid. Since the heat pipe was filled at room temperature, it was important to quantify the potential effects of the change in volume of liquid in the grooves with temperature. Figure 14 shows the variation of the percentage of groove volume occupied by liquid G with saturation temperature for the three fill amounts over the range of working temperatures seen in the experiments. The maximum percent difference was 2.7%, which was not deemed to be significant.

1.7 Conclusions

The effect of fluid inventory on the steady-state performance of a helically-grooved copper-ethanol heat pipe has been examined both experimentally and analytically. It was found that the capillary limit increased and the thermal resistance decreased significantly as the amount of working fluid within the heat pipe increased. In addition, the evaporative heat transfer coefficient was found to be a strong function of the fill amount. The updated analytical model was in very good agreement with the experimental capillary limit results for $G = 1.0$. However, the analytical model overpredicted the capillary limit data for $G = 0.5$ and underpredicted the data for $G = 1.5$.

1.8 Nomenclature

a	adiabatic length near the evaporator end cap, m
\vec{a}_r	radial acceleration, m/s^2
A_e	surface area in the evaporator section, $\pi r_v^2 L_e$, m^2
A_{gr}	cross-sectional area of a groove, m^2

b	adiabatic length near the condenser end cap, m
D_o	tube outside diameter, m
D_{vs}	diameter of the heat pipe vapor space, m
G	Ratio of liquid volume to total groove volume, V_l/V_{gr}
h	groove height, m
h_e	local heat transfer coefficient in the evaporator section, $Q_t/A_e(T_w - T_a)$, W/m ² -K
I	heater current, A
L_a	adiabatic length, m
L_c	condenser length, m
L_e	evaporator length, m
L_{gr}	helical groove length, m
L_t	total heat pipe length, m
m_d	mass of working fluid dispensed by the filling station, kg
m_l	mass of liquid, kg
m_t	total mass of working fluid inventory, kg
m_v	mass of vapor, kg
\dot{m}_c	coolant mass flow rate, kg/s
N_{gr}	number of grooves
p	helical pitch, m
Q_{cap}	capillary limit, W
Q_{in}	heat input at the evaporator, W
Q_t	heat transported, $\dot{m}_c C_p (T_{out} - T_{in})$, W
r_h	radius of the helix, m
r_v	radius of the heat pipe vapor space, m
R	radius of curvature, m
R_{th}	thermal resistance, $(T_{eec} - T_{cec})/Q_t$, K/W
s	coordinate along the centerline of the heat pipe, m
t_w	tube wall thickness, m
T_a	adiabatic temperature, K

T_{cec}	condenser end cap temperature, K
T_{eec}	evaporator end cap temperature, K
T_{in}	calorimeter inlet temperature, K
T_{out}	calorimeter outlet temperature, K
T_{sat}	saturation temperature, K
T_w	outer wall temperature, K
v_l, v_v	specific volume of liquid and vapor, m^3/kg
V	heater voltage
V_{gr}	volume of the grooves, m^3
V_{vs}	vapor space volume, m^3
w	width along the bottom of the groove, m
x	distance from the evaporator end cap, m
Δ	uncertainty
θ_1, θ_2	angles from the sides of the groove to vertical, rad
ϕ	helix angle, rad

Subscripts

cap	capillary
gr	groove
l	liquid
max	maximum
v	vapor
vs	vapor space

1.9 References

ASHRAE, 1977, *Handbook of Fundamentals*, American Society of Heating, Refrigerating and Air-Conditioning Engineers, Inc., Atlanta, GA.

Brennan, P., Krolczek, E., Jen H., and McIntosh R., 1977, "Axially Grooved Heat Pipes,"

AIAA 12th Thermophysics Conf., Paper No. 77-747.

Carey, V., 1992, *Liquid-Vapor Phase-Change Phenomena*, Hemisphere, Washington, D.C.

Castle, R., 1999, "The Effect of Working Fluid Inventory on the Performance of Revolving Helically-Grooved Heat Pipes," Masters Thesis, Wright State University, Dayton, Ohio.

Dunn, P., and Reay, D., 1978, *Heat Pipes*, Pergamon, Oxford.

Faghri, A., 1995, *Heat Pipe Science and Technology*, Taylor and Francis, Washington, D.C.

Ivanovskii, M., Sorokin, V., and Yagodkin, I., 1982, *The Physical Principles of Heat Pipes*, Clarendon, Oxford.

Klasing, K., Thomas, S., and Yerkes, K., 1999, "Prediction of the Operating Limits of Revolving Helically-Grooved Heat Pipes," *ASME Journal of Heat Transfer*, Vol. 121, pp. 213-217.

Lide, D., and Kehiaian, H., 1994, *CRC Handbook of Thermophysical and Thermochemical Data*, CRC Press, Boca Raton, FL.

Miller, R., 1989, *Flow Measurement Engineering Handbook*, 2nd Edn., McGraw-Hill.

Peterson, G., 1994, *An Introduction to Heat Pipes: Modeling, Testing, and Applications*, Wiley, New York.

Schlunder, E., 1983, *Heat Exchanger Design Handbook*, Hemisphere, Washington, D.C.

Thomas, S., Klasing, K., and Yerkes, K., 1998, "The Effects of Transverse Acceleration Induced Body Forces on the Capillary Limit of Helically-Grooved Heat Pipes," *ASME Journal of Heat Transfer*, Vol. 120, pp. 441-451.

Timmermans, J., 1950, *Physico-Chemical Constants of Pure Organic Compounds*, Elsevier, New York.

TRC, 1983, *TRC Thermodynamic Tables—Non-hydrocarbons*, Thermodynamic Research Center: The Texas A & M University System, College Station, TX (Loose-leaf data sheets).

Vargaftik, N., 1975, *Handbook of Physical Properties of Liquids and Gases*, Hemisphere, Washington, D.C.

Vasiliev, L., Grakovich L., and Khrustalev D., 1981, "Low-Temperature Axially Grooved Heat Pipes," *Proc. 4th Int. Heat Pipe Conf.*, London, pp. 337-348.

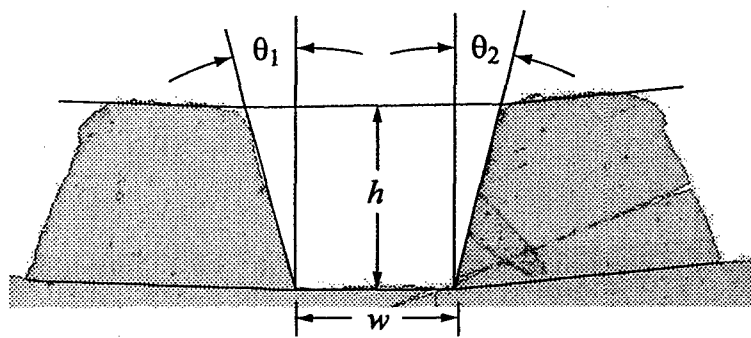


Figure 1: Photomicrograph of the helical groove geometry.

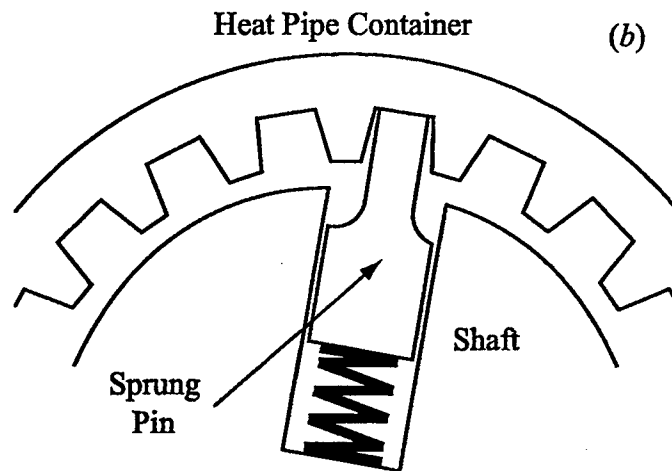
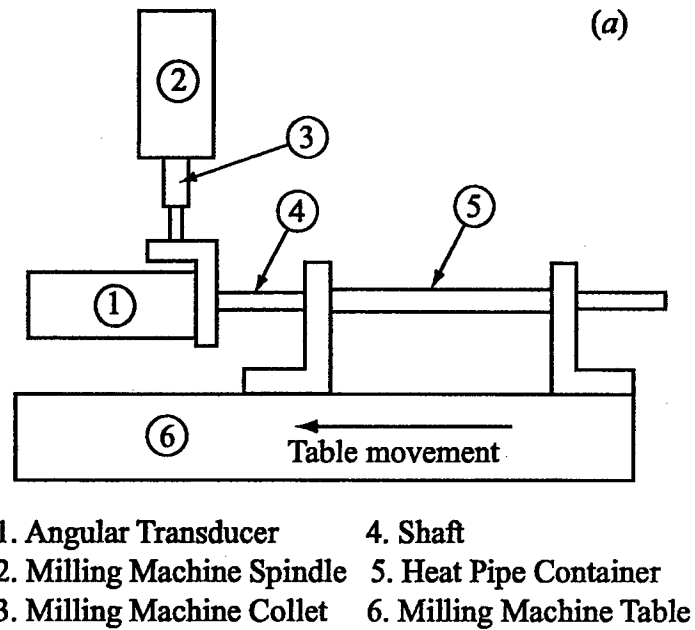


Figure 2: Schematic of the helical pitch measurement technique: (a) Major components; (b) Cross-sectional view of sprung pin engaging a helical groove.

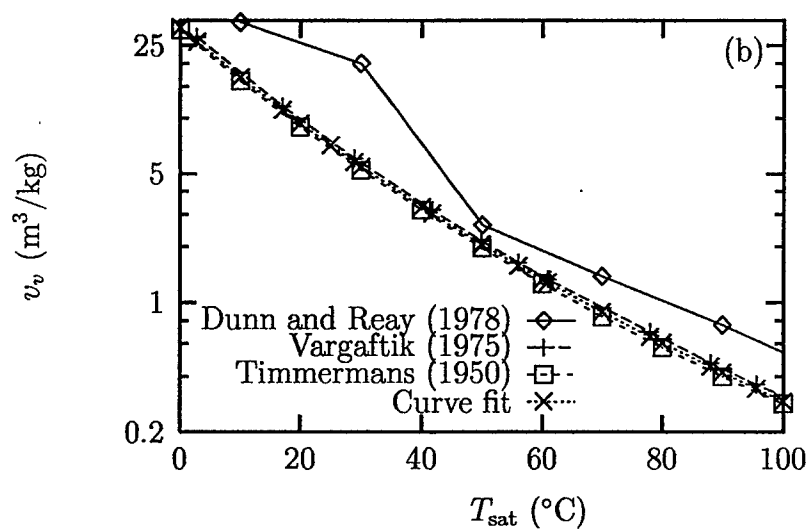
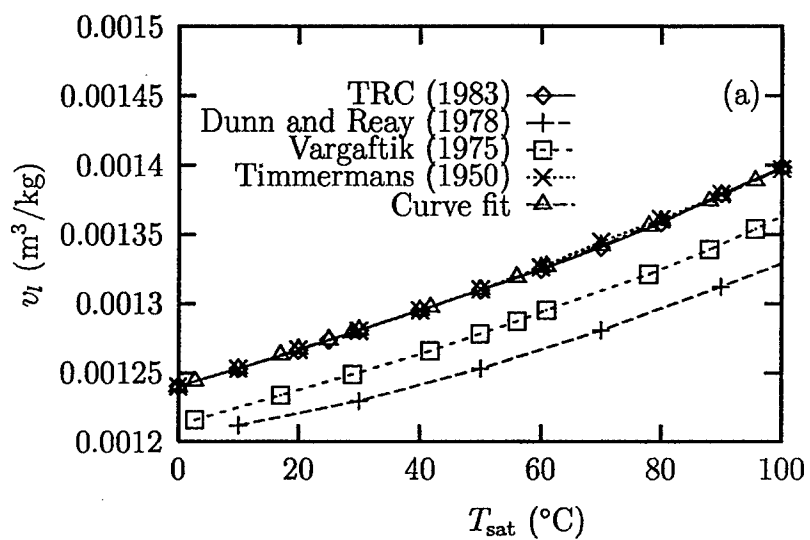


Figure 3: Specific volume of ethanol versus temperature: (a) Saturated liquid; (b) Saturated vapor.

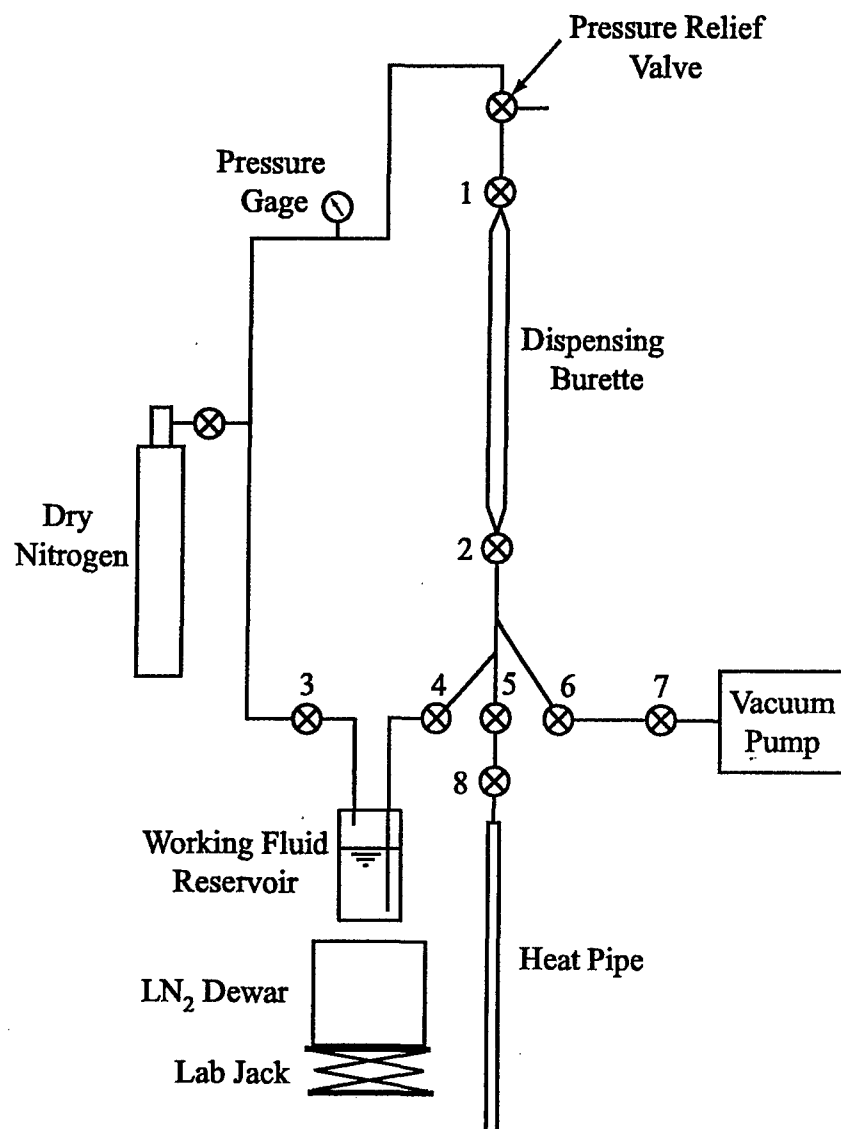
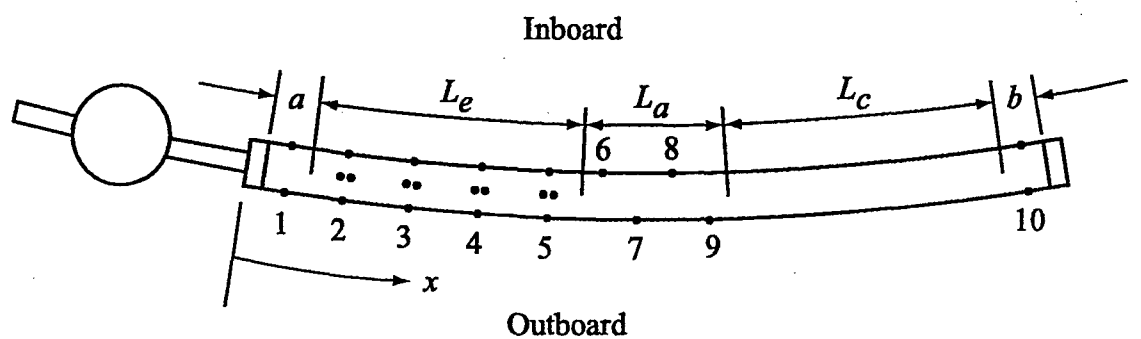


Figure 4: Schematic of the heat pipe filling station.



$a = 25.4 \text{ mm}$		TC#	$x \text{ (mm)}$	TC#	$x \text{ (mm)}$
$L_e = 152.4 \text{ mm}$		1IO	22.2	7O	218.
$L_a = 82.3 \text{ mm}$		2ITOB	54.0	8I	238.
$L_c = 152.4 \text{ mm}$		3ITOB	92.1	9O	259.
$b = 25.4 \text{ mm}$		4ITOB	130.	10IO	435.
End caps: 9.53 mm		5ITOB	168.	11	Coolant Inlet
		6I	198.	12	Coolant Outlet

Figure 5: Thermocouple locations and relevant lengths.

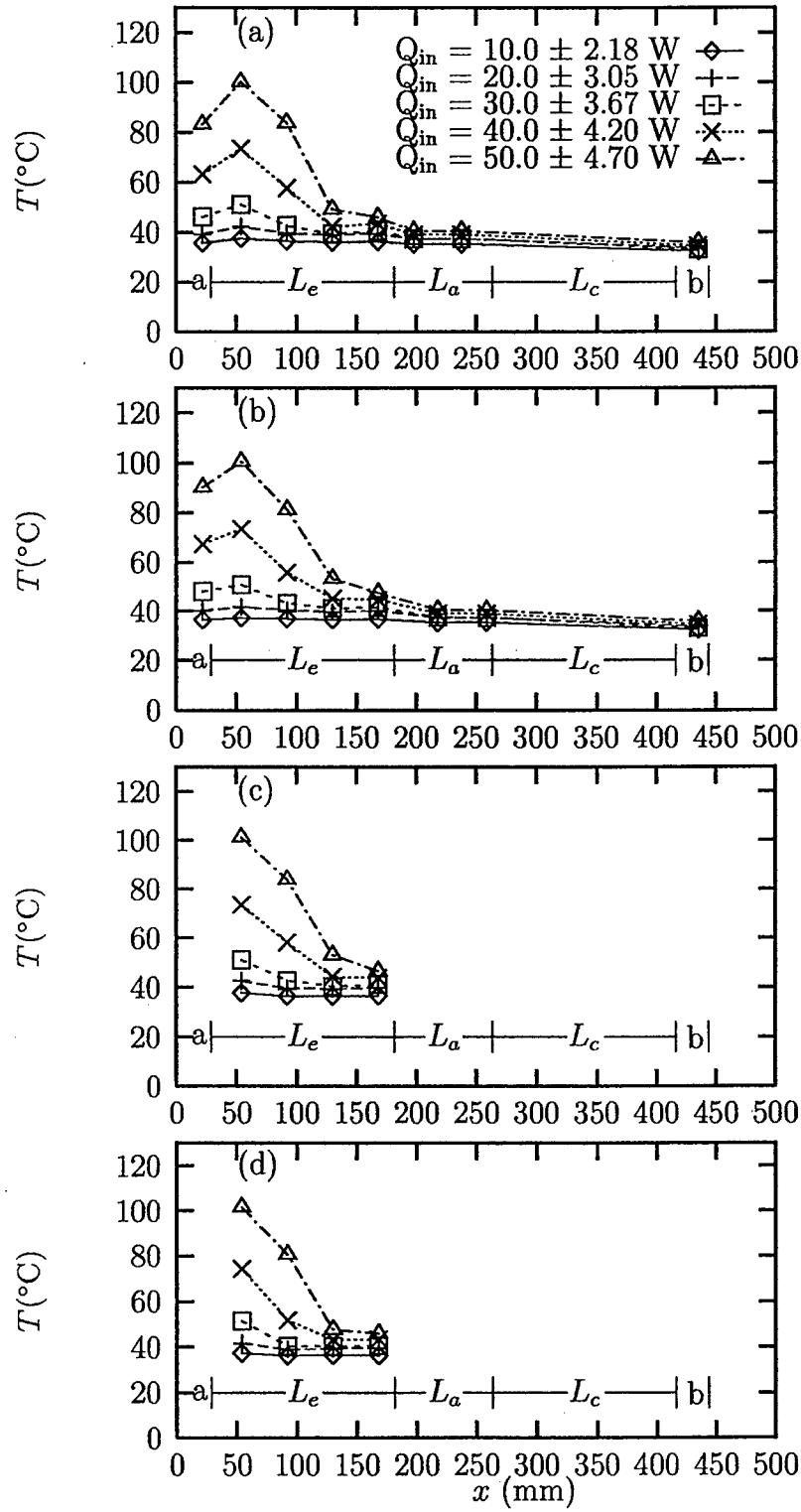


Figure 6: Steady-state temperature distributions for $|\vec{a}_r| = 0.01\text{-g}$, $G = 1.0$: (a) Inboard; (b) Outboard; (c) Top; (d) Bottom.

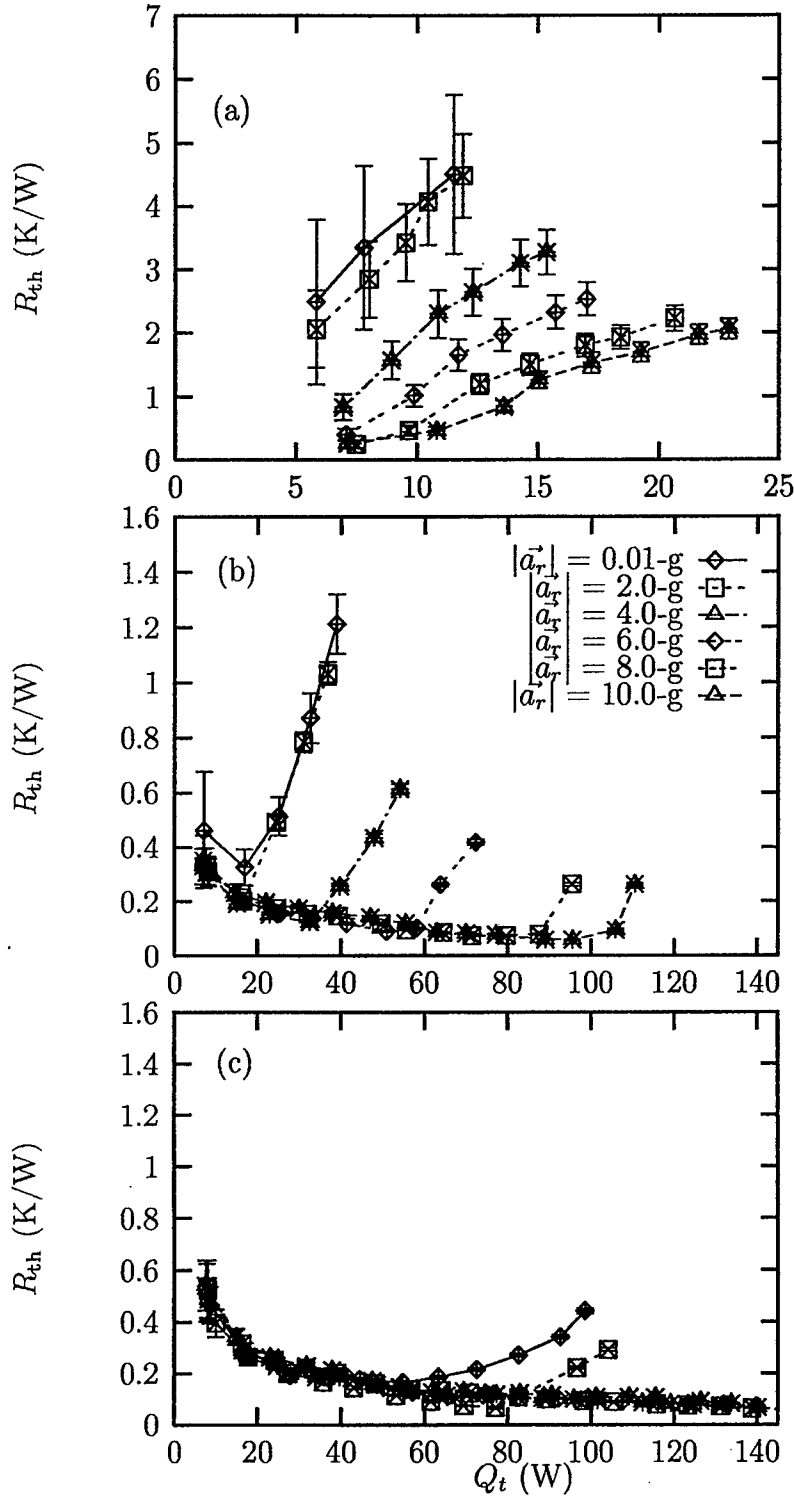


Figure 7: Thermal resistance versus heat transport: (a) $G = 0.5$; (b) $G = 1.0$; (c) $G = 1.5$.

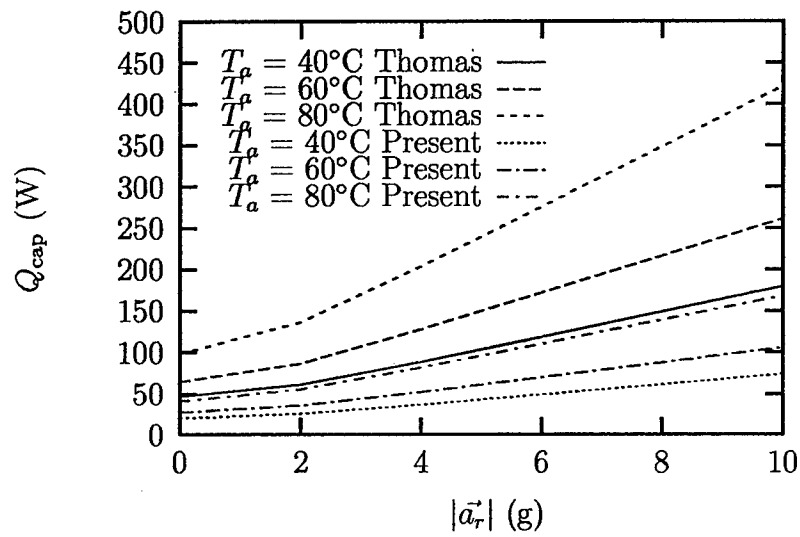


Figure 8: Capillary limit versus radial acceleration comparison of present model and Thomas et al. (1998).

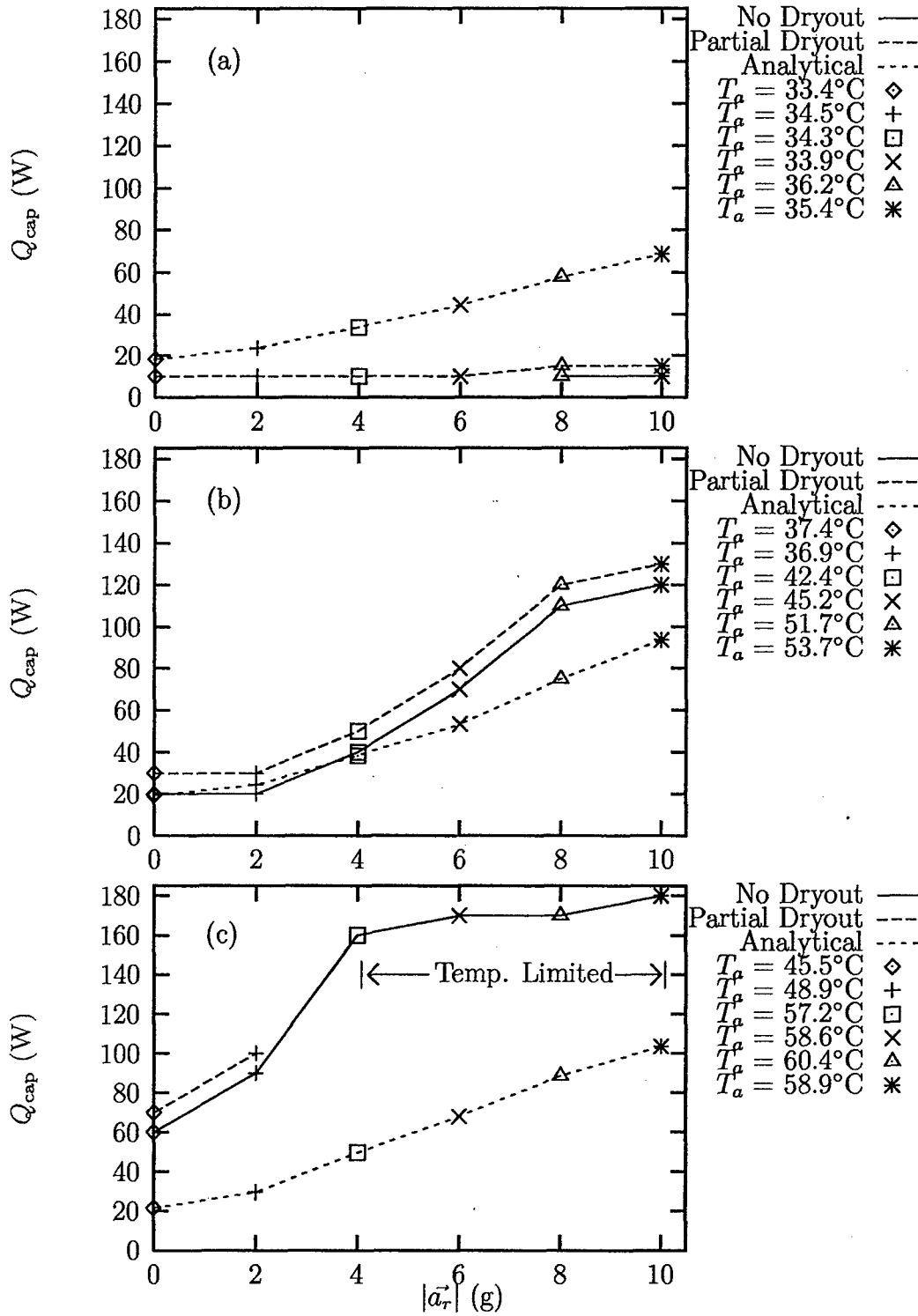


Figure 9: Comparison of present model and experimental capillary limit data versus radial acceleration: (a) $G = 0.5$; (b) $G = 1.0$; (c) $G = 1.5$.

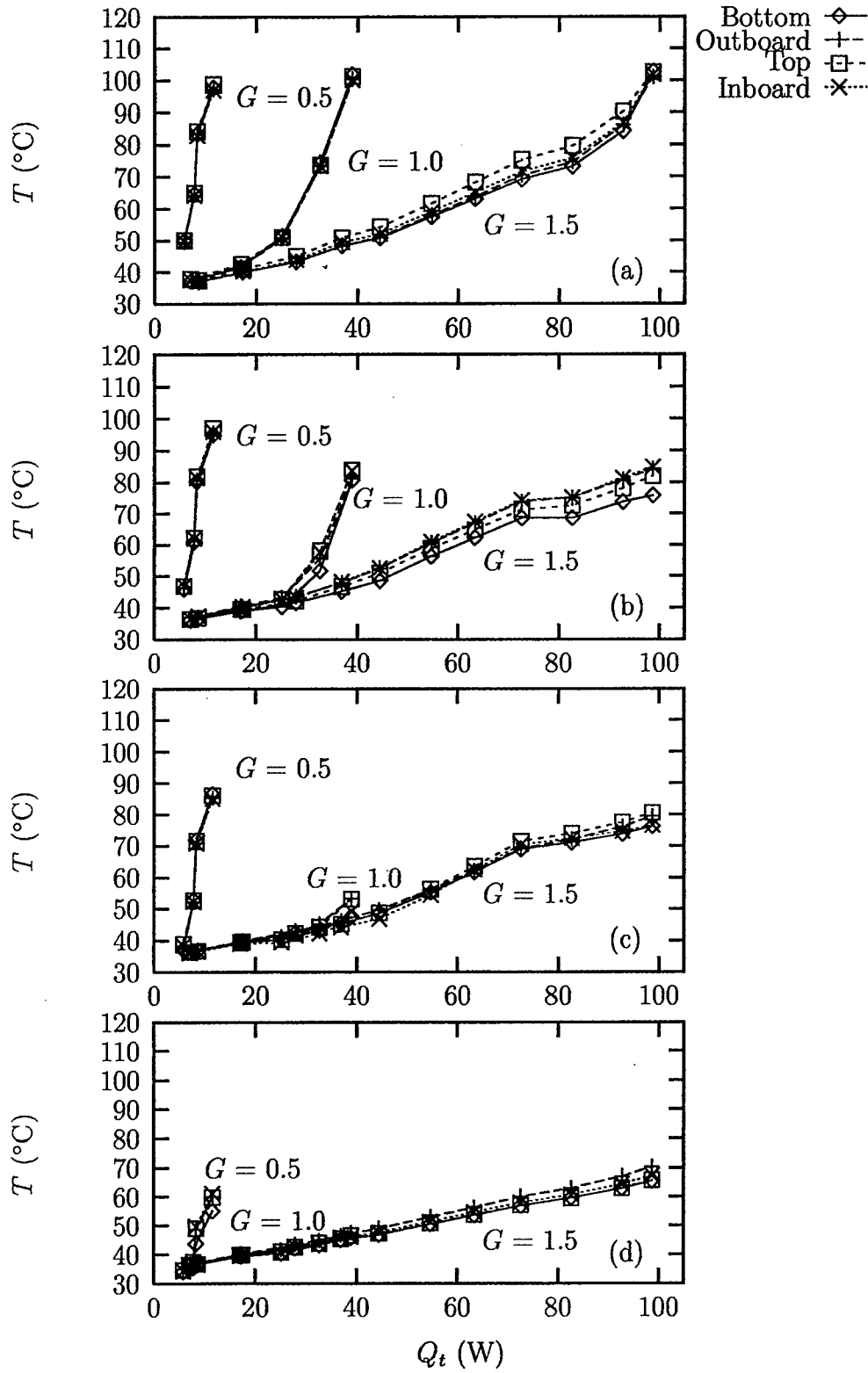


Figure 10: Temperatures within the evaporator section versus transported heat for $|\vec{a}_r| = 0.01\text{-g}$: (a) $x = 54.0$ mm; (b) $x = 92.1$ mm; (c) $x = 130$ mm; (d) $x = 168$ mm.

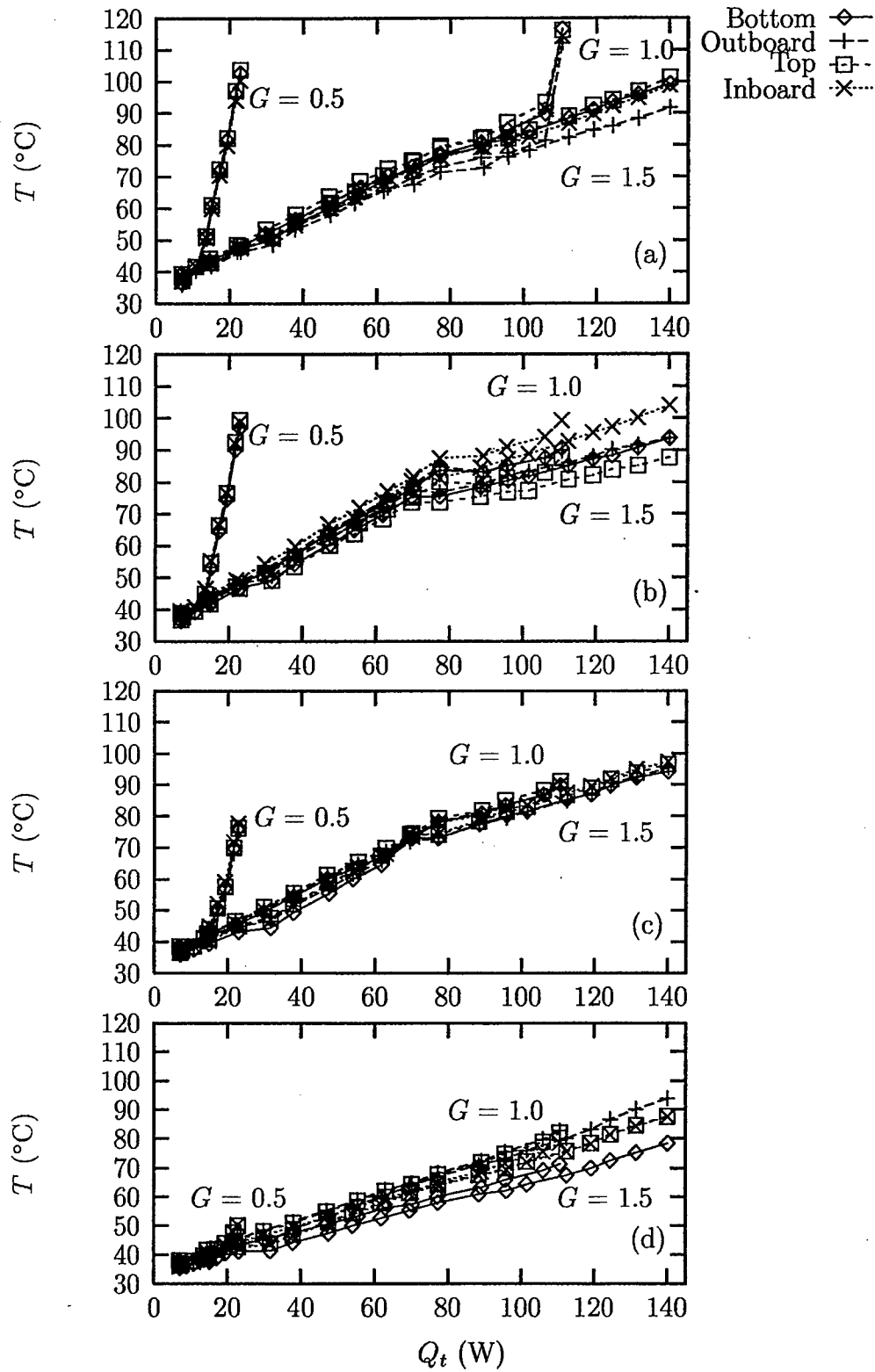


Figure 11: Temperatures within the evaporator section versus transported heat for $|\vec{a}_r| = 10.0$ -g: (a) $x = 54.0$ mm; (b) $x = 92.1$ mm; (c) $x = 130$ mm; (d) $x = 168$ mm.

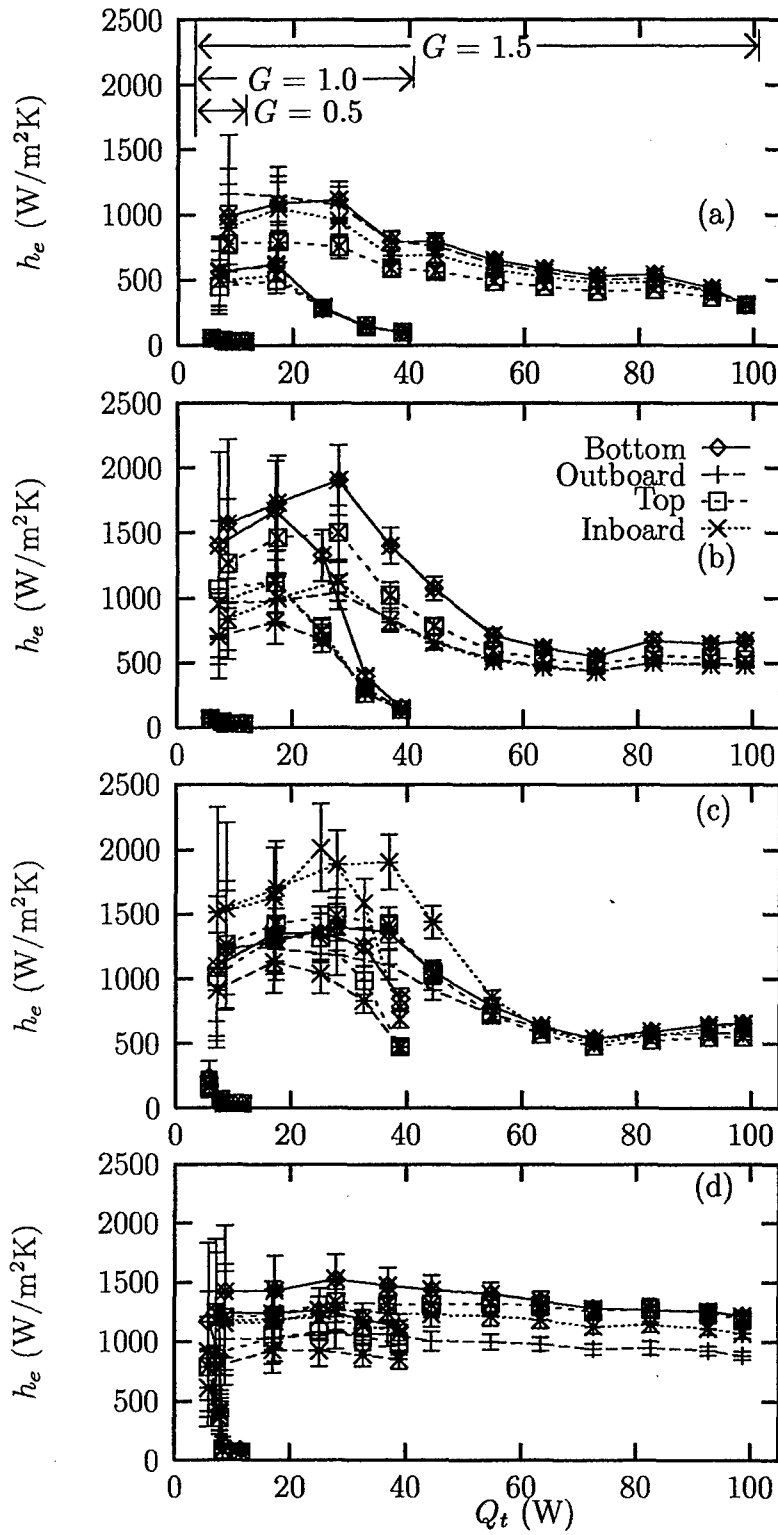


Figure 12: Heat transfer coefficients within the evaporator section versus transported heat for $|\vec{a}_r| = 0.01\text{-g}$: (a) $x = 54.0$ mm; (b) $x = 92.1$ mm; (c) $x = 130$ mm; (d) $x = 168$ mm.

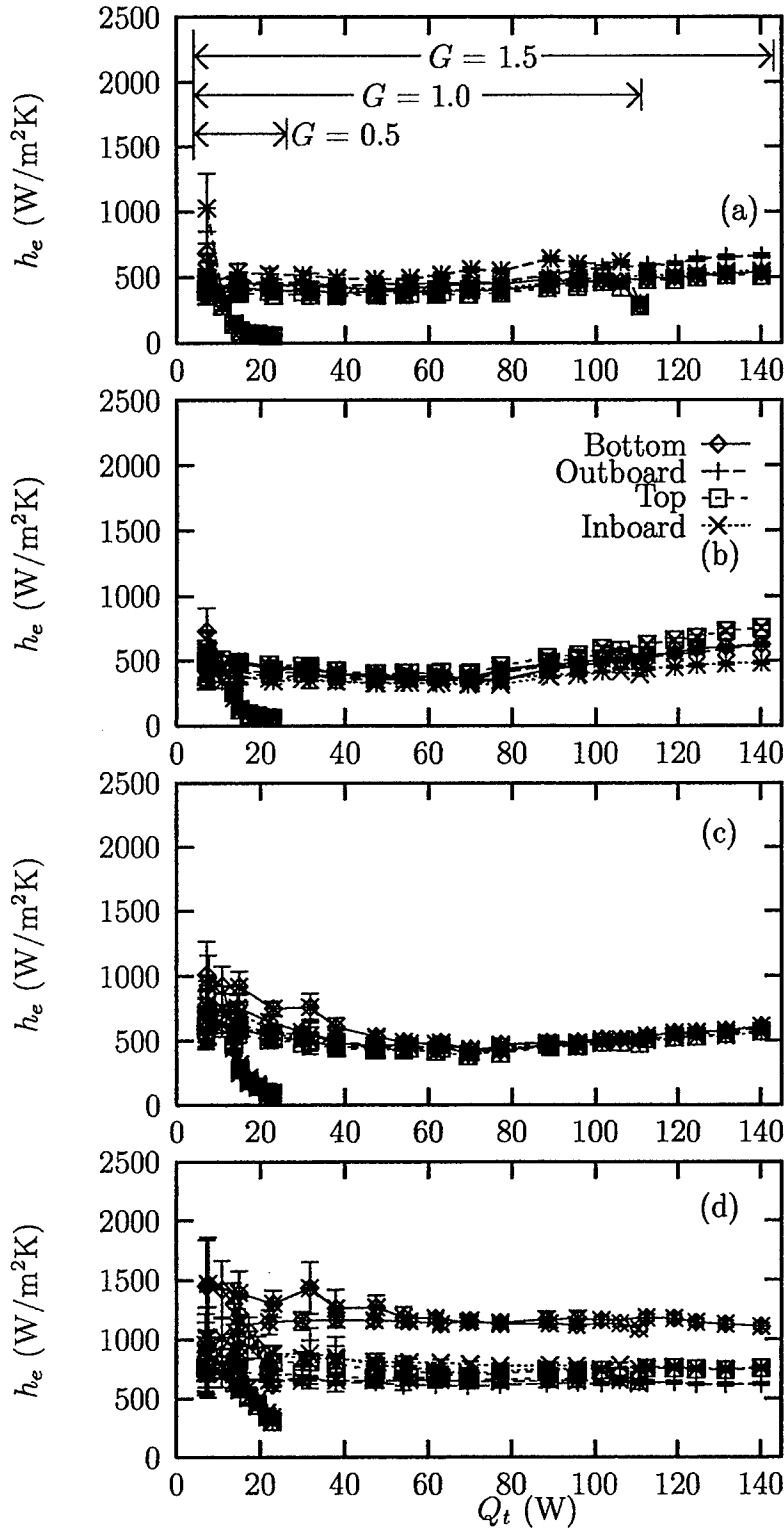


Figure 13: Heat transfer coefficients within the evaporator section versus transported heat for $|\vec{a}_r| = 10.0$ -g: (a) $x = 54.0$ mm; (b) $x = 92.1$ mm; (c) $x = 130$ mm; (d) $x = 168$ mm.

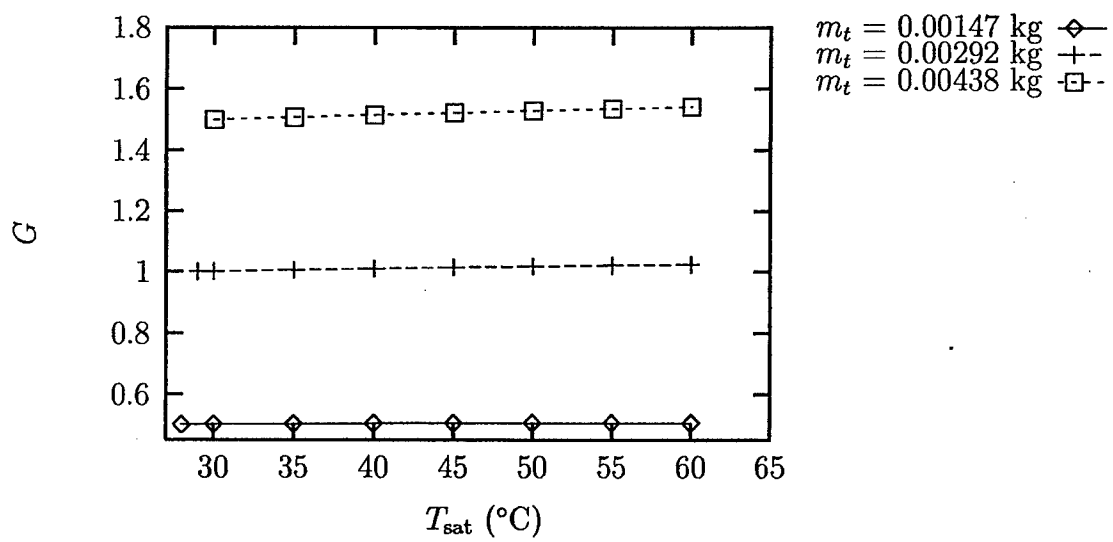


Figure 14: Ratio of liquid volume to total groove volume versus saturation temperature.

2 Fully-Developed Laminar Flow in Trapezoidal Grooves with Shear Stress at the Liquid-Vapor Interface

2.1 Abstract

This paper discusses the behavior of liquid flowing in a groove with a trapezoidal cross section. For fully developed laminar flow, the conservation of mass and momentum equations reduce to the classic Poisson equation in terms of the liquid velocity. A finite difference solution was employed to determine the mean velocity, volumetric flow rate, and Poiseuille number ($Po = fRe$) as functions of the groove aspect ratio, groove-half angle, meniscus contact angle and imposed shear stress at the liquid-vapor interface. Comparisons with existing solutions for fully developed flow in rectangular ducts and rectangular and triangular grooves are provided. The volumetric flow rate in a groove in which the fill amount varies is discussed. A semi-analytical solution and a two-point numerical solution for the mean velocity in a groove are presented and used to determine the capillary limit for a revolving helically-grooved heat pipe. The effects of interfacial shear stress and groove fill ratio on heat pipe performance are investigated.

2.2 Introduction

Internally grooved ducts are used in process equipment to improve heat transfer during condensation and evaporation. In some cases, such as a refrigeration cycle evaporator or condenser with internal grooves, the vapor flow is cocurrent with respect to the liquid flow. In axially grooved heat pipes, the vapor flow is countercurrent to the liquid flow. The interfacial shear stress due to the cocurrent or countercurrent vapor flow contributes to the liquid pressure drop, which can significantly affect the heat transfer capacity of the grooved surface. The objective of the present research was to numerically model the flow of liquid in trapezoidal grooves using a finite difference approach in order to provide accurate information on the effects of cocurrent and countercurrent vapor flow on the pressure drop in the liquid. This geometry was chosen due to the fact that rectangular and triangular grooves are special cases of the trapezoidal groove, thus making the analysis as general as possible.

DiCola [1] solved the conservation of momentum equation for the laminar flow of liquid

in rectangular grooves with a uniform shear stress imposed at the liquid-vapor interface using separation of variables. Unfortunately, this manuscript is no longer available in the open literature. Schneider and DeVos [2] provided the exact solution determined by DiCola [1], along with an expression for the friction factor which approximates the exact solution to within 1% by using the first term of the infinite series solution. This expression was used by Schneider and DeVos to determine the nondimensional heat transport capacity of axially-grooved heat pipes. Upon examination of the DiCola equation, it is obvious that the rectangular groove is completely full; i.e., the meniscus contact angle is $\phi = 90^\circ$.

Ayyaswamy et al. [3] used the Galerkin boundary method to solve the Poisson equation to determine the fluid velocity in triangular grooves. In this study, interfacial shear stress was zero, and the groove half-angle and contact angle were varied from $\theta = 5$ to 60° and $\phi = 0.1^\circ$ to the full groove condition ($\theta + \phi = 90^\circ$). The results were presented graphically and in tabular form, which included the cross-sectional area, mean velocity, hydraulic diameter, and Poiseuille number. It was found that the Poiseuille number increased monotonically with meniscus contact angle.

Ma et al. [4] determined the Poiseuille number for the flow of liquid in triangular grooves with liquid-vapor frictional interaction. The groove half-angle ranged from $20 \leq \theta \leq 60^\circ$ and the meniscus contact angle was varied from $\phi = 0$ to 60° . The conservation of momentum equation was transformed into the Laplace equation in terms of liquid velocity, which was solved using separation of variables and linear superposition. Difficulties were encountered with respect to application of the liquid-vapor interface boundary condition, since the liquid-vapor interface velocity is an unknown function of the vapor velocity. The methodology used to overcome this difficulty required an experimentally determined coefficient. A dimensionless liquid-vapor interface flow number was introduced to account for the interfacial shear stress. This value determined the relative velocities of the liquid and vapor at the liquid-vapor interface, which impacted the magnitude of the Poiseuille number. It was found that the friction factor increased with the interface flow number and contact angle. Results from the experiment executed by Ayyaswamy et al. [3] for no liquid-vapor shear stress showed an excellent comparison with the analytical solution over the ranges of groove half-angle and contact angle mentioned above.

Peterson and Ma [5] performed a follow-up analysis to that of Ma et al. in which the Poiseuille number for flow in triangular grooves was determined using the Nachtsheim-Swigert iteration scheme and a numerical solution of a two-point boundary value problem. This allowed the velocity distributions in both the liquid and vapor to be solved as a coupled problem. Channel angles of $\theta = 10^\circ, 20^\circ, 30^\circ$ and 40° and meniscus contact angles of $\phi = 0^\circ, 20^\circ, 40^\circ$ and 60° were analyzed. It was determined that the dimensionless liquid-vapor flow number (previously defined by Ma et al.) was a function of the vapor velocity and the fluid properties of the liquid and vapor. An experiment was devised to validate the results of the numerical model. It was shown that increasing the countercurrent vapor flow increases the friction factor of the liquid. The agreement between the experimental data and the numerical model was quite good.

Romero and Yost [6] analyzed the flow of liquid in a triangular groove with no shear stress at the liquid-vapor interface. In particular, the flow from a sessile drop into the groove was of interest. A nonlinear partial differential diffusion equation was presented which described the time-dependent height of liquid in the groove in terms of the groove geometry, meniscus contact angle, and fluid properties. A simplified similarity solution was presented for the region which was far from the sessile drop. A full similarity solution was also shown which accounted for the region near the fluid droplet. It was found that the wetting front position was proportional to $(Dt)^{1/2}$, where the diffusion coefficient D was related to the groove geometry, liquid viscosity, and liquid-vapor surface tension.

Lin and Faghri [7] modeled the flow of liquid in the triangular grooves of a rotating miniature heat pipe. A correlation for the friction factor was provided in terms of the shear stress at the liquid-vapor interface. The laminar flow in the triangular groove was solved using a finite element technique for side lengths ranging from $h\sqrt{1 + \tan^2 \theta} = 0.2$ to 0.65 mm and liquid-vapor shear stress $\tau_{lv} = 7.7 \times 10^{-5}$ to 0.055 N/m² for a groove half-angle of $\theta = 20^\circ$ and meniscus contact angle $\phi = 30^\circ$. A regression analysis was used to represent the data to within $\pm 2.8\%$.

Khrustalev and Faghri [8] analyzed the fully developed laminar flow of liquid and vapor in miniature heat pipes using a finite element solution. In particular, the case in which the vapor velocity was high and the cross-sectional areas of the vapor and liquid were comparable

was of interest. It was assumed that, with respect to the vapor flow, the liquid velocity at the liquid-vapor interface was zero. For the liquid flow, the shear stress at the interface was equal and opposite to that of the vapor. This meant that the velocity gradient in the liquid was related to that of the vapor via a ratio of absolute viscosities. The momentum equation for the vapor domain was first solved to determine the shear stress distribution at the liquid-vapor interface. Then the momentum equation for the liquid domain was solved using the shear stress information from the vapor solution. The results presented were for a specific heat pipe geometry that matched a previous experimental study. It was found that the shear stress at the liquid-vapor interface was not uniform, being greater near the point of contact with the solid groove wall. This effect was more significant for smaller values of meniscus contact angle. In addition, the shear stress at the interface became more uniform as the vapor space became more restricted.

Kolodziej et al. [9] analyzed the gravity-driven flow of liquid in a triangular groove with no shear at the liquid-vapor interface. The shape of the liquid-vapor interface was determined in terms of the Bond number and meniscus contact angle. Starting with the Young-Laplace relation, a nonlinear boundary-value problem for the liquid-vapor interface shape was solved. The flow field was then solved for the friction factor using the boundary collocation method. The range of parameters was as follows: groove half-angle $\theta = 5$ to 70° , meniscus contact angle $\phi = 5$ to 45° , and Bond number $Bo = \rho g b^2 / \sigma = 0.001, 0.01, 0.1, 1.0$ and 5.0 , where b is the vertical distance from the liquid-vapor interface to the bottom of the groove. It was found that the Bond number had a significant effect on the friction factor of the flow.

The objective of the present study was to determine the mean velocity, volumetric flow rate, and Poiseuille number for the flow of liquid in trapezoidal grooves. The effect of vapor flowing over the liquid-vapor interface was accounted for by relating the liquid velocity gradient to the friction factor of the vapor. This approach assumed that the liquid velocity did not affect the vapor velocity; i.e., the vapor velocity at the interface was zero. In addition, the variation of the shear stress along the liquid-vapor interface was neglected [8]. The conservation of momentum equation was solved using Gauss-Seidel iteration with successive over-relaxation. The analysis was validated using the results of several previous studies including the flow of liquid in rectangular and triangular grooves with liquid-vapor

interaction. The mean velocity, volumetric flow rate, and Poiseuille number are presented in terms of the groove aspect ratio ($0 \leq \beta \leq 1.5$), groove half-angle ($0 \leq \theta \leq 60^\circ$), meniscus contact angle ($0 \leq \phi \leq 90^\circ - \theta$), and dimensionless shear stress at the liquid-vapor interface ($-0.45 \leq \tau_{lv}^* \leq 5.0$). The results were used to determine the effects of groove fill amount on the capillary limit of the revolving helically-grooved heat pipe studied by Castle et al. [1]. The predictions of the improved capillary limit model were compared to the experimental data obtained.

2.3 Mathematical Model

A constant property liquid flows steadily in a trapezoidal groove as shown in Fig. 31. A meniscus, which is assumed to be circular, comprises the liquid-vapor interface. For fully developed laminar flow with no body forces, the dimensionless conservation of mass and momentum equations reduce to [11]

$$\frac{\partial^2 v^*}{\partial x^{*2}} + \frac{\partial^2 v^*}{\partial z^{*2}} = -1 \quad (10)$$

On the groove walls, the no-slip condition is in effect.

$$v^* = 0 : \begin{cases} 0 \leq x^* \leq \beta, & z^* = 0 \\ \beta \leq x^* \leq \beta + \tan \theta, & z^* = (x^* - \beta) \cot \theta \quad \text{for } \theta > 0 \\ x^* = \beta, & 0 \leq z^* \leq 1 \quad \text{for } \theta = 0 \end{cases} \quad (11)$$

At the line of symmetry, the velocity gradient is zero in the x^* direction

$$\frac{\partial v^*}{\partial x^*} = 0 : \quad x^* = 0, \quad 0 \leq z^* \leq (1 + d^*) - R^* \quad (12)$$

where

$$d^* = R^* \sqrt{1 - \left(\frac{\beta + \tan \theta}{R^*} \right)^2} \quad (13)$$

The dimensionless radius of curvature is given by

$$R^* = \begin{cases} (\beta + \tan \theta) \sqrt{1 + \left[\cot \theta - \frac{\sin \phi}{\sin \theta \sin(\theta + \phi)} \right]^{-2}} & \text{for } \theta > 0 \\ \beta \sec \phi & \text{for } \theta = 0 \end{cases} \quad (14)$$

On the liquid-vapor interface, a uniform shear stress in the y direction is imposed.

$$\frac{\partial v^*}{\partial n^*} = \tau_{lv}^* : 0 \leq x^* \leq \beta + \tan \theta, z^* = (1 + d^*) - \sqrt{R^{*2} - x^{*2}} \quad (15)$$

The dimensional liquid-vapor interface shear stress can be cast in terms of the friction factor of the vapor.

$$\tau_{lv} = \begin{cases} \left[\frac{\rho_v (\bar{v}_v)^2}{2} \right] f_v & \text{for cocurrent flow} \\ - \left[\frac{\rho_v (\bar{v}_v)^2}{2} \right] f_v & \text{for countercurrent flow} \end{cases} \quad (16)$$

The Poiseuille number of the liquid in the groove is given by

$$\text{Po} = f \text{Re} = \frac{D_h^{*2}}{2v^*} \quad (17)$$

The dimensionless hydraulic diameter is

$$D_h^* = \begin{cases} 2 \left[\beta + (\beta + \tan \theta) (1 + d^*) - R^{*2} \cos^{-1} \left(\frac{d^*}{R^*} \right) \right] (\beta + \sec \theta)^{-1} & \text{for } \theta + \phi < \pi/2 \\ 2 (2\beta + \tan \theta) (\beta + \sec \theta)^{-1} & \text{for } \theta + \phi = \pi/2 \end{cases} \quad (18)$$

The mean velocity is defined as

$$\bar{v}^* = \frac{2}{A_l^*} \int_0^{\beta + \tan \theta} \int_0^{z^*} v^* dz^* dx^* \quad (19)$$

where the dimensionless cross-sectional area is given by

$$A_l^* = \begin{cases} \beta + (\beta + \tan \theta) (1 + d^*) - R^{*2} \cos^{-1} \left(\frac{d^*}{R^*} \right) & \text{for } \theta + \phi < \pi/2 \\ 2\beta + \tan \theta & \text{for } \theta + \phi = \pi/2 \end{cases} \quad (20)$$

2.4 Numerical Model

The elliptic Poisson equation given in eqn. (44) with mixed boundary conditions [eqns. (45), (46) and (50)] was solved using Gauss-Seidel iteration with successive over-relaxation and a central differencing scheme [12]. The convergence criteria for the iterative solution was set to $\epsilon = 10^{-8}$ for each case. A grid independence check was made in which the number of grids in each direction was doubled. When the value for the Poiseuille number did not

change by more than 3%, grid independence was considered to be reached. The convergence criteria was then reduced by an order of magnitude while maintaining the highest number of grids. If the Poiseuille number did not change by more than 2%, the solution was considered to be independent of both grid size and ϵ . Otherwise, a grid independence check was made at the smaller value of ϵ until a converged solution was obtained. In fact, the grid independence for 423 of the 446 data points reported was less than 1% [13].

The numerical model was tested against several existing solutions, such as rectangular ducts, triangular grooves without interfacial shear stress, and rectangular and triangular grooves with shear stress. See Lykins [13] for details.

Shah [14] determined the friction factors for the laminar flow within ducts of various cross sections using a least-squares-matching technique. A comparison was made of the Poiseuille number between the present solution and those given by Shah [14] and Shah and London [15] for laminar flow in a family of rectangular ducts ($\theta = 0^\circ$, $0.01 \leq \beta \leq 1.0$). The agreement was excellent, with a maximum difference of 0.9%.

Ayyaswamy et al. [3] presented the friction factors obtained for laminar flow in triangular grooves using the Galerkin method of solution. Romero and Yost [6] derived an equation for the dimensionless volumetric flow rate of liquid in a triangular groove using asymptotic methods and a regression analysis. Kolodziej et al. [9] used the boundary collocation method to solve the same problem, except that the liquid-vapor interface was not assumed to be circular. The present solution was compared to that obtained by Ayyaswamy et al. for $\theta = 5^\circ$ and 60° for the full range of meniscus contact angle ($0.1^\circ \leq \phi \leq 90^\circ - \theta$). The agreement was excellent for $\theta = 60^\circ$, but was less so for $\theta = 5^\circ$. This was due to the extreme narrowness of the flow field for this case. The maximum percent differences for $\theta = 5^\circ$ and 60° were 3.7% and 0.9%, respectively. In comparison to the results by Romero and Yost [6], the maximum percent differences were 2.2% for $\theta = 5^\circ$ and 2.3% for $\theta = 60^\circ$. The agreement with the results provided by Kolodziej et al. for the lowest value of Bond number presented ($Bo = 0.001$) was less satisfactory, with a maximum percent difference of 4.5% for $\theta = 5^\circ$, and 19.9% for $\theta = 60^\circ$. This may be due to the approximate nature of the solution by Kolodziej et al., which was in terms of a truncated infinite summation.

DiCola [1] presented the solution for the Poiseuille number for the laminar flow of a

constant property fluid within a rectangular groove. While interfacial shear stress at the liquid-vapor interface was accounted for, the groove was assumed to be completely full, with a meniscus contact angle of $\phi = 90^\circ$. The comparison between the equation by DiCola and the results of the present analysis for laminar flow in a family of rectangular grooves at the full groove condition ($\phi = 90^\circ$, $0.1 \leq \beta \leq 1.0$, $\tau_{lv}^* = -0.1, 0.0$, and 1.0) resulted in an excellent agreement with a maximum percent difference of 2.3%.

The present model was compared to the correlation presented by Lin and Faghri [7], where the friction factor for the flow of liquid in triangular grooves with liquid-vapor shear was presented. Unfortunately, not enough information was provided by Lin and Faghri to precisely determine the limits of applicability for their equation. Therefore, the correlation was evaluated over a fairly wide range for comparison with the present solution. The agreement was quite good between $0.075 \leq -\tau_{lv}^* \leq 0.1$, where the maximum percent difference in this range was 2.2%.

2.5 Results and Discussion

2.5.1 Parametric Analysis

A numerical study has been completed in which the flow field in a trapezoidal groove has been solved. Specifically, values of the mean velocity, Poiseuille number, and volumetric flow rate are reported for various values of the groove aspect ratio, groove half-angle, meniscus contact angle, and dimensionless shear stress at the liquid-vapor interface. Figure 16 shows a contour plot of the dimensionless mean velocity obtained for cocurrent flow, no shear stress, and countercurrent flow. The flow behavior changes significantly with shear stress, where the maximum velocity is located along the liquid-vapor interface for $\tau_{lv}^* = 5.0$ and 0.0 , and within the interior of the flow field for $\tau_{lv}^* = -0.1$. For countercurrent flow [Fig. 16(c)], a region of reversed flow occurs near the intersection of the groove wall and the liquid-vapor interface. Depending on the magnitude of the countercurrent shear stress, the liquid velocity could be entirely reversed.

Figure 17 presents the mean velocity versus shear stress at the liquid-vapor interface for several values of the groove half-angle. The range of the meniscus contact angle ($0 \leq \phi \leq$

$90^\circ - \theta$) was divided equally to show the behavior of the mean velocity with ϕ . The mean velocity increases linearly with shear stress since the flow is aided by τ_{lv}^* . In addition, \bar{v}^* increases with groove half-angle and meniscus contact angle, which is a result of an increase in cross-sectional area. As the groove half-angle θ increases, \bar{v}^* becomes more sensitive to the meniscus contact angle ϕ due to the increased length of the perimeter of the liquid-vapor interface.

Figure 33 shows that the Poiseuille number decreases dramatically as the shear stress at the liquid-vapor interface increases. For countercurrent flow ($\tau_{lv}^* < 0$), the Poiseuille number is a strong function of shear stress since the mean velocity approaches zero. In addition, the Poiseuille number decreases with increasing meniscus contact angle for a given value of shear stress. For cocurrent flow ($\tau_{lv}^* > 0$), the Poiseuille number is a lesser function of the shear stress, but increases significantly with meniscus contact angle. The Poiseuille number is a weak function of the groove half-angle.

The volumetric flow rate versus shear stress for various meniscus contact angles can be seen in Fig. 19. The volumetric flow rate and mean velocity display similar trends. The volumetric flow rate is a linear function of shear stress, and increases with meniscus contact angle and groove half-angle. The flow rate is slightly more sensitive than the mean velocity with respect to the meniscus contact angle. The mean velocity is given as a function of the interfacial shear stress for a constant meniscus contact angle in Fig. 20. For $\theta = 0$ and 30° , the mean velocity increases and then decreases with groove aspect ratio. This point can be further elucidated in Fig. 21, which presents the mean velocity, Poiseuille number and volumetric flow rate for $\phi = 30^\circ$ and $\tau_{lv}^* = 5.0$. As mentioned previously, the mean velocity increases and then decreases with β for $\theta \leq 30^\circ$. This phenomenon also impacts the Poiseuille number and the volumetric flow rate, where \dot{V}^* attains a maximum value with respect to β for a given groove half-angle $\leq 15^\circ$. Figure 22 shows \bar{v}^* , Po, and \dot{V}^* versus θ for $\beta = 1.0$ and $\tau_{lv}^* = 5.0$. In general, these functions increase significantly with both meniscus contact angle and groove half-angle, except for the Poiseuille number for $\theta = 0^\circ$ and $\phi \leq 20^\circ$.

2.5.2 Semi-Analytical and Two-Point Numerical Solutions for \overline{v}^*

As seen in Figs. 17 and 20, the mean velocity is a linear function of the imposed shear stress at the liquid-vapor interface. Since a direct numerical simulation of the liquid flow field for a number of values of the shear stress is computer resource intensive, it is appropriate to seek a semi-analytical expression for \overline{v}^* . Figure 23(a) shows the definition of the parameters involved, where the mean velocity when the shear stress is zero ($0, \overline{v}_0^*$) is given by the numerical solution. The value for the liquid-vapor shear for which the mean velocity is zero ($\tau_{lv,0}^*, 0$) is given by the following force balance analysis. Figure 23(b) shows a differential element of the liquid in the groove. A force balance between the pressure drop and the shear forces at the liquid-vapor interface and at the wall results in the following relation.

$$p_y A_l - p_{y+dy} A_l + \tau_{lv} A_{lv} - \overline{\tau}_w A_w = 0 \quad (21)$$

The areas over which the shear stresses τ_{lv} and $\overline{\tau}_w$ act are $A_{lv} = P_{lv} dy$ and $A_w = P dy$, respectively. Using these areas and nondimensionalizing gives

$$A_l^* + \tau_{lv}^* P_{lv}^* - \overline{\tau}_w^* P^* = 0 \quad (22)$$

For Poiseuille flow in ducts of arbitrary cross section, and combined Couette-Poiseuille flow between flat plates, the shear stress at the wall is related to the mean velocity of the fluid by a constant [11]. In the present analysis, it is assumed that this also holds for the flow of liquid in a trapezoidal groove with an imposed shear stress at the liquid-vapor interface.

$$\overline{\tau}_w^* = C_1 \overline{v}^* \quad (23)$$

It should be noted that the constant C_1 is probably a function of the groove geometry and meniscus contact angle. However, since the objective of this analysis is to determine the liquid-vapor shear stress when the mean liquid velocity is zero, this functionality is unimportant.

Substituting this relation into the force balance equation results in the following expression for mean velocity

$$\overline{v}^* = \frac{1}{C_1 P^*} (A_l^* + \tau_{lv}^* P_{lv}^*) \quad (24)$$

where the perimeter of the liquid-vapor interface is

$$P_{lv}^* = \begin{cases} 2R^* \sin^{-1} \left(\frac{\beta + \tan \theta}{R^*} \right) & \text{for } \theta + \phi < \pi/2 \\ 2(\beta + \tan \theta) & \text{for } \theta + \phi = \pi/2 \end{cases} \quad (25)$$

The mean velocity is zero when the shear stress at the liquid-vapor interface is

$$\tau_{lv,0}^* = -\frac{A_l^*}{P_{lv}^*} \quad (26)$$

Figures 24(a) and 24(b) show the results of eqn. (26). The numerical results shown in Figs. 17 and 20 were extrapolated to determine the values for shear stress at the liquid-vapor interface when $\bar{v}^* = 0$. The prediction given by eqn. (26) is quite good given the simplicity of the closed-form solution. The equation for the normalized mean velocity as a function of the shear stress is given by

$$v' = \bar{v}^*/\bar{v}_0^* = 1 - \tau' \quad (27)$$

where $\tau' = \tau_{lv}^*/\tau_{lv,0}^*$. The semi-analytical solution for the normalized mean velocity is shown in Fig. 24(c) with the corresponding numerical data presented in Figs. 17 and 20. Equation (27) predicts 93% of the data to within $\pm 30\%$ over the range of the meniscus contact angle, groove half-angle, groove aspect ratio and liquid-vapor shear stress examined in Figs. 17 and 20.

The two-point numerical solution of \bar{v}^* as a function of τ_{lv}^* is also shown in Fig. 23(a). The finite difference numerical model is used to compute the mean velocity for two values of liquid-vapor shear stress $[(0, \bar{v}_0^*) \text{ and } (\tau_{lv,a}^*, \bar{v}_a^*)]$. The equation for the normalized mean velocity as a function of shear stress using this solution is given by eqn. (27), and the shear stress when the mean velocity is zero is

$$\tau_{lv,0}^* = \frac{\tau_{lv,a}^*}{(1 - \bar{v}_a^*/\bar{v}_0^*)} \quad (28)$$

2.5.3 Effect of Groove Fill Ratio

Figure 25(a) shows the case when liquid evaporates from a trapezoidal groove. Initially, the groove is full with $\phi + \theta = 90^\circ$. The contact angle decreases until the minimum meniscus contact angle ϕ_0 for the particular solid-liquid combination is reached. Past this point, the

meniscus detaches from the top of the groove and recedes until the lowest part of the meniscus reaches the bottom of the groove [16]. When the thickness of the liquid film at the bottom of the groove is on the order of several hundred Angstroms, forces due to London-van der Waals interactions with the surrounding liquid and solid molecules induce instabilities in the fluid [17]. These instabilities cause the liquid in the groove to bifurcate into two separate flows in the corners of the groove, which are each equivalent to the flow in a triangular groove. The liquid in the two corners of the groove will continue to recede until it is depleted.

The dimensions of the grooves analyzed by Castle et al. [1] were used to determine the volumetric flow rate of ethanol in a trapezoidal copper groove as a function of the amount of liquid in the groove. The geometric values of the parametric analysis depicted in Fig. 25(a) are given by Lykins [13]. Faghri [7] gives $\phi_0 = 7^\circ$ for a receding meniscus of ethanol on copper. In terms of the present analysis, as the liquid recedes into the groove, the groove aspect ratio β increases. In addition, after bifurcation occurs $\beta = 0$, and the groove half-angle θ changes to that of the corner of the groove. A relation for the point at which bifurcation occurs is provided where the liquid is assumed to bifurcate when the lowest part of the meniscus actually reaches the bottom of the groove. The radius of curvature at the bifurcation point for a trapezoidal groove is

$$R_b^* = \frac{1}{2} [1 + (\beta + \tan \theta)^2] \quad (29)$$

The meniscus contact angle at bifurcation as a function of the groove geometry is

$$\phi_b = \tan^{-1} \left(\frac{1}{\sin \theta} \left\{ \left[\cos \theta + \frac{2 \sin \theta (\beta + \tan \theta)}{1 - (\beta + \tan \theta)^2} \right]^{-1} - \cos \theta \right\} \right)^{-1} \quad (30)$$

The radius of curvature of the liquid-vapor interface is shown in Fig. 26(a) as a function of the groove fill ratio. When the groove is nearly full, the radius of curvature approaches infinity. As the amount of liquid in the groove decreases, the radius of curvature is relatively constant, and then becomes very small after the liquid bifurcates into the corners of the groove. Figures 26(b) and 26(c) show two flow parameters, F_1 and F_2 , which allow the presentation of the mean velocity and volumetric flow rate before and after bifurcation on the same graph. Both flow parameters increase monotonically with groove fill ratio, as expected. In Fig. 26(c), for a groove fill ratio of $A_l/A_g = 0.158$, the volumetric flow rate was 1% of that for the full groove due to the decrease in flow area. This figure shows that

the groove was essentially shut off for $A_l/A_g \leq 0.158$, which was prior to bifurcation. Using the functional relationship for mean velocity given by eqn. (24), the volumetric flow rate is

$$\dot{V}^* = \frac{A_l^*}{C_1 P^*} (A_l^* + \tau_{lv}^* P_{lv}^*) \quad (31)$$

When $\tau_{lv}^* = 0$, $\dot{V} \propto A_l^2$, which confirms that the volumetric flow rate should decrease rapidly with decreasing flow area for $A_l < 1$.

2.5.4 Capillary Limit Analysis for a Revolving Helically-Grooved Heat Pipe

Using the results of the numerical analysis, the capillary limit prediction for a revolving helically-grooved heat pipe proposed by Thomas et al. [3] was improved by accounting for the effects of working fluid fill amount and the shear stress at the liquid-vapor interface. The improved model was compared to the experimental data collected by Castle et al. [1], who determined the capillary limit of a revolving helically-grooved copper-ethanol heat pipe for radial accelerations of $|\vec{a}_r| = 0.01, 2.0, 4.0, 6.0, 8.0$ and 10.0 -g and groove fill ratios of $V_l/V_g = 0.5, 1.0$ and 1.5 . The dimensions of the heat pipe examined by Castle et al. [1] are given in Table 5. A pressure balance within the heat pipe results in the following expression for the capillary limit ([7], [20])

$$\Delta p_{\text{cap,max}} \geq \Delta p_v + \Delta p_l + \Delta p_{\text{bf}} \quad (32)$$

The maximum capillary pressure for an axial groove is

$$\Delta p_{\text{cap,max}} = \frac{\sigma}{R_c} \quad (33)$$

It is assumed that the capillary limit occurs when the liquid bifurcates into the corners of the grooves. This statement is based on the results of the variation of the volumetric flow rate with groove fill ratio in Fig. 26. The capillary radius when the liquid bifurcates ($R_c = 0.02252$ cm) was found using eqns. (29) and (30).

For a circular cross section heat pipe with uniform heat input and output along the lengths of the evaporator and condenser, respectively, the pressure drop in the vapor is

$$\Delta p_v = \frac{8\mu_v L_{\text{eff}} \dot{Q}_t}{\pi \rho_v h_{fg} R_v^4} \quad (34)$$

The pressure drop in the liquid was found by using the normalized mean velocity relation [eqn. (27)] rewritten in dimensional form.

$$dp_l = - \left(\frac{\mu_l \bar{v}_l}{h_l^2 v_0^*} + \frac{\tau_{lv}}{h_l \tau_{lv,0}^*} \right) dy \quad (35)$$

In a heat pipe, the liquid flows opposite to the vapor in all regions. Therefore, the shear stress at the liquid-vapor interface for countercurrent flow was used [eqn. (16)]. The Poiseuille number of the vapor flow was modeled as laminar flow within a smooth tube with a circular cross section ($Po_v = 16$). Substituting these relations into eqn. (35) gives

$$dp_l = - \left(\frac{\mu_l \bar{v}_l}{h_l^2 v_0^*} - \frac{4\mu_v \bar{v}_v}{h_l R_v \tau_{lv,0}^*} \right) dy \quad (36)$$

It is assumed that the cross-sectional area of the liquid is constant along the length of the groove. For a constant heat flux in both the evaporator and condenser sections, eqn. (36) can be integrated to determine the total pressure drop in the helical groove.

$$\Delta p_l = L_{\text{eff}} \left(\frac{\mu_l \bar{v}_{l,\text{max}}}{h_l^2 v_0^*} - \frac{4\mu_v \bar{v}_{v,\text{max}}}{h_l R_v \tau_{lv,0}^*} \right) \sqrt{\left(\frac{2\pi R_h}{L_p} \right)^2 + 1} \quad (37)$$

The maximum liquid velocity in a groove is

$$\bar{v}_{l,\text{max}} = \frac{\dot{Q}_g}{\rho_l A_l h_{fg}} \quad (38)$$

Similarly, the maximum vapor velocity is

$$\bar{v}_{v,\text{max}} = \frac{\dot{Q}_t}{\pi R_v^2 \rho_v h_{fg}} \quad (39)$$

where the total heat transported by the heat pipe accounts for the contributions by all of the individual grooves. Using the above relations, the liquid pressure drop in a groove as a function of the transported heat is

$$\Delta p_l = \frac{L_{\text{eff}}}{h_{fg}} \left(\frac{\mu_l \dot{Q}_g}{h_l^2 v_0^* \rho_l A_l} - \frac{4\mu_v \dot{Q}_t}{\pi h_l R_v^3 \rho_v \tau_{lv,0}^*} \right) \sqrt{\left(\frac{2\pi R_h}{L_p} \right)^2 + 1} \quad (40)$$

The body forces imposed on the fluid within a particular groove may either aid or hinder the return of the fluid to the evaporator, depending on the groove pitch L_p and the circumferential location of the starting point of the helical groove ([3], [2]). However, even if the

body force hinders the return of the fluid, each groove contributes to the heat transported \dot{Q}_t . Therefore, the capillary limit equation [eqn. (32)] was first solved for the heat transported by each individual groove \dot{Q}_g , and the results were summed to determine the total heat transport \dot{Q}_t . Since the pressure drop in the vapor space and the pressure drop in each groove were functions of the total heat transport, eqn. (32) was solved iteratively. The body forces due to acceleration and gravity were integrated over the length of the groove to find the average pressure drop [3].

$$\Delta p_{bf} = -\rho_l \left[\int_0^{L_t} \hat{e}_{x3} \cdot \left(-\vec{A} + \{-g\} \hat{e}_{z1} \right) ds \right] \sqrt{\left(\frac{2\pi R_h}{L_p} \right)^2 + 1} \quad (41)$$

Combining the above relations, the general expression for the maximum capillary limit for a single helical groove which accounts for shear stress at the liquid-vapor interface and the effect of groove fill ratio is given by

$$\begin{aligned} \frac{\sigma}{R_c} \geq \frac{L_{eff}}{h_{fg}} \left\{ \frac{8\mu_v \dot{Q}_t}{\pi \rho_v R_v^4} + \left(\frac{\mu_l \dot{Q}_g}{h_l^2 v_0^* \rho_l A_l} - \frac{4\mu_v \dot{Q}_t}{\pi h_l R_v^3 \rho_v \tau_{lv,0}^*} \right) \sqrt{\left(\frac{2\pi R_h}{L_p} \right)^2 + 1} \right\} \\ - \rho_l \left[\int_0^{L_t} \hat{e}_{x3} \cdot \left(-\vec{A} + \{-g\} \hat{e}_{z1} \right) ds \right] \sqrt{\left(\frac{2\pi R_h}{L_p} \right)^2 + 1} \end{aligned} \quad (42)$$

A closed-form solution for the capillary limit of a heat pipe with straight axial grooves and no body forces can be derived from eqn. (42).

$$\dot{Q}_{cap} = \frac{\sigma h_{fg}}{R_c L_{eff}} \left[\frac{\mu_l}{N_g h_l^2 v_0^* \rho_l A_l} + \frac{8\mu_v}{\pi \rho_v R_v^4} \left(1 - \frac{R_v}{2h_l \tau_{lv,0}^*} \right) \right]^{-1} \quad (43)$$

Figure 27(a) shows the results of the closed-form solution [eqn. (43)]. The groove geometry given by Castle et al. [1] was used, except that straight axial grooves were assumed ($L_p \rightarrow \infty$) instead of helical grooves. Over the range of groove fill ratio examined, the capillary limit increased with A_l/A_g by more than three orders of magnitude. For this case, the semi-analytical solution and the two-point numerical solution were nearly identical due to the low vapor velocities, and hence the low liquid-vapor shear stress. This point is further demonstrated in Fig. 27(a) by the graph indicated by "No Shear," where the term in eqn. (43) that accounts for the effect of liquid-vapor shear on the liquid was dropped by allowing $\tau_{lv,0}^* \rightarrow -\infty$. The capillary limit decreases when shear stress is accounted for, as expected.

Figure 27(b) shows the closed-form solution when water is the working fluid. In this case, the difference between the results of the two-point numerical solution and the no-shear solution is much more pronounced due to the significantly higher vapor velocities involved. The agreement between the semi-analytical solution and the two-point numerical solution is quite good. The semi-analytical solution offers very close results with a significantly reduced amount of computer resources required.

The capillary limit prediction for the helically-grooved heat pipe given by eqn. (42) is shown in Fig. 28 using the semi-analytical solution [eqn. (26)] for $|\vec{a}_r| = 0.0$ and 10.0-g. The capillary limit heat transport increases both with groove fill ratio and working temperature. In addition, \dot{Q}_{cap} increases significantly with the radial acceleration due to the improved liquid pumping ability of the helical grooves [3].

The experimental data collected by Castle et al. [1] for the capillary limit of a revolving helically-grooved heat pipe versus radial acceleration rates are shown in Fig. 29, along with the predictions of the present semi-analytical model and that given by Castle et al. [1]. During the experiments, the working temperature was not held constant, so the present model was evaluated at the saturation temperature reported for a given value of radial acceleration. For a groove fill ratio of $A_l/A_g = 0.5$ [Fig. 29(a)], the present model more closely matches the experimental data than the model by Castle et al. [1], which did not account for the groove fill ratio or liquid-vapor shear stress. For $A_l/A_g = 1.0$ [Fig. 29(b)], the present model significantly overpredicts the experimental data and the previous model, but matches the trend in the data quite well, given the simplicity of the model.

2.6 Conclusions

A numerical study has been concluded where the mean velocity, Poiseuille number, and volumetric flow rate of liquid in a trapezoidal groove have been determined as functions of groove geometry, meniscus contact angle and shear stress at the liquid-vapor interface. The mean velocity and volumetric flow rate have been shown to be linear functions of shear stress, and the Poiseuille number is a strong function of the shear stress for countercurrent flow. A semi-analytical solution and a two-point numerical solution for the mean velocity were presented and used to predict the capillary limit of a revolving helically-grooved heat

pipe for various groove fill ratios. Interfacial shear stress due to countercurrent flow in a heat pipe decreases the maximum heat transport. For cases in which the vapor velocities are high, this effect is more pronounced. The groove fill ratio was shown to have a significant impact on heat pipe performance. Underfilling the heat pipe examined by 10% resulted in a decrease in the predicted capillary limit by approximately 17 to 20% for water and ethanol, respectively.

2.7 Nomenclature

A_g	cross-sectional area of the groove, m^2
A_l	cross-sectional area of the liquid, m^2
A_{lv}	area of the liquid-vapor interface, m^2
A_w	area of the groove wall, m^2
A_l^*	A_l/h^2
\vec{a}_r	radial acceleration vector, m/s^2
\vec{A}	acceleration vector at any point in the helical groove, m/s^2
b	distance from the liquid-vapor interface to the bottom of the groove, m
Bo	Bond number, $\rho g b^2 / \sigma$
d^*	parameter defined in eqn. (48)
D	diffusion coefficient
D_h	hydraulic diameter, $4A_l/P$, m
D_h^*	D_h/h
F_1	mean velocity parameter, $h_l^2 \bar{v}^*$, m^2
F_2	volumetric flow rate parameter, $h_l^4 \dot{V}^*$, m^4
f	friction coefficient, $2\bar{\tau}_w / \rho \bar{v}^2$
g	acceleration due to gravity, m/s^2
h	groove height, m
h_{fg}	heat of vaporization, J/kg
h_l	height of the liquid in the groove at the wall, m
L_a	adiabatic length, m
L_c	condenser length, m

L_e	evaporator length, m
L_{eff}	effective heat pipe length, $L_e/2 + L_a + L_c/2$, m
L_p	pitch length, m
L_t	total heat pipe length, m
n	coordinate normal to the liquid-vapor interface
n^*	n/h
N_g	number of grooves
p	pressure, N/m ²
P	wetted perimeter, m
P_{lv}	perimeter of the liquid-vapor interface, m
P^*	P/h
P_{lv}^*	P_{lv}/h
Po	Poiseuille number, $f\text{Re}$
\dot{Q}_{cap}	capillary limit heat transport, W
\dot{Q}_g	heat transfer due to a single groove, W
\dot{Q}_t	total heat transported, $\sum_{i=1}^{N_g} \dot{Q}_{g,i}$, W
R	radius of curvature of the liquid-vapor interface, m
R_c	capillary radius, m
R_h	radius of the helix, m
R_v	radius of the heat pipe vapor space, m
R^*	R/h
R_b^*	dimensionless radius of curvature at bifurcation
Re	Reynolds number, $\rho \bar{v} D_h / \mu$
t	time, s
T_{sat}	saturation temperature, K
v	y -direction velocity, m/s
\bar{v}	mean y -direction velocity, m/s
$\bar{v}_{l,\text{max}}$	maximum mean liquid velocity, m/s
$\bar{v}_{v,\text{max}}$	maximum mean vapor velocity, m/s
v^*	$\mu v / h^2 (-dp/dy)$

$\overline{v^*}$	dimensionless mean y -direction velocity
$\overline{v_0^*}$	dimensionless mean y -direction velocity when $\tau_{lv}^* = 0$
$\overline{v_0^*}$	dimensionless mean y -direction velocity when $\tau_{lv}^* = 0$
$\overline{v_a^*}$	dimensionless mean y -direction velocity when $\tau_{lv}^* = \tau_{lv,a}^*$
v'	normalized mean velocity, $\overline{v^*}/\overline{v_0^*}$
V_g	total groove volume, m^3
V_l	liquid inventory volume, m^3
\dot{V}	volumetric flow rate, $\overline{v}A_l$, m^3/s
\dot{V}^*	$\mu\dot{V}/[h^4(-dp/dy)]$
w	width of the bottom of the groove, m
w_l	width of the liquid in the groove, m
x, y, z	coordinate directions
x^*	x/h
z^*	z/h
β	groove aspect ratio, $w/2h$
ϵ	convergence criteria
θ	groove half-angle, rad
μ	absolute viscosity, $\text{Pa}\cdot\text{s}$
ρ	density, kg/m^3
σ	surface tension, N/m
τ'	normalized shear stress at the liquid-vapor interface, $\tau_{lv}^*/\tau_{lv,0}^*$
τ_{lv}	shear stress at the liquid-vapor interface, N/m^2
τ_{lv}^*	$\tau_{lv}/h(-dp/dy)$
$\tau_{lv,0}^*$	shear stress at the liquid-vapor interface when $\overline{v^*} = 0$
$\tau_{lv,a}^*$	shear stress value in Fig. 23(a)
$\overline{\tau_w}$	average shear stress at the wall, N/m^2
$\overline{\tau_w^*}$	$\overline{\tau_w}/h(-dp/dy)$
ϕ	meniscus contact angle, rad
ϕ_0	minimum meniscus contact angle, rad
ϕ_b	meniscus contact angle at bifurcation, rad

References

- [1] G. DiCola, Soluzione analitica, amezzo della trasformata di Fourier, di un problema di fusso in un canale rettangolare, *Euratom C.C.R.*, Ispra, Italy, C.E.T.I.S. (1968).
- [2] G. Schneider and R. DeVos, Non-dimensional analysis for the heat transport capability of axially grooved heat pipes including liquid/vapor interaction, AIAA Paper No. 80-0214 (1980).
- [3] P. Ayyaswamy, I. Catton and D. Edwards, Capillary flow in triangular grooves, *ASME J. Appl. Mech.* **41**, 332-336 (1974).
- [4] H. Ma, G. Peterson, and X. Lu, The influence of vapor-liquid interactions on the liquid pressure drop in triangular microgrooves, *Int. J. Heat Mass Transfer* **37**, 2211-2219 (1994).
- [5] G. Peterson and H. Ma, Analysis of countercurrent liquid-vapor interactions and the effect on the liquid friction factor, *Experimental Thermal and Fluid Science* **12**, 13-24 (1996).
- [6] L. Romero and F. Yost, Flow in an open channel, *J. Fluid Mech.* **322**, 109-129 (1996).
- [7] L. Lin and A. Faghri, Steady-state performance of a rotating miniature heat pipe, *AIAA J. Thermophysics Heat Transfer* **11**, 513-518 (1997).
- [8] D. Khrustalev and A. Faghri, Coupled liquid and vapor flow in miniature passages with micro grooves, *ASME J. Heat Transfer* **121**, 729-733 (1999).
- [9] J. Kolodziej, G. Musielak, M. Kaczmarek and T. Strek, Determination of free surface and gravitational flow of liquid in triangular groove, *Computational Mechanics* **24**, 110-117 (1999).
- [10] R. Castle, S. Thomas and K. Yerkes, The effect of working fluid inventory on the performance of revolving helically-grooved heat pipes, *Proceedings of the 2000 National*

Heat Transfer Conference, Paper No. NHTC2000-12268, Pittsburgh, PA, accepted for publication in *ASME J. Heat Transfer* (2000).

- [11] F. White, *Viscous Fluid Flow* (2nd Edn), McGraw-Hill, New York (1991).
- [12] R. Burden and J. Faires, *Numerical Analysis* (3rd Edn), PWS Publishers, Boston (1985).
- [13] R. Lykins, Numerical analysis of fully developed laminar flow in trapezoidal and sinusoidal grooves with shear stress at the liquid vapor interface, Masters Thesis, Wright State University, Dayton, Ohio (2000).
- [14] R. Shah, Laminar flow friction and forced convection heat transfer in ducts of arbitrary geometry, *Int. J. Heat Mass Transfer* **18**, 849-862 (1975).
- [15] R. Shah and A. London, *Laminar Flow Forced Convection in Ducts*, Academic, New York (1978).
- [16] R. Hopkins, A. Faghri and D. Khrustalev, Flat miniature heat pipes with micro capillary grooves, *ASME J. Heat Transfer* **121**, 102-109 (1999).
- [17] E. Ruckenstein and R. Jain, Spontaneous rupture of thin liquid films, *J. Chem. S.* **70**, 132-147 (1974).
- [18] A. Faghri, *Heat Pipe Science and Technology*, Taylor and Francis, Washington, D.C. (1995).
- [19] S. Thomas, K. Klasing and K. Yerkes, The effects of transverse acceleration-induced body forces on the capillary limit of helically grooved heat pipes, *ASME J. Heat Transfer* **120**, 441-451 (1998).
- [20] S. Chi, *Heat Pipe Theory and Practice: A Sourcebook*, Hemisphere Publ. Corp., New York (1976).
- [21] K. Klasing, S. Thomas and K. Yerkes, Prediction of the operating limits of revolving helically-grooved heat pipes, *ASME J. Heat Transfer* **121**, 213-217 (1999).

Table 5: Specifications of the heat pipe test article examined by Castle et al. [1].

Groove Height, h	0.03831 cm
Groove Base Width, w	0.03445 cm
Groove Half-Angle, θ	14.62°
Evaporator Length, L_e	15.2 cm
Adiabatic Length, L_a	8.2 cm
Condenser Length, L_c	15.2 cm
Vapor Space Radius, R_v	0.6795 cm
Number of Grooves, N_g	50
Helical Pitch Length, L_p	135.8 cm
Helix Radius, R_h	0.6992 cm

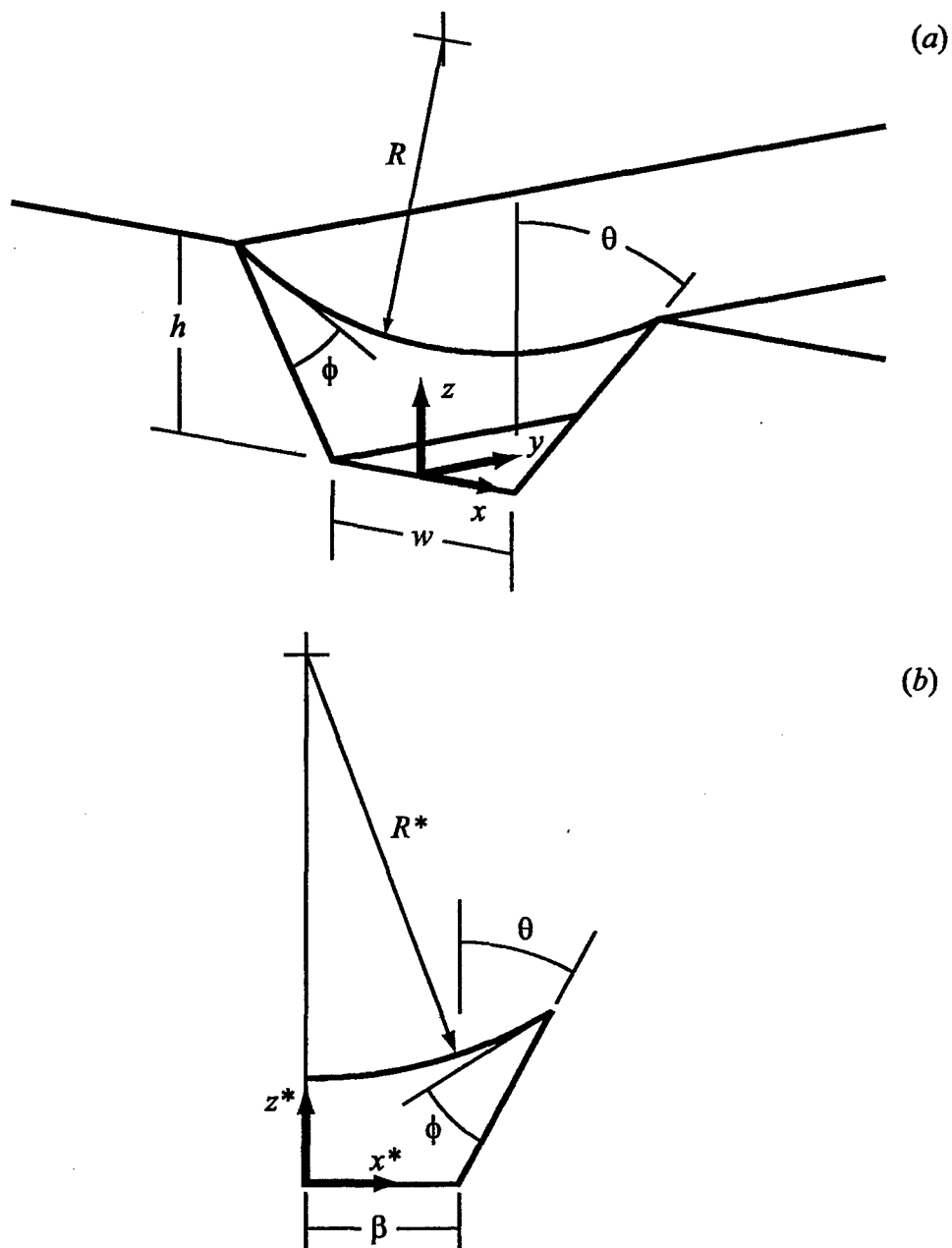


Figure 15: Flow of liquid in a trapezoidal groove: (a) Coordinate system; (b) Solution domain.

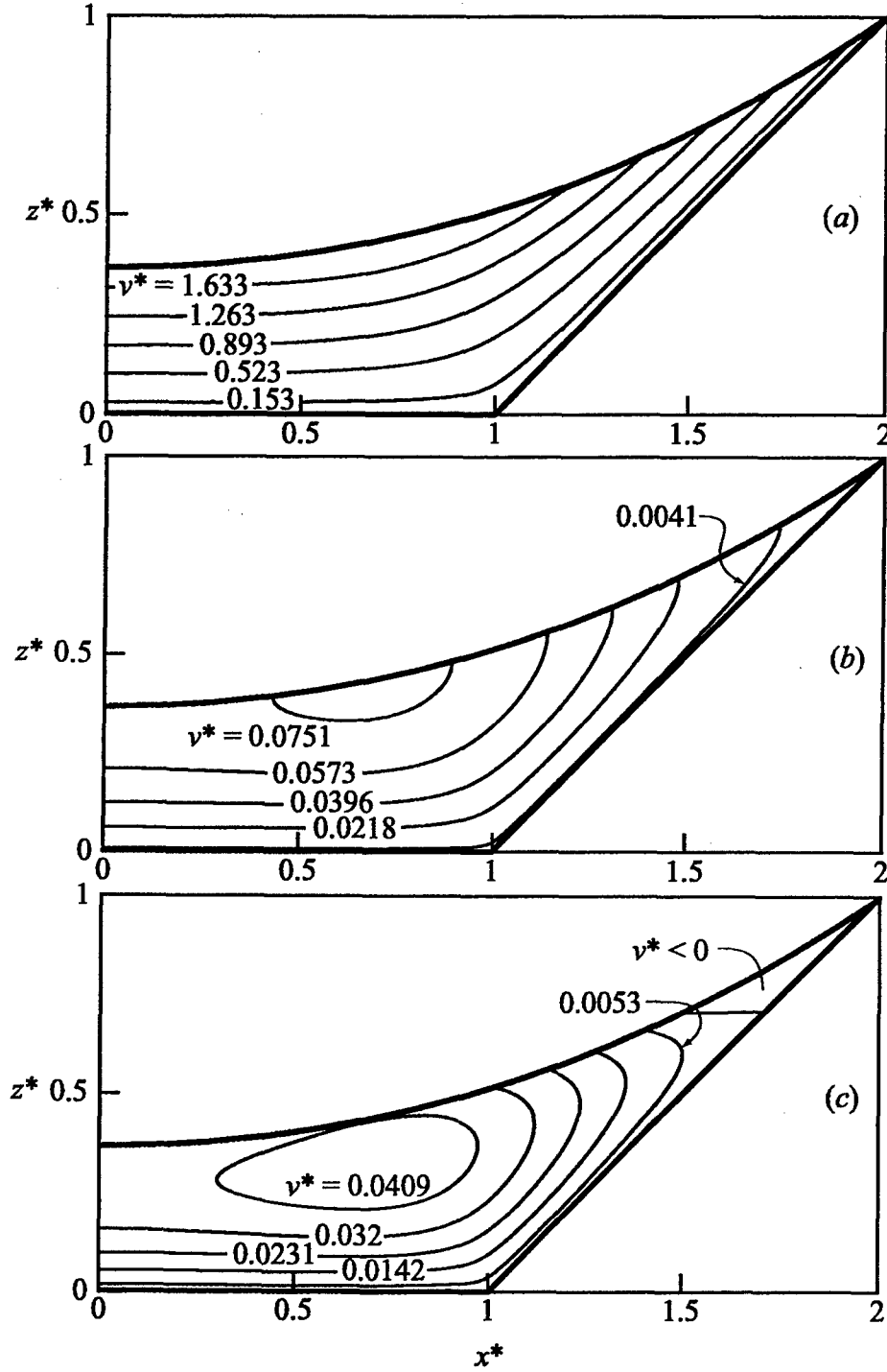


Figure 16: Dimensionless velocity fields for laminar flow in trapezoidal grooves ($\beta = 1.0$, $\phi = 10^\circ$, $\theta = 45^\circ$): (a) $\tau_{lv}^* = 5.0$ (cocurrent flow); (b) $\tau_{lv}^* = 0.0$; (c) $\tau_{lv}^* = -0.1$ (countercurrent flow).

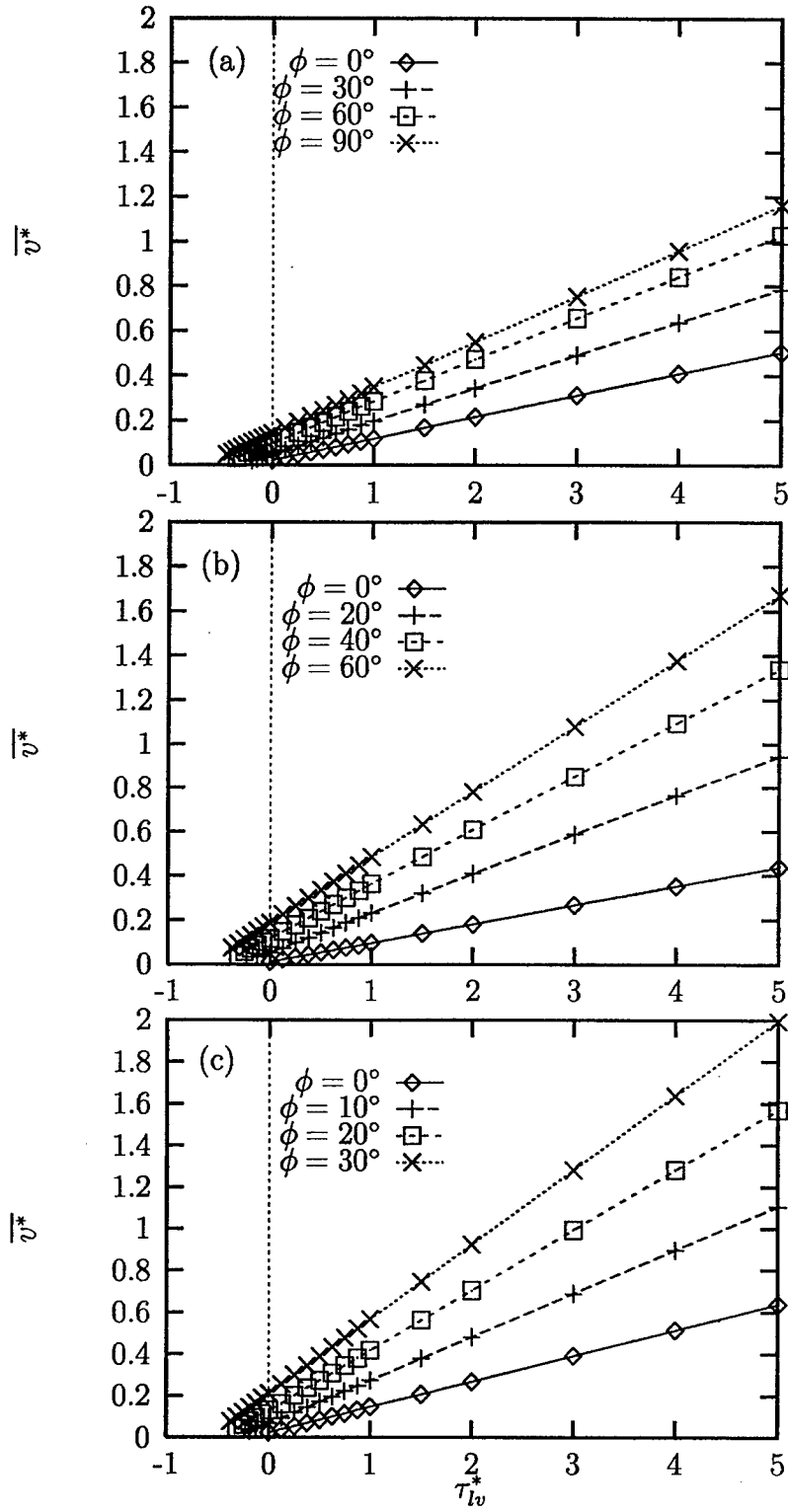


Figure 17: \overline{v}^* versus τ_{lv}^* for laminar flow in trapezoidal grooves ($\beta = 1.0$): (a) $\theta = 0^\circ$; (b) $\theta = 30^\circ$; (c) $\theta = 60^\circ$.

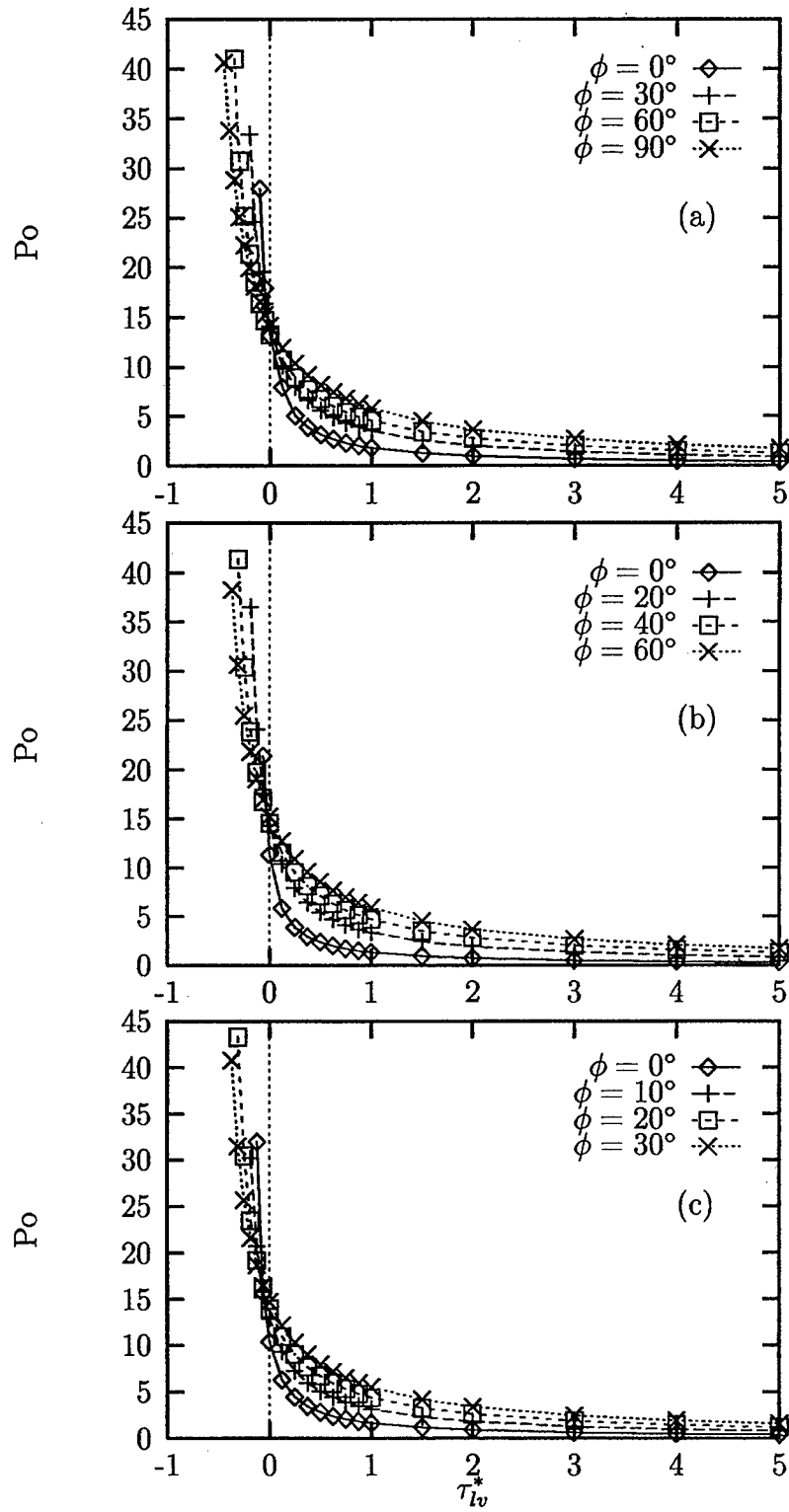


Figure 18: Po versus τ_{lv}^* for laminar flow in trapezoidal grooves ($\beta = 1.0$): (a) $\theta = 0^\circ$; (b) $\theta = 30^\circ$; (c) $\theta = 60^\circ$.

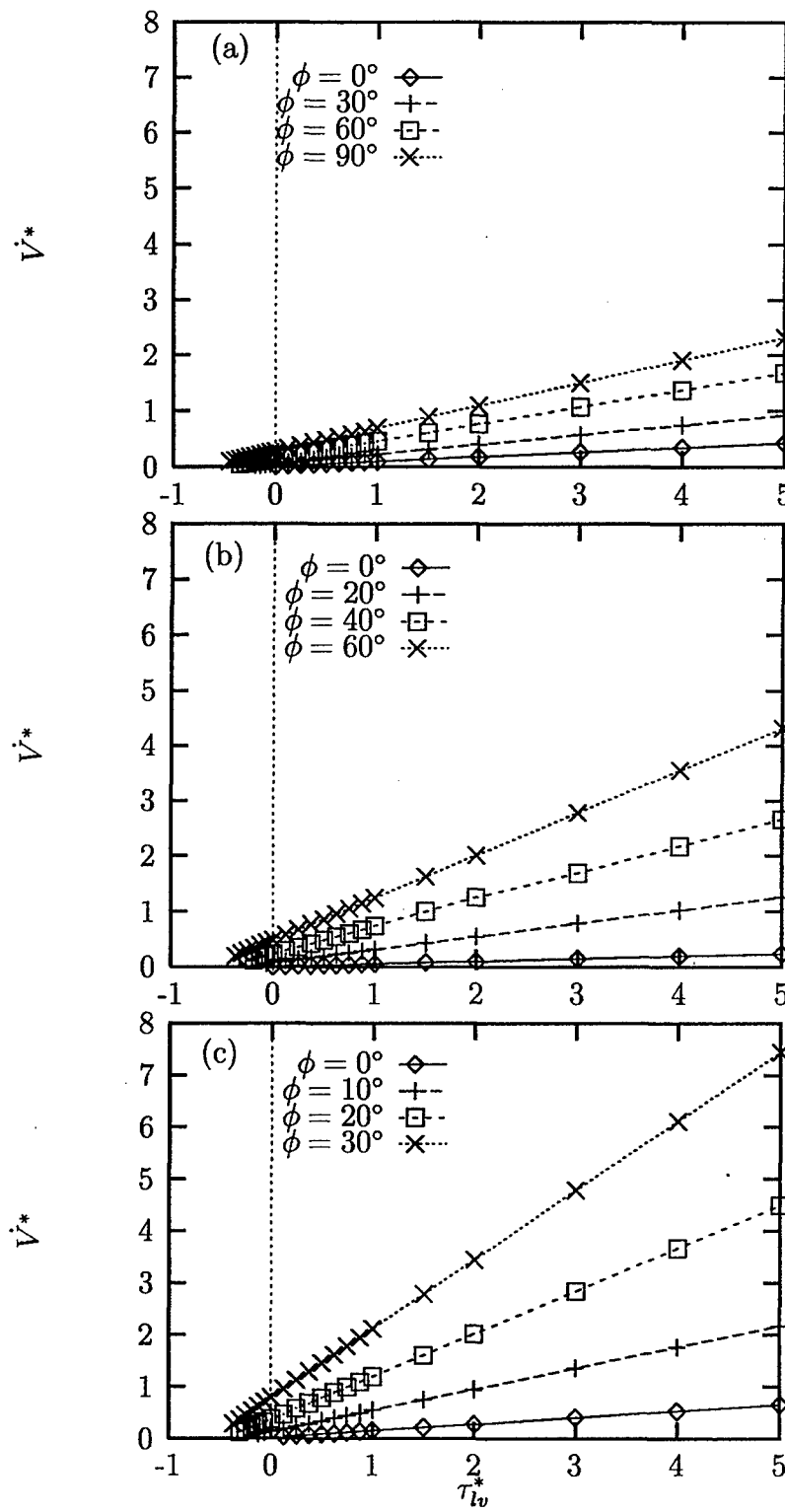


Figure 19: \dot{V}^* versus τ_{lv}^* for laminar flow in trapezoidal grooves ($\beta = 1.0$): (a) $\theta = 0^\circ$; (b) $\theta = 30^\circ$; (c) $\theta = 60^\circ$.

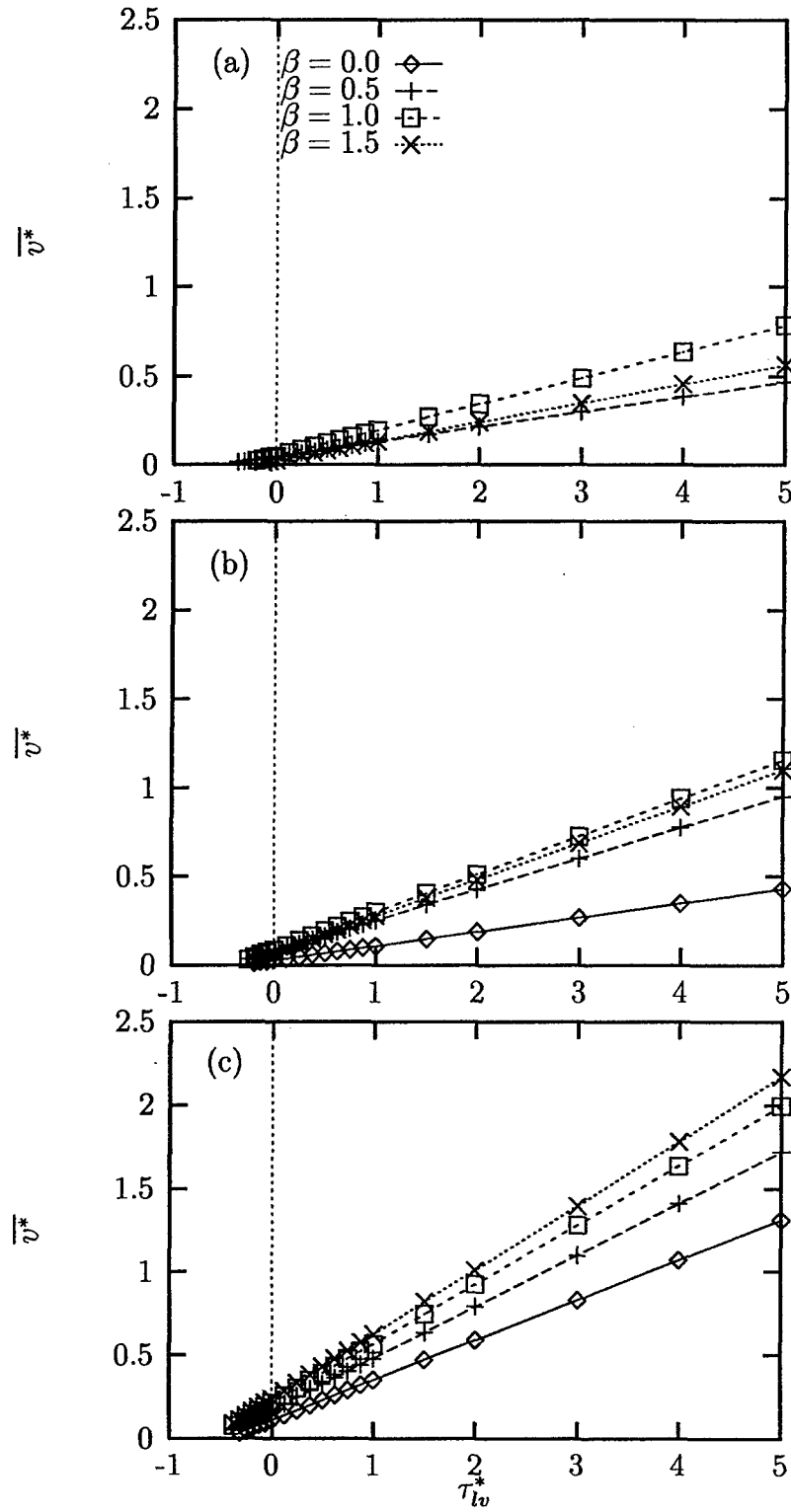


Figure 20: \overline{v}^* versus τ_{lv}^* for laminar flow in trapezoidal grooves ($\phi = 30^\circ$): (a) $\theta = 0^\circ$; (b) $\theta = 30^\circ$; (c) $\theta = 60^\circ$.

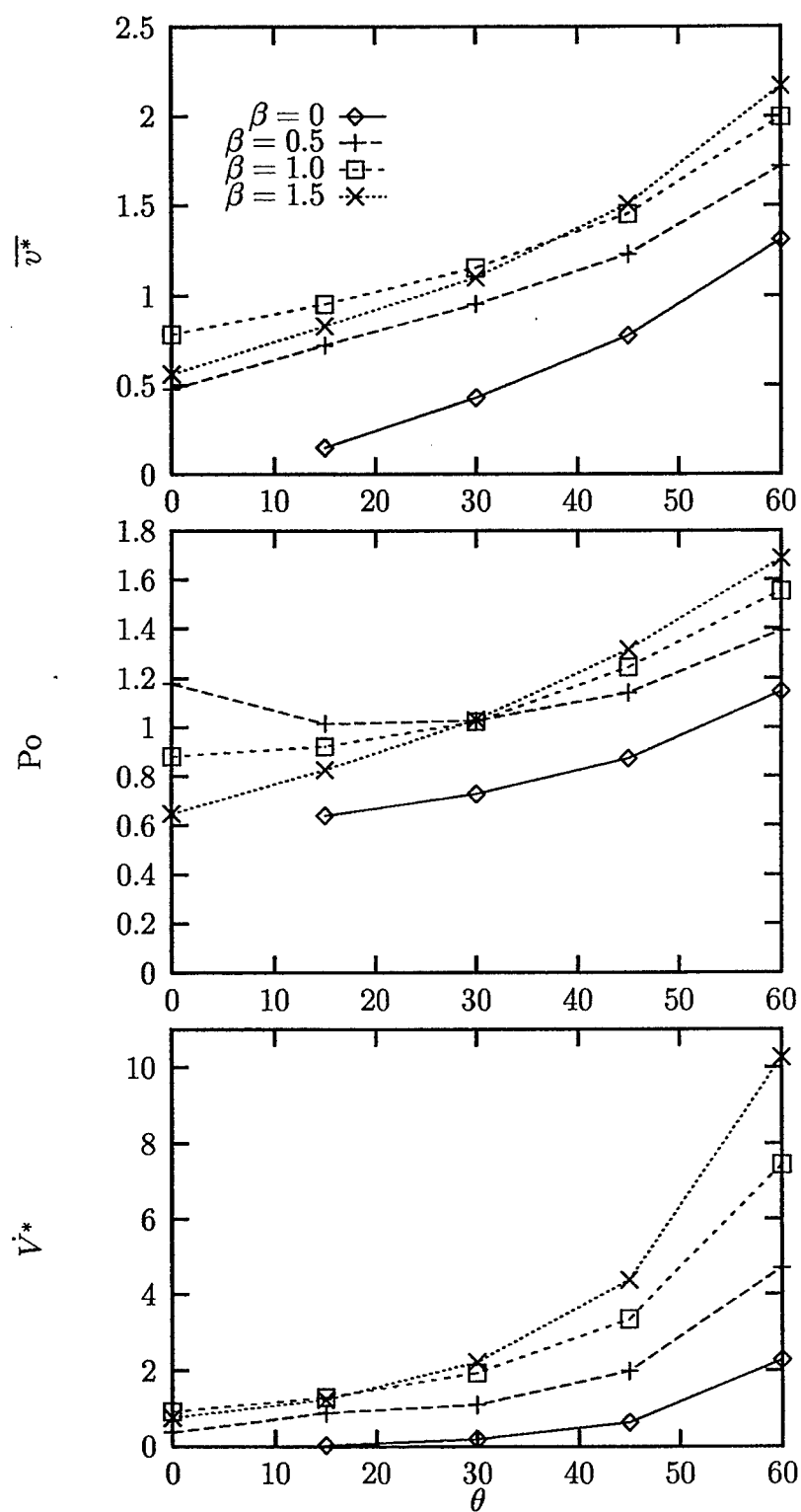


Figure 21: $\overline{v^*}$, Po and \dot{V}^* versus θ for laminar flow in trapezoidal grooves ($\phi = 30^\circ$, $\tau_{lv}^* = 5.0$).

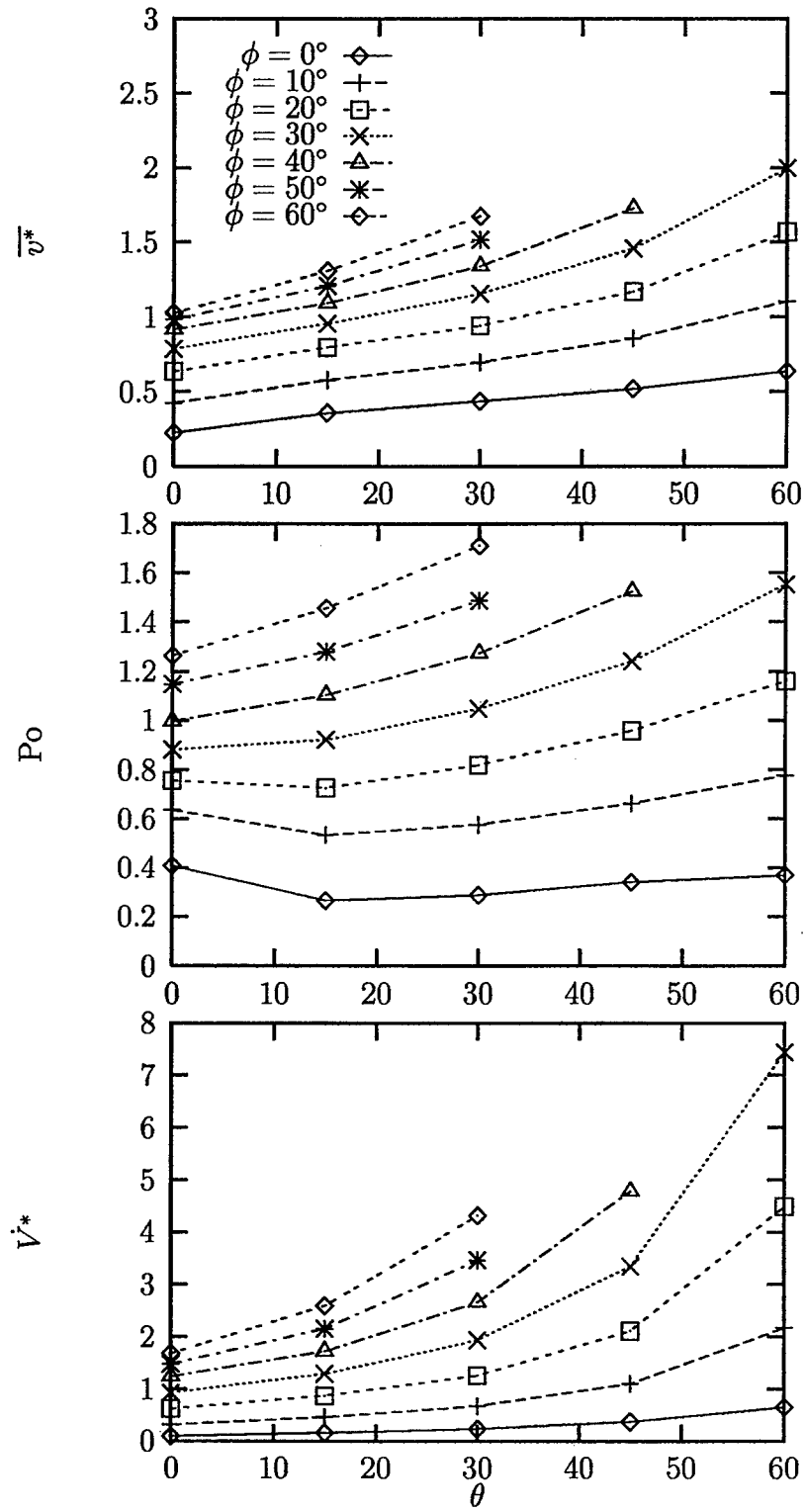


Figure 22: \bar{v}^* , Po and \dot{V}^* versus θ for laminar flow in trapezoidal grooves ($\beta = 1.0$, $\tau_{lv}^* = 5.0$).

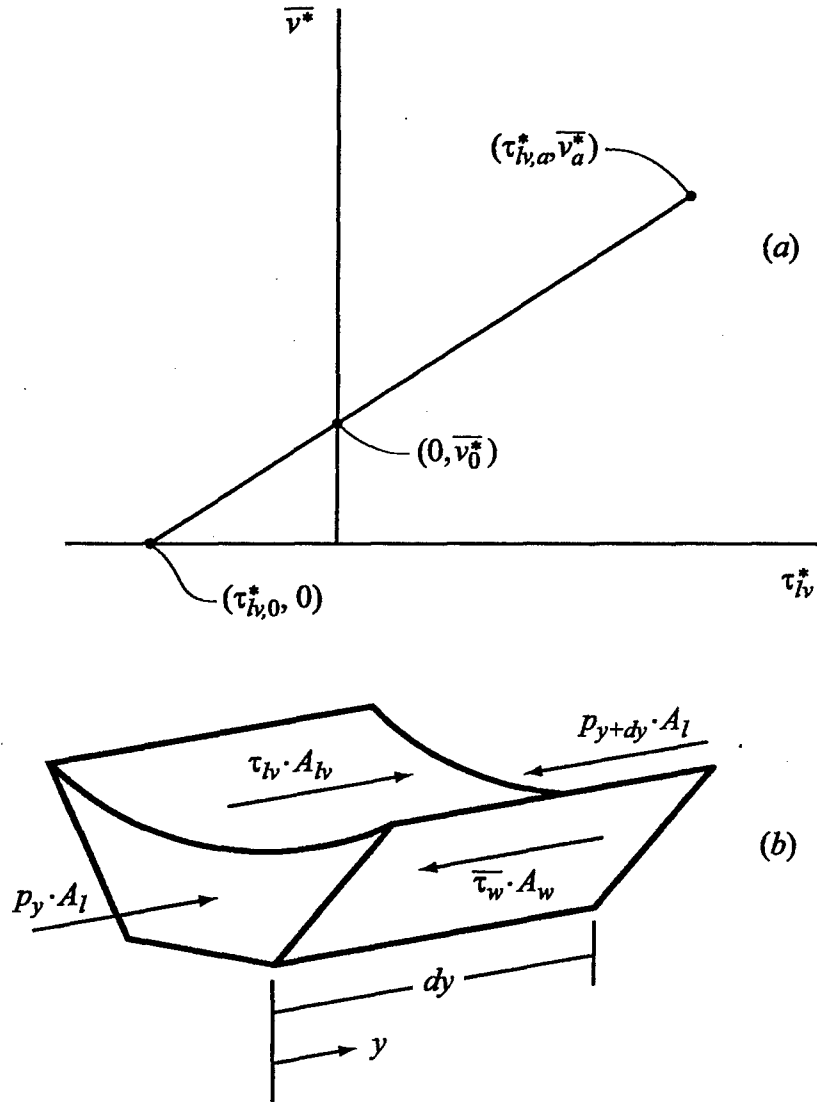


Figure 23: Semi-analytical and two-point numerical solutions for \bar{v}^* : (a) Definition of parameters; (b) Force balance on the liquid in a trapezoidal groove.

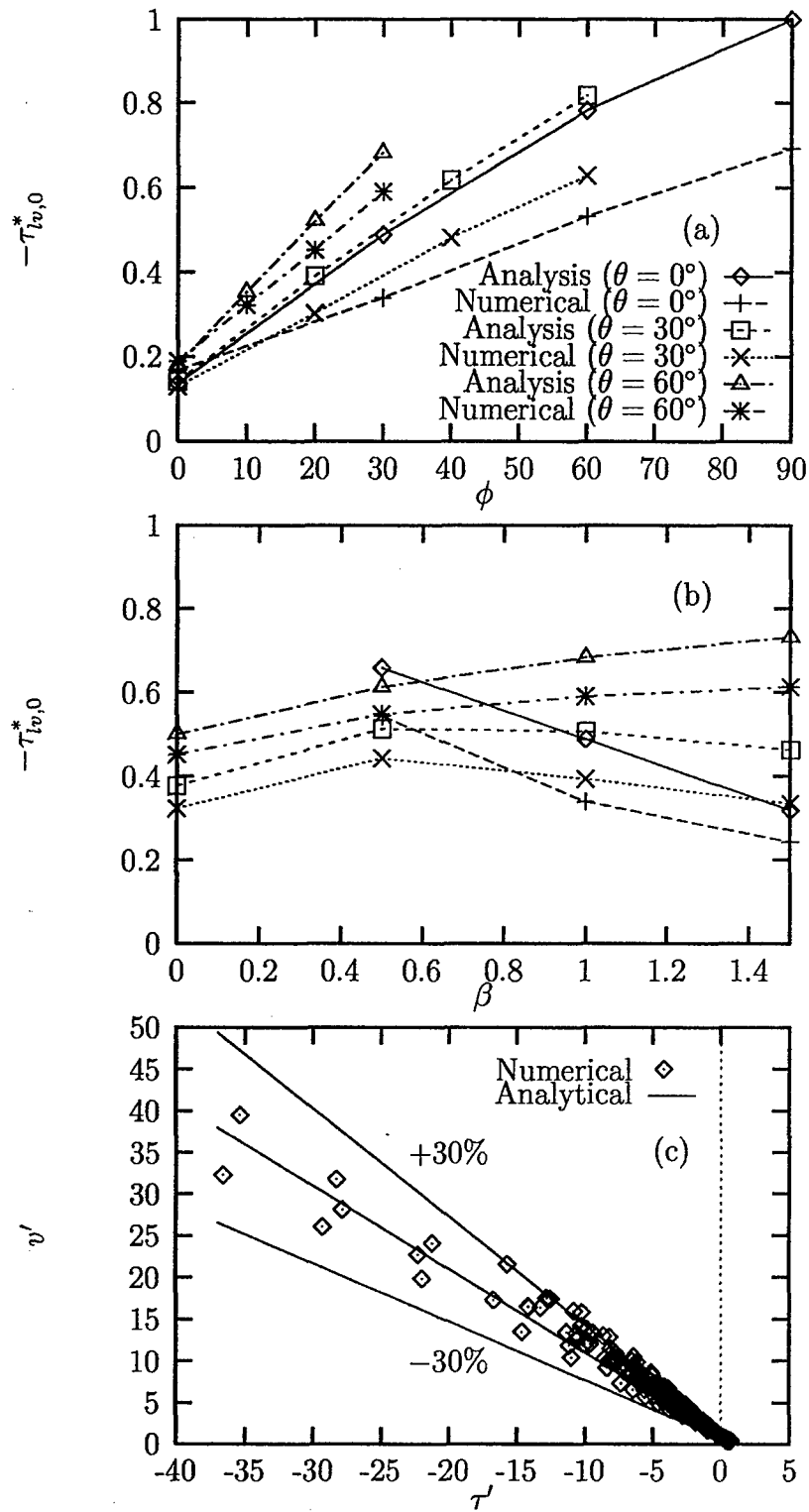


Figure 24: Numerical and semi-analytical solution comparison: (a) $-\tau_{lv,0}^*$ versus ϕ for $\beta = 1.0$ (from Fig. 17); (b) $-\tau_{lv,0}^*$ versus β for $\phi = 30^\circ$ (from Fig. 20); (c) Normalized mean velocity versus normalized shear stress at the liquid-vapor interface (from Figs. 17 and 20).

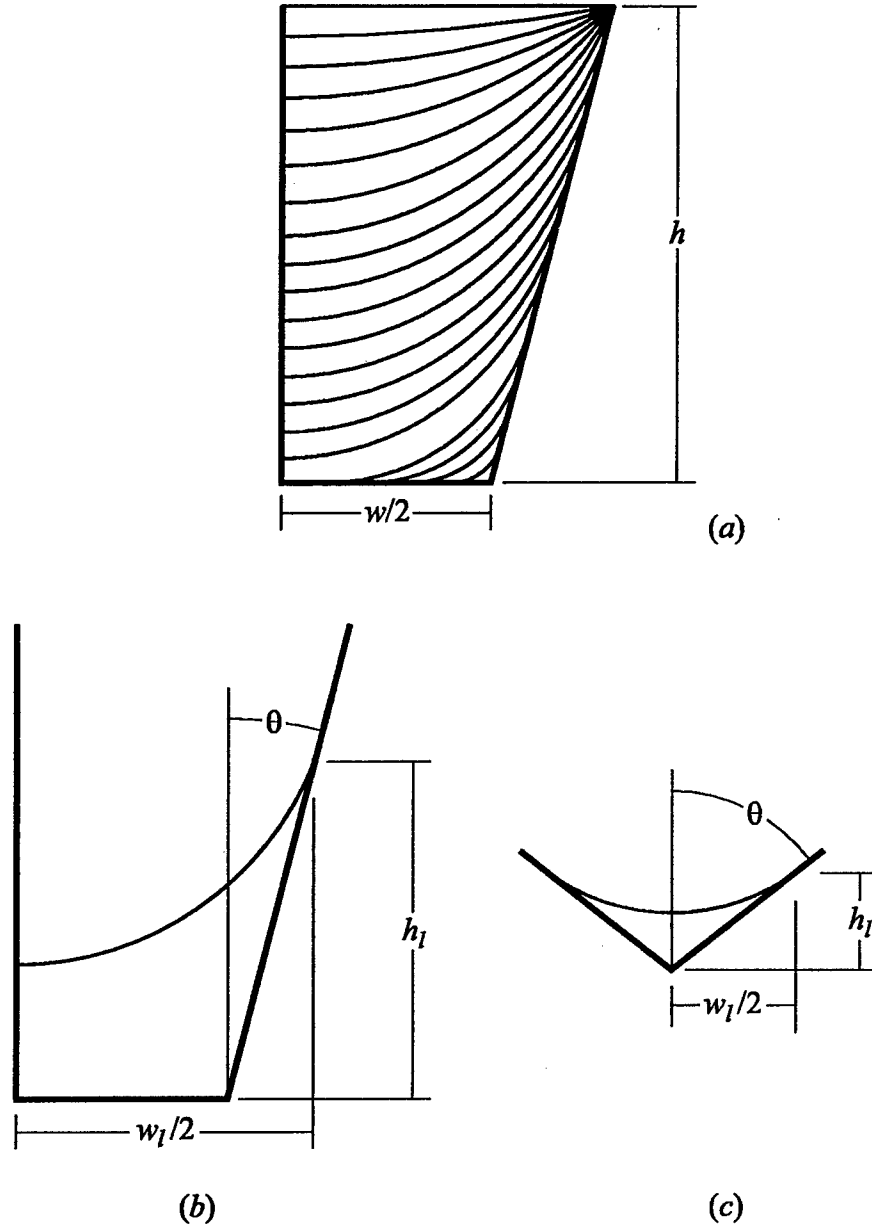


Figure 25: Effect of groove fill ratio on liquid flowing in a trapezoidal groove: (a) Parametric analysis (to scale, $h = 0.03831$ cm, $w = 0.03445$ cm, $\theta = 14.62^\circ$); (b) Definition of variables prior to bifurcation of the liquid; (c) Definition of variables after bifurcation of the liquid.

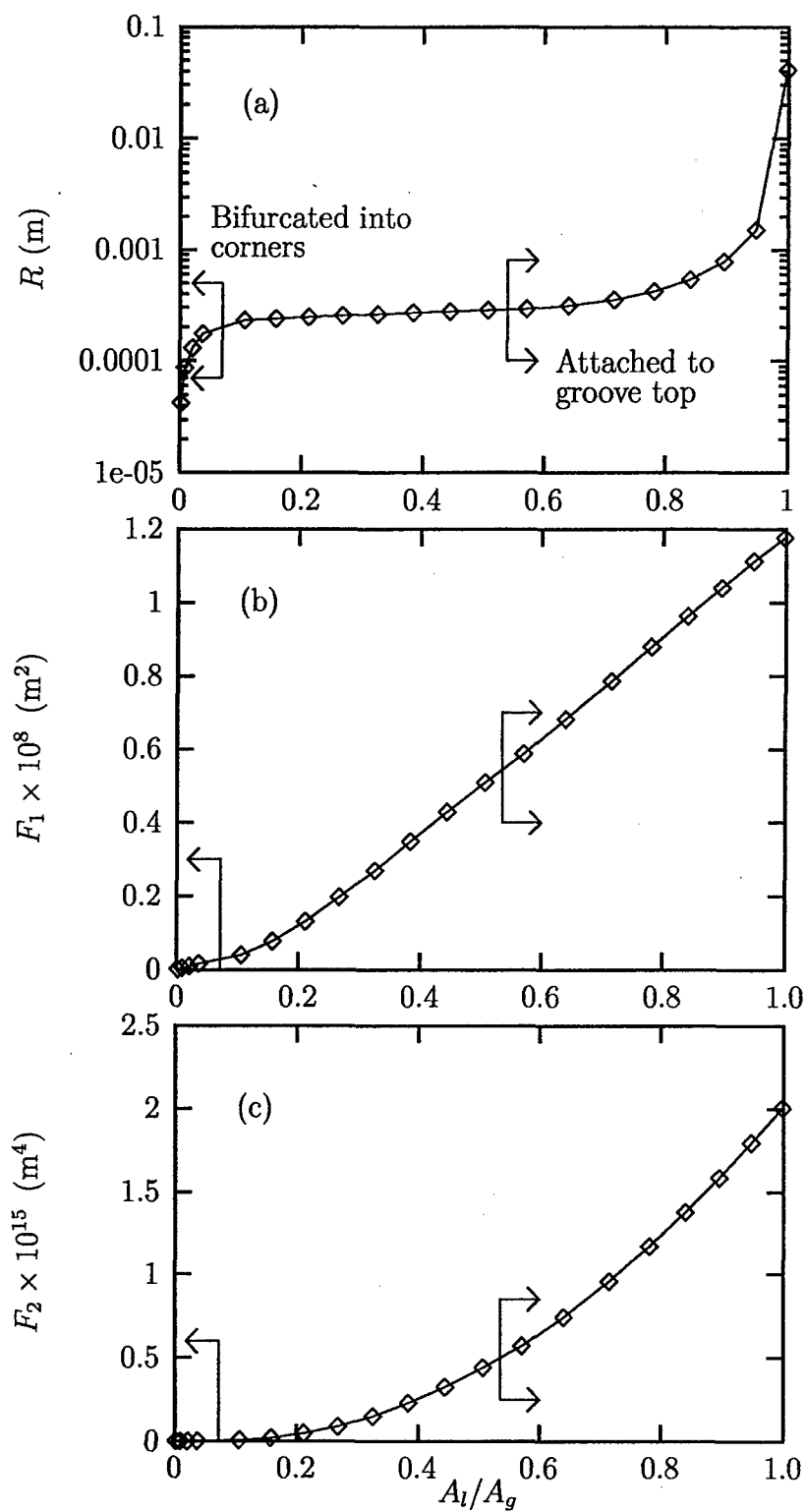


Figure 26: Effect of groove fill ratio: (a) Radius of curvature of the liquid-vapor interface; (b) Mean velocity parameter; (c) Volumetric flow rate parameter.

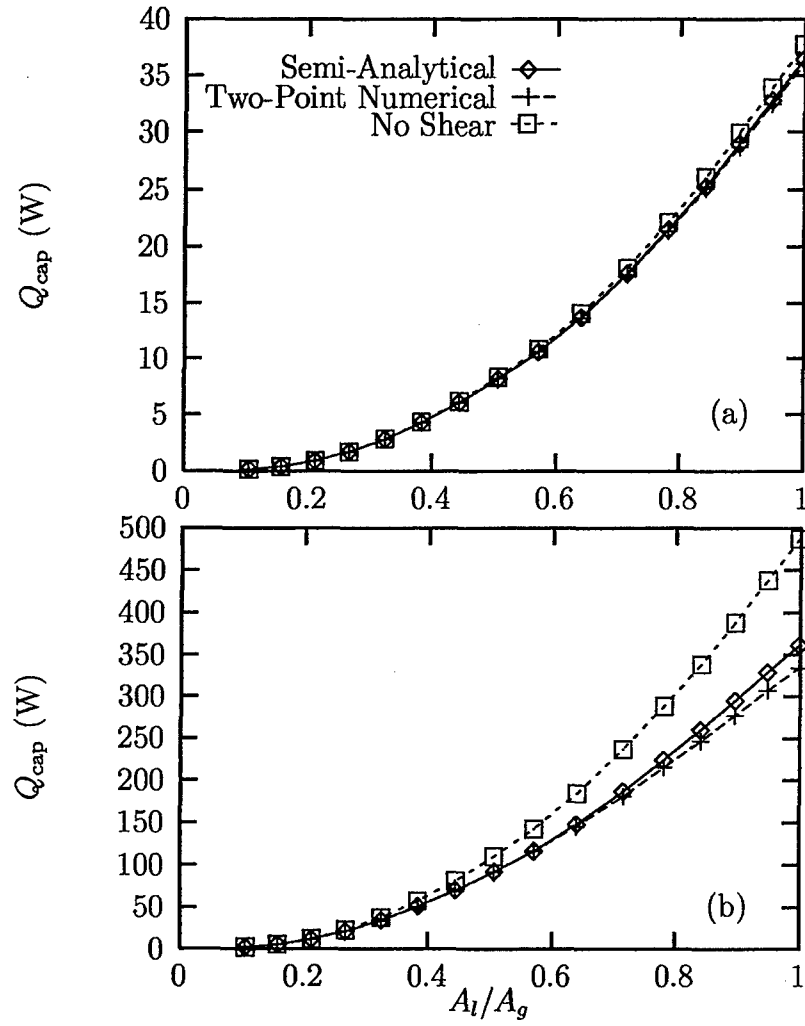


Figure 27: Maximum heat transport predicted by the closed-form solution versus groove fill ratio (Straight axial grooves, no body forces, $T_{\text{sat}} = 40^\circ\text{C}$): (a) Ethanol; (b) Water.

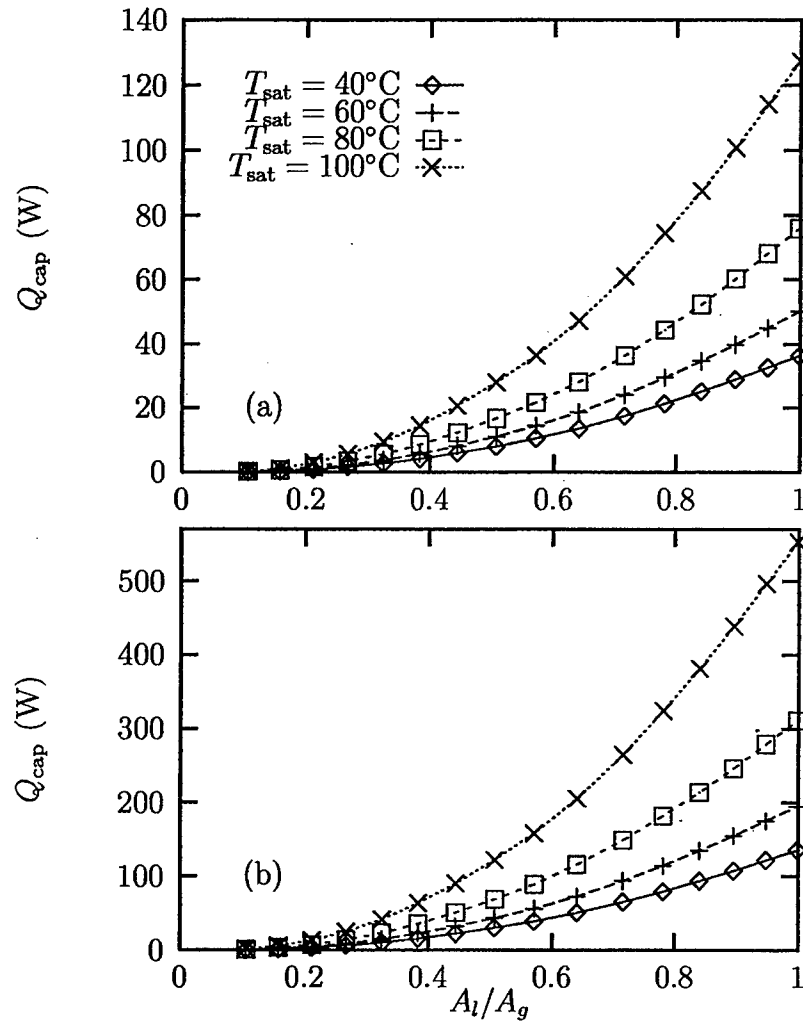


Figure 28: Maximum heat transport versus groove fill ratio for several working temperatures (Ethanol): (a) $|\vec{a}_r| = 0.0\text{-g}$; (b) $|\vec{a}_r| = 10.0\text{-g}$.

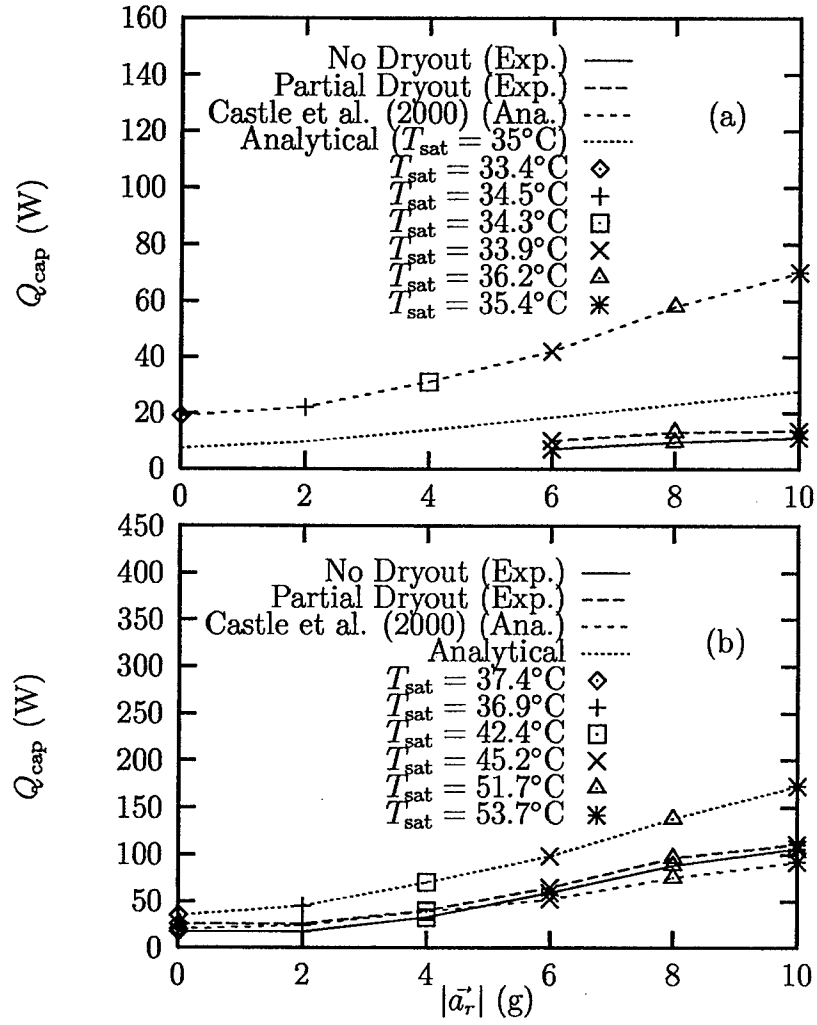


Figure 29: Maximum heat transport versus radial acceleration: (a) $A_l/A_g = 0.5$; (b) $A_l/A_g = 1.0$.

3 Fully-Developed Laminar Flow in Sinusoidal Grooves

3.1 Abstract

The flow of a constant property fluid through a sinusoidal groove has been analyzed. A numerical solution of the conservation of mass and momentum equations for fully developed flow is presented. The mean velocity, volumetric flow rate and Poiseuille number are presented as functions of the groove geometry, meniscus contact angle and shear stress at the liquid-vapor interface. In addition, a semi-analytical solution for the dimensionless mean velocity in terms of the dimensionless shear stress at the meniscus is shown to agree with the numerical data quite well.

3.2 Introduction

Isotropic materials such as quartz glass or borosilicate glass can be chemically etched to form micro-grooves for the enhancement of evaporative heat transfer in chip-level devices (Kirshberg et al., 1999). A typical etched profile in glass is shown in Fig. 30, where the profile is smooth instead of having sharp corners seen in the etching of crystalline materials such as silicon (Maluf, 2000). While many studies have been performed on sharp-cornered geometries [triangular grooves (Ayyaswamy et al., 1974; Ma et al., 1994; Romero and Yost, 1996; Lin and Faghri, 1997; Kolodziej et al., 1999), rectangular grooves (DiCola, 1968; Schneider and DeVos, 1980; Khrustalev and Faghri, 1999), and trapezoidal grooves (Hopkins et al., 1999; Thomas et al., 2000)], very little information is available in the open literature on the flow of liquid in rounded-corner geometries. Stroes and Catton (1997) compared the capillary performance of triangular and sinusoidal grooves by means of an experimental study. Two sets of grooves were machined into stainless steel test plates such that the cross-sectional areas of the grooves were equal. Strip heaters were placed under the plates to provide heat input. The test plates were placed at inclination angles of 4 and 6° and ethanol was added to the grooves until the liquid reached the lands of the grooves. The average wetted length of each set of grooves was recorded as the heat input was varied from 0 to 25 W. The study showed that the triangular grooves had a greater capillary pumping ability compared to the sinusoidal grooves with the same cross-sectional area, inclination angle, and heat input.

Stroes and Catton postulated that this was due to the axial rate of change of the radius of curvature of the meniscus. Sinusoidal grooves, however, could dissipate a given heat input with a smaller wetted area than triangular grooves due to the larger wetted perimeter found with sinusoidal grooves. The objective of the present study was to examine the fully-developed laminar flow of liquid in sinusoidal grooves. The effects of countercurrent and cocurrent vapor flow over the liquid-vapor interface were investigated by relating the liquid velocity gradient to the friction factor of the vapor. The variation of the shear stress on the liquid-vapor interface (Khrustalev and Faghri, 1999) was neglected, and the liquid-vapor interface was assumed to be circular ($Bo \ll 1$). The mean velocity, volumetric flow rate and Poiseuille number were determined as functions of the interfacial shear stress, the meniscus contact angle, the groove aspect ratio and the amount that the groove was filled.

3.3 Mathematical Model

A constant property liquid flows steadily in a sinusoidal groove as shown in Fig. 31. A meniscus, which is assumed to be circular, comprises the liquid-vapor interface. For fully developed laminar flow, the conservation of mass and momentum equations reduce to the classic Poisson equation in dimensionless form (White, 1991)

$$\frac{\partial^2 v^*}{\partial x^{*2}} + \frac{\partial^2 v^*}{\partial z^{*2}} = -1 \quad (44)$$

On the groove wall, the no-slip condition is in effect.

$$v^* = 0 : \quad 0 \leq x^* \leq w_l^*/2, \quad z^* = \frac{1}{2} \left\{ 1 + \cos \left[-\pi \left(\frac{x^*}{\beta} + 1 \right) \right] \right\} \quad (45)$$

At the line of symmetry, the velocity gradient is zero in the x^* direction

$$\frac{\partial v^*}{\partial x^*} = 0 : \quad x^* = 0, \quad 0 \leq z^* \leq h_l^* + R^* \sqrt{1 - \left(\frac{w_l^*}{2R^*} \right)^2} - R^* \quad (46)$$

The dimensionless radius of curvature is given by

$$R^* = \left(\frac{w_l^*}{2} \right) \left[1 + \frac{(1 + d^* \tan \phi)^2}{(d^* - \tan \phi)^2} \right]^{\frac{1}{2}} \quad (47)$$

where

$$d^* = \frac{\pi}{2\beta} \sin \left[-\pi \left(\frac{w_l^*}{2\beta} + 1 \right) \right] \quad (48)$$

The maximum value for the meniscus contact angle ϕ for a wetting fluid can be determined for a given geometry by allowing the radius of curvature to approach $R^* \rightarrow \infty$.

$$\phi_{\max} = \tan^{-1} \left\{ \frac{\pi}{2\beta} \sin \left[-\pi \left(\frac{w_l^*}{2\beta} + 1 \right) \right] \right\} \quad (49)$$

At the liquid-vapor interface, a uniform shear stress is imposed in the y direction.

$$\frac{\partial v^*}{\partial n^*} = \tau_{lv}^* : 0 \leq x^* \leq w_l^*/2, z^* = h_l^* + R^* \sqrt{1 - \left(\frac{w_l^*}{2R^*} \right)^2} - \sqrt{R^{*2} - x^{*2}} \quad (50)$$

The dimensional shear stress at the liquid-vapor interface can be cast in terms of the friction factor of the vapor.

$$\tau_{lv} = \begin{cases} \left[\frac{\rho_v (\overline{v_v})^2}{2} \right] f_v & \text{for cocurrent flow} \\ - \left[\frac{\rho_v (\overline{v_v})^2}{2} \right] f_v & \text{for countercurrent flow} \end{cases} \quad (51)$$

The Poiseuille number of the liquid in the groove is given by

$$\text{Po} = f\text{Re} = \frac{D_h^{*2}}{2v^*} \quad (52)$$

The dimensionless hydraulic diameter for the flow of liquid in a sinusoidal groove with a circular meniscus is $D_h^* = 4A_l^*/P^*$, where the dimensionless cross-sectional area of the liquid is given by

$$A_l^* = \frac{w_l^*}{2} (2h_l^* - 1) - R^* \left[R^* \cos^{-1} \sqrt{1 - \left(\frac{w_l^*}{2R^*} \right)^2} - \left(\frac{w_l^*}{2} \right) \sqrt{1 - \left(\frac{w_l^*}{2R^*} \right)^2} \right] + \left(\frac{\beta}{\pi} \right) \sin \left[-\pi \left(\frac{w_l^*}{2\beta} + 1 \right) \right] \quad \text{for } \phi < \phi_{\max} \quad (53)$$

$$A_l^* = \frac{w_l^*}{2} (2h_l^* - 1) + \left(\frac{\beta}{\pi} \right) \sin \left[-\pi \left(\frac{w_l^*}{2\beta} + 1 \right) \right] \quad \text{for } \phi = \phi_{\max} \quad (54)$$

The dimensionless wetted perimeter is given by the following integral equation.

$$P^* = 2 \int_0^{w_l^*/2} \sqrt{1 + \left(\frac{\pi}{2\beta} \right)^2 \sin^2 \left[-\pi \left(\frac{x^*}{\beta} + 1 \right) \right]} dx^* \quad (55)$$

The mean velocity is defined as

$$\overline{v^*} = \frac{2}{A_l^*} \int_0^{w_l^*/2} \int_0^{z^*} v^* dz^* dx^* \quad (56)$$

Table 6: Poiseuille number versus sinusoidal duct aspect ratio: Comparison of the present solution with that given by Shah (1975).

β	Poiseuille Number, Po	
	Shah (1975)	Present
1/4	14.553	14.479
1/3	14.022	13.931
1/2	13.023	12.935
1/ $\sqrt{3}$	12.630	12.543
2/3	12.234	12.148
1	11.207	11.115
2	10.123	10.061
4	9.743	9.6373

3.4 Numerical Model

The elliptic Poisson equation given by eqn. (44) with mixed boundary conditions [eqns. (45), (46) and (50)] was solved using Gauss-Seidel iteration with a central differencing scheme and successive over-relaxation (Anderson et al., 1984). The convergence criteria for the iterative solution was set to $\epsilon = 10^{-10}$ for each case. A grid independence check was made in which the number of grids in each direction was doubled. When the value for the Poiseuille number did not change by more than 1%, grid independence was considered to be reached. The convergence criteria was then reduced by an order of magnitude while maintaining the highest number of grids. If the Poiseuille number did not change by more than 1%, the solution was considered to be independent of both grid size and ϵ . Otherwise, a grid independence check was made at the smaller value of ϵ until a converged solution was reached. The integral equation for the wetted perimeter [eqn. (55)] was integrated numerically since no closed-form solution exists.

The numerical model was tested against an existing solution in the archival literature. Shah (1975) determined the friction factors for the laminar flow within ducts of various cross sections using a least-squares-matching technique. Table 6 shows the comparison of the Poiseuille number between the present solution and that given by Shah (1975) for laminar flow in a family of sinusoidal ducts. The agreement is excellent, with a maximum difference of 1.1%.

3.5 Results and Discussion

A numerical study has been completed in which the flow of liquid in a sinusoidal groove has been solved. Figure 32 presents contour plots of the dimensionless liquid velocity. The maximum liquid velocity increases with cocurrent shear, and decreases with countercurrent shear, as expected. For countercurrent vapor flow, a portion of the liquid flows in the $-y$ direction, which is opposite to the direction of the pressure gradient. This flow reversal shows the potential of the vapor shear to drive the mean velocity of the liquid to zero, or to completely reverse the flow, depending on the magnitude of the pressure gradient.

Figure 33 and Table 7 show the mean velocity, volumetric flow rate and Poiseuille number versus shear stress at the liquid-vapor interface for several values of the meniscus contact angle. The mean velocity increases with both τ_{lv}^* and ϕ , but is a relatively weak function of ϕ . For a given value of meniscus contact angle, the mean velocity is linear with τ_{lv}^* due to an overall force balance on the liquid. The volumetric flow rate also increases with τ_{lv}^* and ϕ , but is a much stronger function of ϕ due to the increase in the cross-sectional area of the liquid. The Poiseuille number decreases as τ_{lv}^* increases. For cocurrent vapor flow ($\tau_{lv}^* > 0$), Po decreases steadily with τ_{lv}^* . For countercurrent flow, Po increases dramatically with $-\tau_{lv}^*$ due to the mean velocity approaching zero. In general, Po increases with ϕ due to the increase in the hydraulic diameter of the liquid.

Figure 34 and Table 8 present the mean velocity, volumetric flow rate and Poiseuille number versus the groove fill ratio for several values of the groove aspect ratio. The mean velocity increases monotonically with area ratio and groove aspect ratio. The volumetric flow rate also increases with w_l^*/w^* and β , but drops off rapidly for $w_l^*/w^* < 0.5$ due to the decrease in flow area. The Poiseuille number is relatively constant for this case. For $\beta \geq 0.5$, Po decreases and then increases with area ratio. For $\beta = 0.25$, Po increases over the range of w_l^*/w^* examined.

3.6 Semi-Analytical Solution for \bar{v}^*

As seen in Fig. 33(a), the mean velocity is a linear function of the imposed shear stress at the liquid-vapor interface. Since a direct numerical simulation of the liquid flow field for

Table 7: Mean velocity, Poiseuille number and volumetric flow rate versus shear stress at the liquid-vapor interface for various values of meniscus contact angle ($\beta = 0.5$, $w_i^*/2 = 0.25$, $P^* = 1.15245$).

ϕ	τ_{lv}^*	\bar{v}^*	Po	V^*
0°	-0.1	0.18878×10^{-2}	27.088	0.17394×10^{-3}
0°	-0.075	0.26896×10^{-2}	19.013	0.24782×10^{-3}
0°	-0.05	0.35104×10^{-2}	14.567	0.32344×10^{-3}
0°	-0.025	0.43465×10^{-2}	11.765	0.40048×10^{-3}
0°	0.0	0.51353×10^{-2}	9.9581	0.47316×10^{-3}
0°	0.0625	0.71345×10^{-2}	7.1676	0.65738×10^{-3}
0°	0.125	0.91525×10^{-2}	5.5873	0.84330×10^{-3}
0°	0.25	0.13188×10^{-1}	3.8774	0.12152×10^{-2}
0°	0.375	0.17224×10^{-1}	2.9689	0.15870×10^{-2}
0°	0.5	0.21260×10^{-1}	2.4053	0.19589×10^{-2}
0°	0.75	0.29332×10^{-1}	1.7434	0.27026×10^{-2}
0°	1.0	0.37404×10^{-1}	1.3672	0.34464×10^{-2}
0°	2.0	0.69691×10^{-1}	0.73377	0.64214×10^{-2}
25°	-0.1	0.32506×10^{-2}	27.245	0.39414×10^{-3}
25°	-0.075	0.41572×10^{-2}	21.303	0.50408×10^{-3}
25°	-0.05	0.50437×10^{-2}	17.559	0.61158×10^{-3}
25°	-0.025	0.59348×10^{-2}	14.923	0.71962×10^{-3}
25°	0.0	0.68259×10^{-2}	12.974	0.82768×10^{-3}
25°	0.0625	0.90536×10^{-2}	9.7820	0.10978×10^{-2}
25°	0.125	0.11229×10^{-1}	7.8870	0.13616×10^{-2}
25°	0.25	0.15650×10^{-1}	5.6588	0.18977×10^{-2}
25°	0.375	0.20072×10^{-1}	4.4123	0.24338×10^{-2}
25°	0.5	0.24493×10^{-1}	3.6158	0.29700×10^{-2}
25°	0.75	0.33336×10^{-1}	2.6566	0.40422×10^{-2}
25°	1.0	0.42179×10^{-1}	2.0997	0.51144×10^{-2}
25°	2.0	0.77551×10^{-1}	1.1420	0.94034×10^{-2}
50°	-0.1	0.45097×10^{-2}	27.149	0.64296×10^{-3}
50°	-0.075	0.54643×10^{-2}	22.406	0.77904×10^{-3}
50°	-0.05	0.64189×10^{-2}	19.074	0.91514×10^{-3}
50°	-0.025	0.73345×10^{-2}	16.693	0.10457×10^{-2}
50°	0.0	0.82746×10^{-2}	14.796	0.11797×10^{-2}
50°	0.0625	0.10625×10^{-1}	11.523	0.15148×10^{-2}
50°	0.125	0.12975×10^{-1}	9.4363	0.18498×10^{-2}
50°	0.25	0.17586×10^{-1}	6.9621	0.25072×10^{-2}
50°	0.375	0.22255×10^{-1}	5.5014	0.31728×10^{-2}
50°	0.5	0.26922×10^{-1}	4.5477	0.38382×10^{-2}
50°	0.75	0.36256×10^{-1}	3.3769	0.51690×10^{-2}
50°	1.0	0.45590×10^{-1}	2.6855	0.64998×10^{-2}
50°	2.0	0.82926×10^{-1}	1.4764	0.11823×10^{-1}
72.34°	-0.1	0.54127×10^{-2}	28.188	0.86146×10^{-3}
72.34°	-0.075	0.64152×10^{-2}	23.783	0.10210×10^{-2}
72.34°	-0.05	0.74177×10^{-2}	20.569	0.11805×10^{-2}
72.34°	-0.025	0.84202×10^{-2}	18.120	0.13401×10^{-2}
72.34°	0.0	0.94227×10^{-2}	16.192	0.14996×10^{-2}
72.34°	0.0625	0.11929×10^{-1}	12.790	0.18985×10^{-2}
72.34°	0.125	0.14354×10^{-1}	10.629	0.22844×10^{-2}
72.34°	0.25	0.19309×10^{-1}	7.9016	0.30730×10^{-2}
72.34°	0.375	0.24264×10^{-1}	6.2880	0.38618×10^{-2}
72.34°	0.5	0.29219×10^{-1}	5.2217	0.46504×10^{-2}
72.34°	0.75	0.39129×10^{-1}	3.8992	0.62276×10^{-2}
72.34°	1.0	0.49039×10^{-1}	3.1112	0.78048×10^{-2}
72.34°	2.0	0.88244×10^{-1}	1.7290	0.14044×10^{-1}

Table 8: Wetted perimeter, mean velocity, Poiseuille number and volumetric flow rate versus groove fill ratio for various values of groove aspect ratio ($\tau_{lv}^* = 0.0$, $\phi = 0^\circ$).

β	w_l^*/w^*	P^*	\bar{v}^*	Po	\dot{V}^*
0.25	0.1	0.0731191	0.13005×10^{-4}	8.4006	0.35142×10^{-8}
0.25	0.2	0.223950	0.20221×10^{-3}	9.6365	0.70676×10^{-6}
0.25	0.3	0.450806	0.63058×10^{-3}	11.141	0.84242×10^{-5}
0.25	0.4	0.734032	0.12616×10^{-2}	12.059	0.40386×10^{-4}
0.25	0.5	1.04707	0.20592×10^{-2}	12.514	0.12238×10^{-3}
0.25	0.6	1.36011	0.29299×10^{-2}	12.849	0.27336×10^{-3}
0.25	0.7	1.64333	0.38585×10^{-2}	12.871	0.49958×10^{-3}
0.25	0.8	1.87019	0.47149×10^{-2}	12.940	0.77004×10^{-3}
0.25	0.9	2.02102	0.55519×10^{-2}	13.346	0.10799×10^{-2}
0.25	0.999	2.09364	0.74536×10^{-2}	15.203	0.18573×10^{-2}
0.5	0.1	0.114187	0.35380×10^{-5}	9.4469	0.82578×10^{-9}
0.5	0.2	0.288528	0.19851×10^{-3}	8.4052	0.82718×10^{-6}
0.5	0.3	0.531454	0.10922×10^{-2}	8.7511	0.20062×10^{-4}
0.5	0.4	0.827649	0.28055×10^{-2}	9.3706	0.13311×10^{-3}
0.5	0.5	1.15245	0.51353×10^{-2}	9.9581	0.47316×10^{-3}
0.5	0.6	1.47724	0.78593×10^{-2}	10.398	0.11735×10^{-2}
0.5	0.7	1.77344	0.10755×10^{-1}	10.780	0.22962×10^{-2}
0.5	0.8	2.01636	0.13817×10^{-1}	11.282	0.38892×10^{-2}
0.5	0.9	2.19070	0.17762×10^{-1}	12.443	0.64680×10^{-2}
0.5	0.999	2.30389	0.25467×10^{-1}	14.698	0.12692×10^{-1}
0.75	0.1	0.160025	0.11137×10^{-5}	10.092	0.21124×10^{-9}
0.75	0.2	0.367435	0.10959×10^{-3}	8.9207	0.44516×10^{-6}
0.75	0.3	0.634966	0.93568×10^{-3}	8.4299	0.18655×10^{-4}
0.75	0.4	0.951588	0.31271×10^{-2}	8.5312	0.17184×10^{-3}
0.75	0.5	1.29509	0.67001×10^{-2}	8.8579	0.74738×10^{-3}
0.75	0.6	1.63860	0.11328×10^{-1}	9.2444	0.21238×10^{-2}
0.75	0.7	1.95522	0.16731×10^{-1}	9.7209	0.46642×10^{-2}
0.75	0.8	2.22275	0.23143×10^{-1}	10.489	0.89608×10^{-2}
0.75	0.9	2.43016	0.32404×10^{-1}	11.885	0.17278×10^{-1}
0.75	0.999	2.58868	0.47659×10^{-1}	13.997	0.35626×10^{-1}
1.0	0.1	0.207697	0.45992×10^{-6}	10.367	0.73744×10^{-10}
1.0	0.2	0.453879	0.59860×10^{-4}	9.4362	0.22830×10^{-6}
1.0	0.3	0.752420	0.66244×10^{-3}	8.7481	0.13415×10^{-4}
1.0	0.4	1.09559	0.27276×10^{-2}	8.4926	0.16081×10^{-3}
1.0	0.5	1.46369	0.67927×10^{-2}	8.5590	0.84758×10^{-3}
1.0	0.6	1.83180	0.12785×10^{-1}	8.8427	0.27842×10^{-2}
1.0	0.7	2.17497	0.20665×10^{-1}	9.3068	0.69688×10^{-2}
1.0	0.8	2.47351	0.31143×10^{-1}	10.106	0.15279×10^{-1}
1.0	0.9	2.71969	0.46597×10^{-1}	11.485	0.32778×10^{-1}
1.0	0.999	2.92539	0.69923×10^{-1}	13.281	0.69692×10^{-1}

a number of values of the shear stress is computer resource intensive, it is appropriate to seek a semi-analytical expression for \overline{v}^* . Figure 35(a) shows the definition of the parameters involved, where the mean velocity when the shear stress is zero (\overline{v}_0^*) is given by the numerical solution. The value for the liquid-vapor shear for which the mean velocity is zero ($\tau_{lv,0}^*$) is given by the following force balance analysis. Figure 35(b) shows a differential element of the liquid in the groove. A force balance between the pressure drop and the shear forces at the liquid-vapor interface and at the wall results in the following relation.

$$p_y A_l - p_{y+dy} A_l + \tau_{lv} A_{lv} - \overline{\tau}_w A_w = 0 \quad (57)$$

The areas over which the shear stresses τ_{lv} and $\overline{\tau}_w$ act are $A_{lv} = P_{lv} dy$ and $A_w = P dy$, respectively. Using these areas and nondimensionalizing gives

$$A_l^* + \tau_{lv}^* P_{lv}^* - \overline{\tau}_w^* P^* = 0 \quad (58)$$

For Poiseuille flow in ducts of arbitrary cross section, and combined Couette-Poiseuille flow between flat plates, the shear stress at the wall is related to the mean velocity of the fluid by a constant (White, 1991). Therefore, in the present analysis, it is assumed that this also holds for the flow of liquid in a sinusoidal groove with an imposed shear stress at the liquid-vapor interface.

$$\overline{\tau}_w^* = C_1 \overline{v}^* \quad (59)$$

It should be noted that the constant C_1 is probably a function of the groove geometry and meniscus contact angle. However, since the objective of this analysis is to determine the liquid-vapor shear stress when the mean liquid velocity is zero, this functionality is unimportant. The perimeter of the liquid-vapor interface is

$$P_{lv}^* = 2R^* \sin^{-1} \left(\frac{w_l^*}{2R^*} \right) \quad (60)$$

Substituting these relations into the force balance equation results in the following expression for mean velocity.

$$\overline{v}^* = \frac{1}{C_1 P^*} \left[A_l^* + 2\tau_{lv}^* R^* \sin^{-1} \left(\frac{w_l^*}{2R^*} \right) \right] \quad (61)$$

The mean velocity is zero when

$$\tau_{lv,0}^* = - \frac{A_l^*}{2R^* \sin^{-1} \left(\frac{w_l^*}{2R^*} \right)} \quad (62)$$

Figure 36(a) shows the results of eqn. (62). The numerical results shown in Fig. 33(a) were extrapolated to determine the values for shear stress at the liquid-vapor interface when $\bar{v}^* = 0$. Both curves indicate that $\tau_{lv,0}^*$ increases with ϕ due to the increasing depth of liquid in the groove. The prediction given by eqn. (62) is quite good given the simplicity of the closed-form solution. The equation for the mean velocity as a function of the shear stress is given by

$$v' = \bar{v}^*/v_0^* = 1 - \tau' \quad (63)$$

where $\tau' = \tau_{lv}^*/\tau_{lv,0}^*$. The semi-analytical solution for the normalized mean velocity is shown in Fig. 36(b) with the corresponding numerical data presented in Fig. 33. Equation (63) predicts 94% of the data to within $\pm 20\%$ over the range of meniscus contact angle examined.

3.7 Conclusions

Based on the results of the numerical model of the flow of liquid in a sinusoidal groove, the following conclusions have been made: For a given meniscus contact angle, the mean velocity was linear with imposed shear stress at the liquid-vapor interface. The volumetric flow rate in the groove was negligible for groove fill ratios of less than $w_l^*/w^* < 0.5$. The Poiseuille number was a strong function of the countercurrent shear stress. A semi-analytical expression was provided to approximate the mean velocity as a function of the shear stress at the liquid-vapor interface.

3.8 Nomenclature

A_l	cross-sectional area of the liquid, m^2
A_l^*	A_l/h^2
A_{lv}	area of the liquid-vapor interface, m^2
A_w	area of the groove wall, m^2
Bo	Bond number, $\rho g z_1^2/\sigma$
d^*	parameter defined in eqn. (48)
D_h	hydraulic diameter, $4A_l/P$, m
D_h^*	D_h/h
f	friction coefficient, $2\bar{\tau}/\rho\bar{v}^2$

g	acceleration due to gravity, m/s ²
h	groove height, m
h_l	height of liquid in the groove at the wall, m
h_l^*	h_l/h
n	coordinate normal to the liquid-vapor interface
n^*	n/h
p	pressure, N/m ²
P	wetted perimeter, m
P^*	P/h
P_{lv}	perimeter of the liquid-vapor interface, m
P_{lv}^*	P_{lv}/h
Po	Poiseuille number, fRe
R	radius of curvature of the meniscus, m
R^*	R/h
Re	Reynolds number, $\rho \bar{v} D_h / \mu$
v	y -direction velocity, m/s
\bar{v}	average y -direction velocity, m/s
v^*	$\mu v / h^2 (-dp/dy)$
\bar{v}^*	dimensionless average y -direction velocity
\bar{v}_0^*	dimensionless average y -direction velocity when $\tau_{lv}^* = 0$
v'	\bar{v}^* / \bar{v}_0^*
\dot{V}	volumetric flow rate, $\bar{v} A_l$, m ³ /s
\dot{V}^*	$\mu \dot{V} / [h^4 (-dp/dy)]$
w	period of the sinusoidal groove, m
w^*	w/h
w_l	width of the liquid in the groove, m
w_l^*	w_l/h
x, y, z	coordinate directions
x^*	x/h
z_1	distance from the liquid-vapor interface to the groove bottom, m

z^*	z/h
β	groove aspect ratio, $w/2h$
ϵ	convergence criteria
μ	absolute viscosity, Pa-s
ρ	density, kg/m ³
σ	surface tension, N/m
τ_{lv}	shear stress at the liquid-vapor interface, N/m ²
τ_{lv}^*	$\tau_{lv}/h(-dp/dy)$
$\tau_{lv,0}^*$	dimensionless shear stress at the liquid-vapor interface when $\bar{v}^* = 0$
$\bar{\tau}$	average shear stress, $A_l(-dp/dy)/P$, N/m ²
$\bar{\tau}_w$	average shear stress at the groove wall, N/m ²
$\bar{\tau}_w^*$	$\bar{\tau}_w/h(-dp/dy)$
τ'	$\tau_{lv}^*/\tau_{lv,0}^*$
ϕ	meniscus contact angle, rad
ϕ_{\max}	maximum meniscus contact angle, rad

3.9 References

- Anderson, D., Tannehill, J., and Pletcher, R., 1984, *Computational Fluid Mechanics and Heat Transfer*, Hemisphere, New York.
- Ayyaswamy, P., Catton, I., and Edwards, D., 1974, "Capillary flow in triangular grooves," *ASME J. Appl. Mech.*, Vol. 41, pp. 332-336.
- DiCola, G., 1968, "Soluzione analitica, amezzo della trasformata di Fourier, di un problema di fusso in un canale rettangolare," Euratom C.C.R. Ispra (Italy), C.E.T.I.S.
- Hopkins, R., Faghri, A., and Khrustalev, D., 1999, "Flat miniature heat pipes with micro capillary grooves," *ASME J. Heat Transfer*, Vol. 121, pp. 102-109.
- Khrustalev, D., and Faghri, A., 1999, "Coupled liquid and vapor flow in miniature passages with micro grooves," *ASME J. Heat Transfer*, Vol. 121, pp. 729-733.
- Kirshberg, J., Liepmann, D., and Yerkes, K., 1999, "Micro-cooler for chip-level temperature control," *Proc. SAE Aerospace Power Systems Conf.*, Paper No. 1999-01-1407.

Kolodziej, J., Musielak, G., Kaczmarek, M., and Strek, T., 1999, "Determination of free surface and gravitational flow of liquid in triangular groove," *Computational Mechanics*, Vol. 24, pp. 110-117.

Lin, L., and Faghri, A., 1997, "Steady-state performance of a rotating miniature heat pipe," *AIAA J. Thermophysics Heat Transfer*, Vol. 11, pp. 513-518.

Ma, H., Peterson, G., and Lu, X., 1994, "The influence of vapor-liquid interactions on the liquid pressure drop in triangular microgrooves," *Int. J. Heat Mass Transfer*, Vol. 37, pp. 2211-2219.

Maluf, N., 2000, *An Introduction to Microelectromechanical Systems Engineering*, Artech House, Boston.

Romero, L., and Yost, F., 1996, "Flow in an open channel," *J. Fluid Mech.*, Vol. 322, pp. 109-129.

Schneider, G., and DeVos, R., 1980, "Non-dimensional analysis for the heat transport capability of axially grooved heat pipes including liquid/vapor interaction," AIAA Paper No. 80-0214.

Shah, R., 1975, "Laminar flow friction and forced convection heat transfer in ducts of arbitrary geometry," *Int. J. Heat Mass Transfer*, Vol. 18, pp. 849-862.

Stroes, G., and Catton, I., 1997, "An experimental investigation of the capillary performance of triangular versus sinusoidal channels," *ASME J. Heat Transfer*, Vol. 119, pp. 851-853.

Thomas, S., Lykins, R., and Yerkes, K., 2000, "Friction factors for fully-developed laminar flow in trapezoidal grooves with shear stress at the liquid-vapor interface," in preparation.

White, F., 1991, *Viscous Fluid Flow*, 2nd edn., McGraw-Hill, New York.

3.10 Appendix

3.10.1 Equation of the circular meniscus

To determine the equation of the circular meniscus, a relationship must be made based on the slope of the tangent line at the sinusoidal groove wall, which is given by

$$\tan \psi = \left. \frac{dz^*}{dx^*} \right|_{\text{sine}} \quad (64)$$

The equation of the sinusoid for the groove wall is given by

$$z^* = \frac{1}{2} \left\{ 1 + \cos \left[-\pi \left(\frac{x^*}{\beta} + 1 \right) \right] \right\} \quad (65)$$

Differentiating eqn. (65) with respect to x^* gives

$$\frac{dz^*}{dx^*} = \frac{\pi}{2\beta} \sin \left[-\pi \left(\frac{x^*}{\beta} + 1 \right) \right] \quad (66)$$

Therefore, substituting eqn. (66) into eqn. (64) and evaluating $x^* = w_l^*/2$ results in the equation of the slope of the tangent line at the wall of the sinusoidal groove.

$$\tan \psi = \left. \frac{dz^*}{dx^*} \right|_{\text{sinusoid}} = \frac{\pi}{2\beta} \sin \left[-\pi \left(\frac{w_l^*}{2\beta} + 1 \right) \right] \quad (67)$$

The slope of the tangent line on the circular meniscus is given by

$$\tan \theta = \left. \frac{dz^*}{dx^*} \right|_{\text{circle}} \quad (68)$$

From Fig. 37, the angle θ can be found as a function of angles α , ϕ , and ψ

$$\alpha = \pi - \psi \quad (69)$$

$$\theta + \phi + \alpha = \pi \quad (70)$$

$$\theta = \psi - \phi \quad (71)$$

Taking the tangent of both sides of eqn. (71) and using the trigonometric addition formula for tangent gives

$$\tan \theta = \tan(\psi - \phi) \quad (72)$$

$$\tan(\alpha \pm \beta) = \frac{\tan \alpha \pm \tan \beta}{1 \mp \tan \alpha \tan \beta} \quad (73)$$

$$\tan \theta = \frac{\tan \psi - \tan \phi}{1 + \tan \psi \tan \phi} \quad (74)$$

The general equation for a circle with the z^* axis as a line of symmetry is

$$x^{*2} + (z^* - z_o^*)^2 = R^{*2} \quad (75)$$

Taking the derivative of eqn. (75) with respect to x^* gives

$$2x^* + 2(z^* - z_o^*) \frac{dz^*}{dx^*} = 0 \quad (76)$$

Rearranging eqn. (76) to solve for dz^*/dx^* gives

$$\frac{dz^*}{dx^*} = -\frac{x^*}{(z^* - z_o^*)} \quad (77)$$

By substituting $x^* = w_l^*/2$ and $z^* = h_l^*$ into eqn. (77) and then substituting the result into eqn. (68) gives the slope of the tangent line on the circular meniscus

$$\left. \frac{dz^*}{dx^*} \right|_{\text{circle}} = -\frac{w_l^*/2}{(h_l^* - z_o^*)} = \tan \theta \quad (78)$$

Combining eqns. (74) and (78) gives

$$-\frac{w_l^*/2}{(h_l^* - z_o^*)} = \frac{\tan \psi - \tan \phi}{1 + \tan \psi \tan \phi} \quad (79)$$

Rearranging eqn. (79) to solve for z_o^* gives

$$z_o^* = h_l^* + \frac{\left(\frac{w_l^*}{2}\right)(1 + \tan \psi \tan \phi)}{\tan \psi - \tan \phi} \quad (80)$$

where z_o^* is the height of the center of the circle on the z^* axis. By letting d be the distance between the center of the circular liquid-vapor interface and the height of the liquid, it can be shown that

$$z_o^* = h_l^* + d \quad (81)$$

$$d = \sqrt{R^{*2} - \left(\frac{c}{2}\right)^2} \quad (82)$$

$$\frac{c}{2} = \frac{w_l^*}{2} \quad (83)$$

$$z_o^* = h_l^* + \sqrt{R^{*2} - \left(\frac{w_l^*}{2}\right)^2} \quad (84)$$

Combining eqns. (80) and (84) gives

$$\sqrt{R^{*2} - \left(\frac{w_l^*}{2}\right)^2} = \frac{\left(\frac{w_l^*}{2}\right)(1 + \tan \psi \tan \phi)}{\tan \psi - \tan \phi} \quad (85)$$

$$R^{*2} - \left(\frac{w_l^*}{2}\right)^2 = \left[\frac{\left(\frac{w_l^*}{2}\right)(1 + \tan \psi \tan \phi)}{\tan \psi - \tan \phi} \right]^2 \quad (86)$$

$$\frac{\left(\frac{w_l^*}{2}\right)}{\sqrt{R^{*2} - \left(\frac{w_l^*}{2}\right)^2}} = \frac{d^* - \tan \phi}{1 + d^* \tan \phi} \quad (87)$$

where

$$d^* = \tan \psi = \frac{\pi}{2\beta} \sin \left[-\pi \left(\frac{w_l^*}{2\beta} + 1 \right) \right] \quad (88)$$

$$\sqrt{R^{*2} - \left(\frac{w_l^*}{2}\right)^2} = \frac{\left(\frac{w_l^*}{2}\right) (1 + d^* \tan \phi)}{d^* - \tan \phi} \quad (89)$$

$$R^{*2} - \left(\frac{w_l^*}{2}\right)^2 = \frac{\left(\frac{w_l^*}{2}\right)^2 (1 + d^* \tan \phi)^2}{(d^* - \tan \phi)^2} \quad (90)$$

$$R^{*2} = \left(\frac{w_l^*}{2}\right)^2 \left[1 + \frac{(1 + d^* \tan \phi)^2}{(d^* - \tan \phi)^2} \right] \quad (91)$$

The equation of the radius of curvature of the meniscus in terms of meniscus contact angle is

$$R^* = \left(\frac{w_l^*}{2}\right) \left[1 + \frac{(1 + d^* \tan \phi)^2}{(d^* - \tan \phi)^2} \right]^{\frac{1}{2}} \quad (92)$$

3.10.2 Determination of the maximum meniscus contact angle

The maximum meniscus contact angle can be found when $R^* \rightarrow \infty$ in eqn. (92). It can be seen that $R^* \rightarrow \infty$ as $(d^* - \tan \phi) \rightarrow 0$. Therefore

$$d^* - \tan \phi_{\max} = 0 \quad (93)$$

Substituting eqn. (93) into eqn. (88) for d^* results in

$$\frac{\pi}{2\beta} \sin \left[-\pi \left(\frac{w_l^*}{2\beta} + 1 \right) \right] - \tan \phi_{\max} = 0 \quad (94)$$

Solving for ϕ_{\max} gives the equation for the maximum meniscus contact angle.

$$\phi_{\max} = \tan^{-1} \left\{ \frac{\pi}{2\beta} \sin \left[-\pi \left(\frac{w_l^*}{2\beta} + 1 \right) \right] \right\} \quad (95)$$

3.10.3 Determination of the hydraulic diameter

The hydraulic diameter of the flow field must be determined so that the Poiseuille number can be calculated. To find $D_h^* = 4A_l^*/P^*$, it can be shown from Fig. 38 that

$$A_1 + A_2 + A_3 = \frac{1}{2}w_l^*h_l^* \quad (96)$$

$$A_2 = \frac{A_l^*}{2} = \frac{1}{2}w_l^*h_l^* - A_1 - A_3 \quad (97)$$

The area A_3 can be found by integrating the equation for the sinusoidal groove wall, eqn. (65) over $0 \leq x^* \leq w_l^*/2$.

$$A_3 = \int_0^{w_l^*/2} \frac{1}{2} \left\{ 1 + \cos \left[-\pi \left(\frac{x^*}{\beta} + 1 \right) \right] \right\} dx^* \quad (98)$$

$$A_3 = \frac{w_l^*}{4} - \frac{\beta}{2\pi} \sin \left[-\pi \left(\frac{w_l^*}{2\beta} + 1 \right) \right] \quad (99)$$

From Fig. 38, A_1 is the area above the meniscus. It can be shown that A_1 is one-half of the area of the segment

$$A_1 = \frac{R^{*2}}{2} \cos^{-1} \left(\frac{d}{R^*} \right) - d\sqrt{R^{*2} - d^2} \quad (100)$$

where

$$d = \sqrt{R^{*2} - \left(\frac{w_l^*}{2} \right)^2} \quad (101)$$

Thus, the area A_1 is

$$A_1 = \frac{R^*}{2} \left[R^* \cos^{-1} \sqrt{1 - \left(\frac{w_l^*}{2R^*} \right)^2} - \left(\frac{w_l^*}{2} \right) \sqrt{1 - \left(\frac{w_l^*}{2R^*} \right)^2} \right] \quad (102)$$

Substituting eqns. (99) and (102) into eqn. (97) gives the cross-sectional area of the flow field

$$A_l^* = \frac{w_l^*}{2} (2h_l^* - 1) - R^* \left[R^* \cos^{-1} \sqrt{1 - \left(\frac{w_l^*}{2R^*} \right)^2} - \left(\frac{w_l^*}{2} \right) \sqrt{1 - \left(\frac{w_l^*}{2R^*} \right)^2} \right] + \frac{\beta}{\pi} \sin \left[-\pi \left(\frac{w_l^*}{2\beta} + 1 \right) \right] \quad \text{for } \phi < \phi_{\max} \quad (103)$$

When the meniscus contact angle approaches the maximum value $\phi \rightarrow \phi_{\max}$, the area $A_1 \rightarrow 0$. Therefore, the cross-sectional area of the flow field for this case is

$$A_l^* = w_l^*h_l^* - 2A_3 \quad (104)$$

$$A_i^* = w_i^* h_i^* - \frac{w_i^*}{2} + \frac{\beta}{\pi} \sin \left[-\pi \left(\frac{w_i^*}{2\beta} + 1 \right) \right] \quad (105)$$

$$A_i^* = \frac{w_i^*}{2} (2h_i^* - 1) + \frac{\beta}{\pi} \sin \left[-\pi \left(\frac{w_i^*}{2\beta} + 1 \right) \right] \quad \text{for } \phi = \phi_{\max} \quad (106)$$

In order to determine the wetted perimeter, the following formula will be used to find the arc length of the groove wall

$$P^* = \int_{x_1}^{x_2} \sqrt{1 + (y')^2} dx \quad \text{for } y = f(x)$$

$$P^* = 2 \int_0^{w_i^*/2} \sqrt{1 + \left(\left. \frac{dz^*}{dx^*} \right|_{\text{sine}} \right)^2} dx^* \quad (107)$$

where

$$\left. \frac{dz^*}{dx^*} \right|_{\text{sine}} = \frac{\pi}{2\beta} \sin \left[-\pi \left(\frac{x^*}{\beta} + 1 \right) \right] \quad (108)$$

Thus, the arc length can be found by substituting eqn. (108) into eqn. (107)

$$P^* = 2 \int_0^{w_i^*/2} \sqrt{1 + \left(\frac{\pi}{2\beta} \right)^2 \sin^2 \left[-\pi \left(\frac{x^*}{\beta} + 1 \right) \right]} dx^* \quad (109)$$

The equation for the wetted perimeter has no closed-form solution, and consequently the equation for the hydraulic diameter has no closed-form solution. The reason is that the integral in eqn. (109) is elliptic, and must be solved numerically.

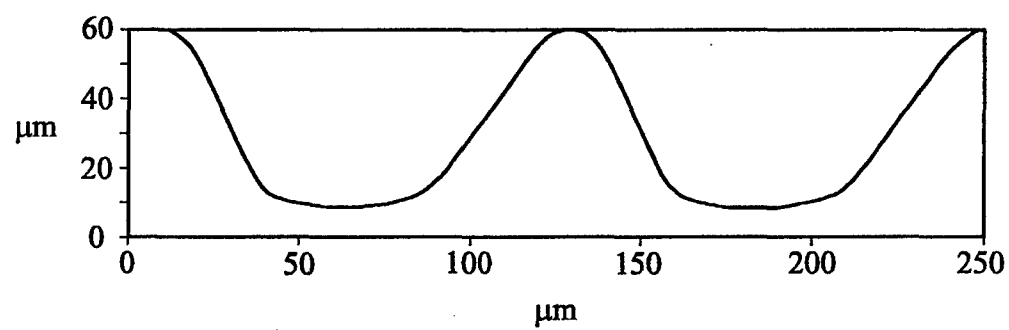


Figure 30: Grooves chemically etched in glass (Courtesy of D. Liepmann, University of California at Berkeley).

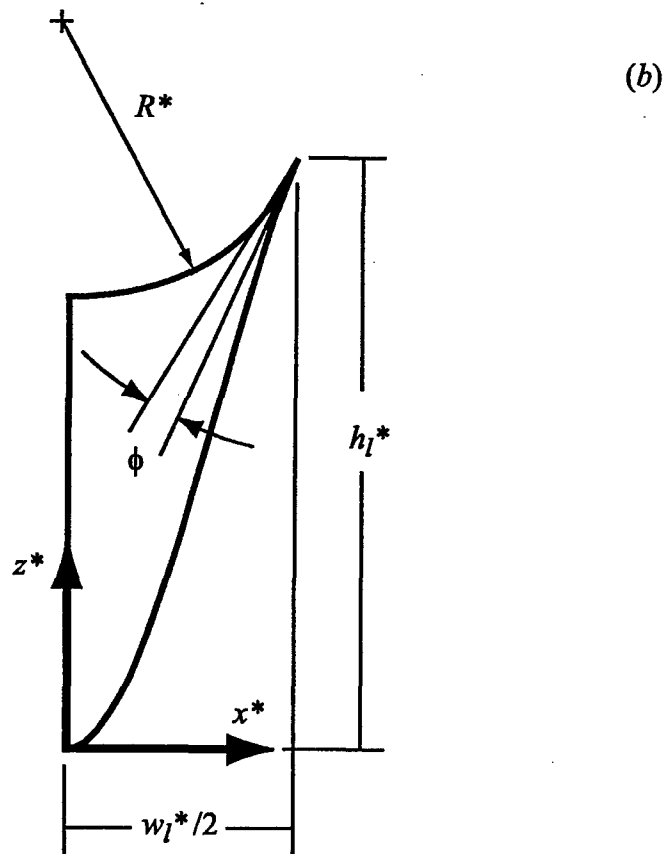
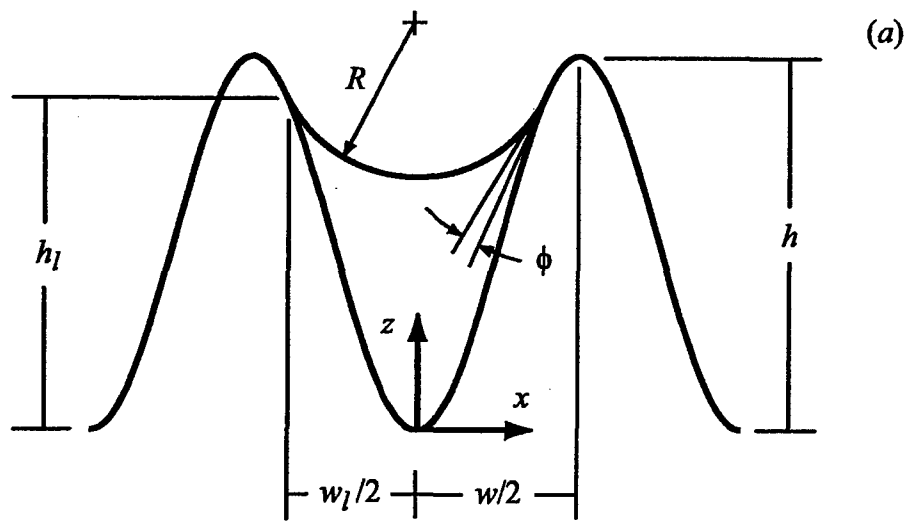


Figure 31: Flow of liquid in a sinusoidal groove: (a) Definition of geometric parameters; (b) Dimensionless solution domain.

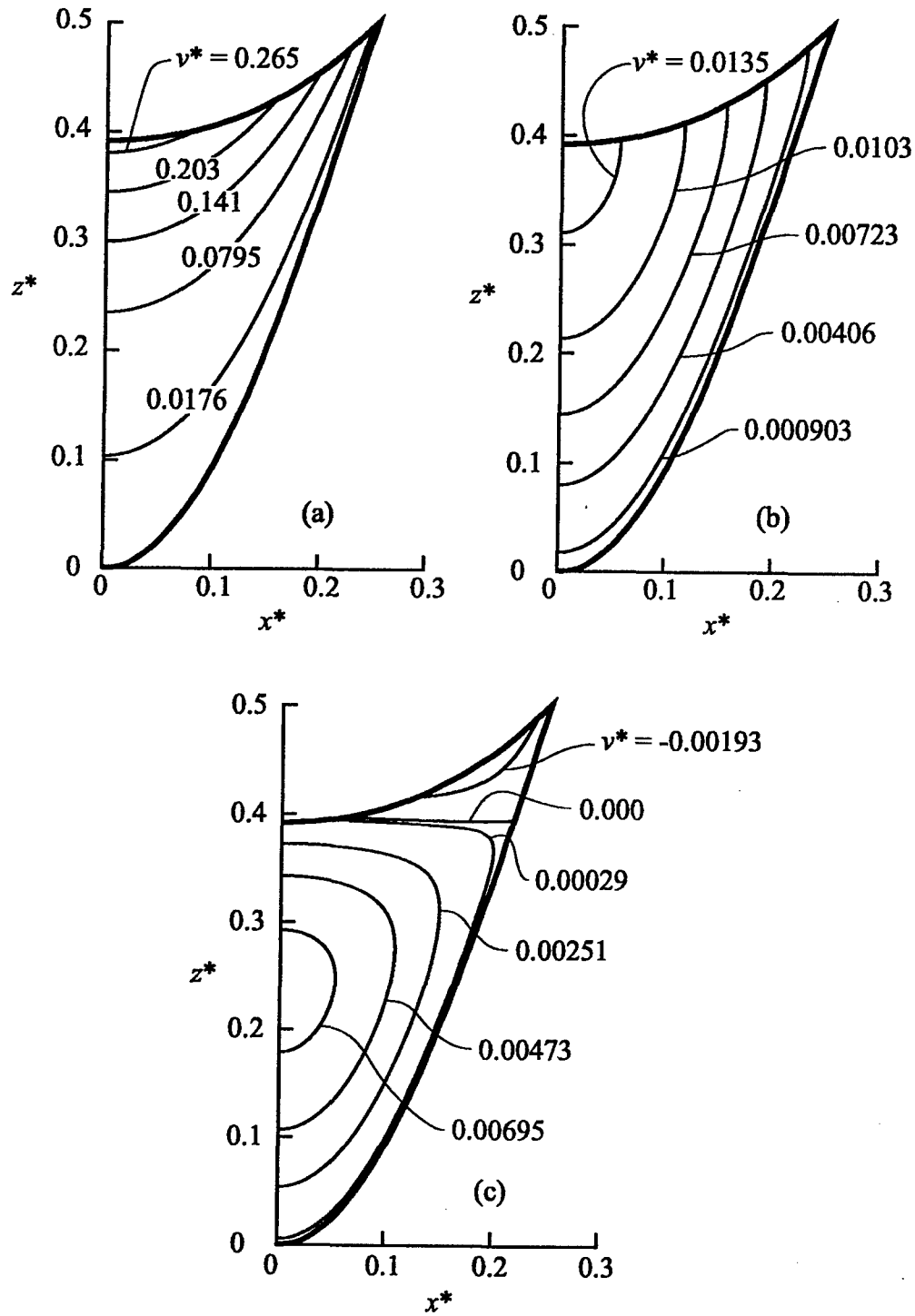


Figure 32: Dimensionless velocity fields for laminar flow in a sinusoidal groove ($\beta = 0.5$, $w_l^*/2 = 0.25$, $\phi = 25^\circ$): (a) $\tau_{lv}^* = 2.0$ (cocurrent flow); (b) $\tau_{lv}^* = 0.0$; (c) $\tau_{lv}^* = -0.1$ (countercurrent flow).

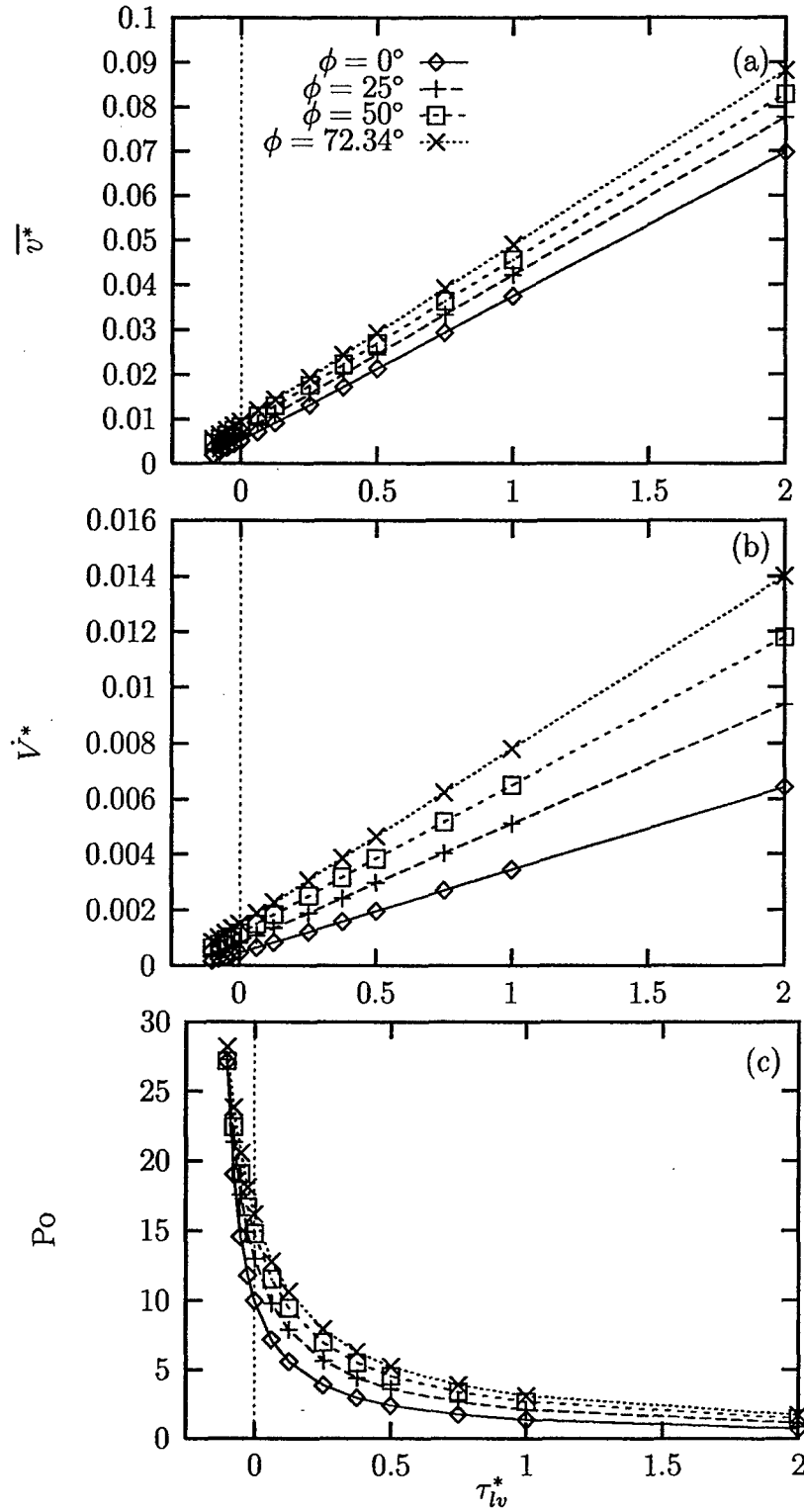


Figure 33: Variation of the flow variables with shear stress at the liquid-vapor interface for various values of meniscus contact angle ($\beta = 0.5$, $w_l^*/2 = 0.25$, $P^* = 1.15245$): (a) Mean velocity; (b) Volumetric flow rate; (c) Poiseuille number.

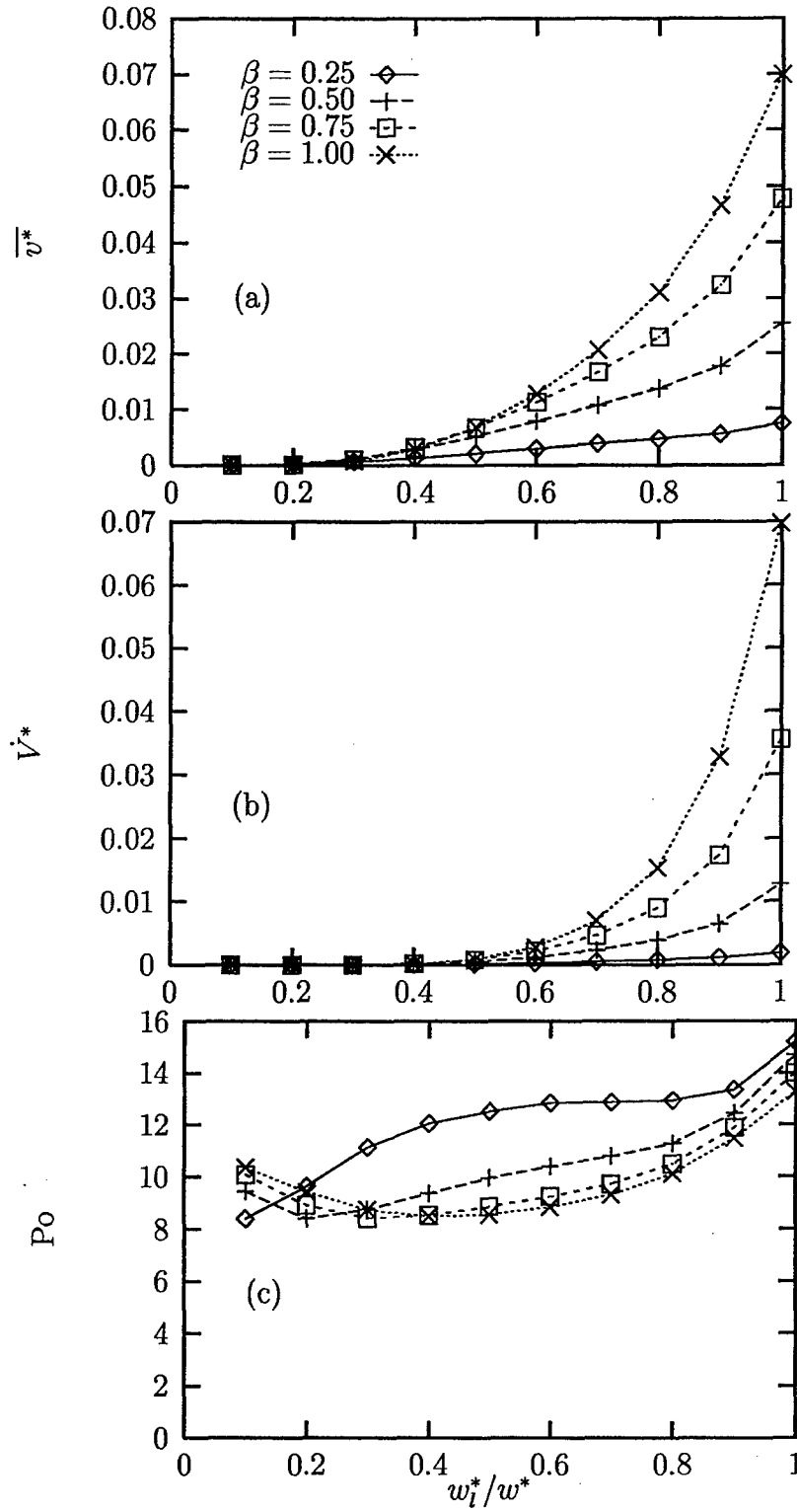


Figure 34: Variation of the flow variables with groove fill ratio for various values of groove aspect ratio ($\tau_{lv}^* = 0.0$, $\phi = 0^\circ$): (a) Mean velocity; (b) Volumetric flow rate; (c) Poiseuille number.

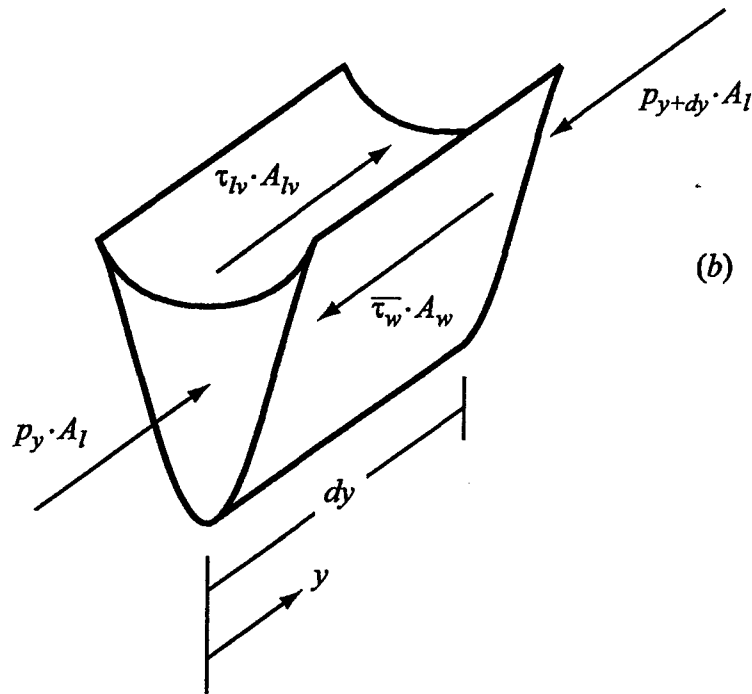
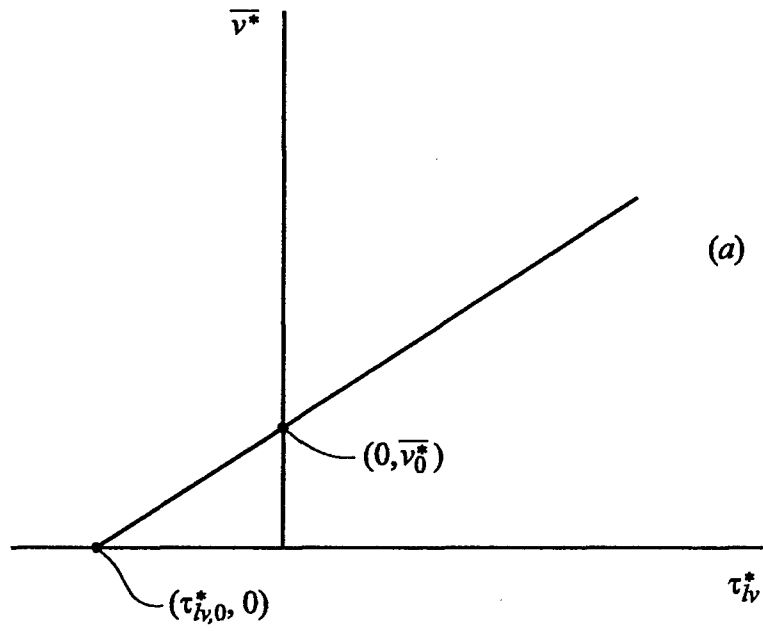


Figure 35: Semi-analytical solution for \overline{v}^* : (a) Definition of parameters; (b) Force balance on the liquid in a sinusoidal groove.

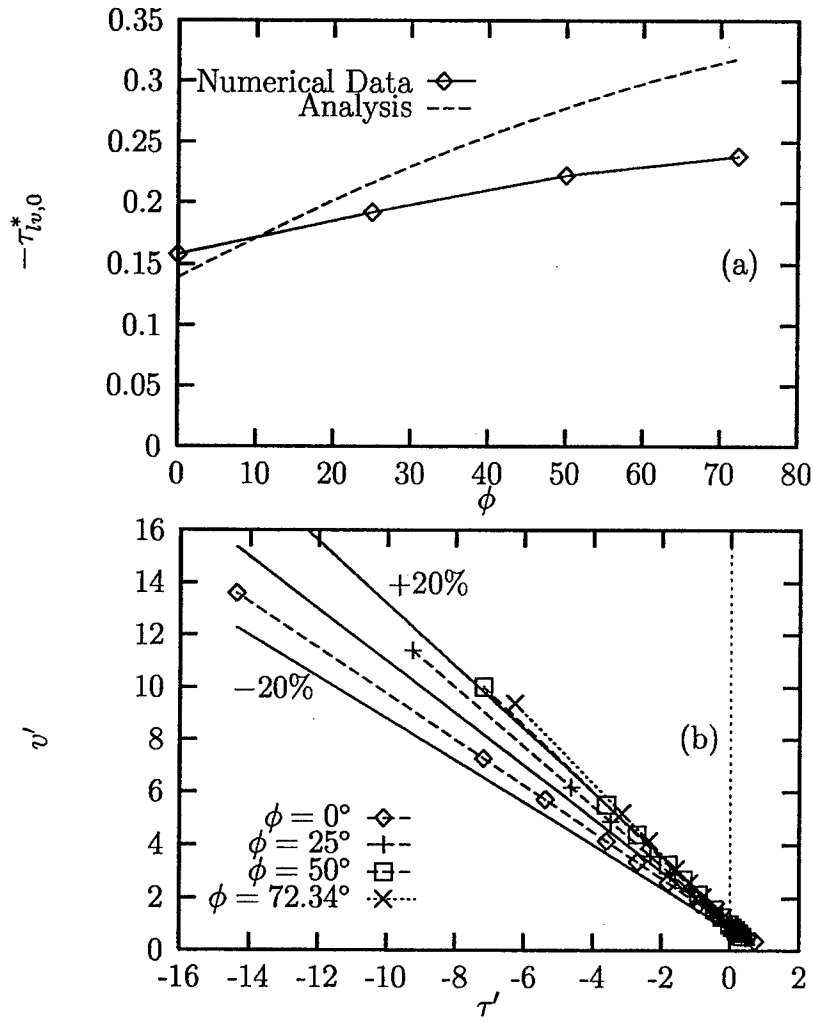


Figure 36: Comparison of the semi-analytical solution with numerical data ($\beta = 0.5$, $w_l^*/2 = 0.25$): (a) Countercurrent vapor shear stress required for $\overline{v^*} = 0$; (b) Normalized mean velocity versus normalized shear stress at the liquid-vapor interface.

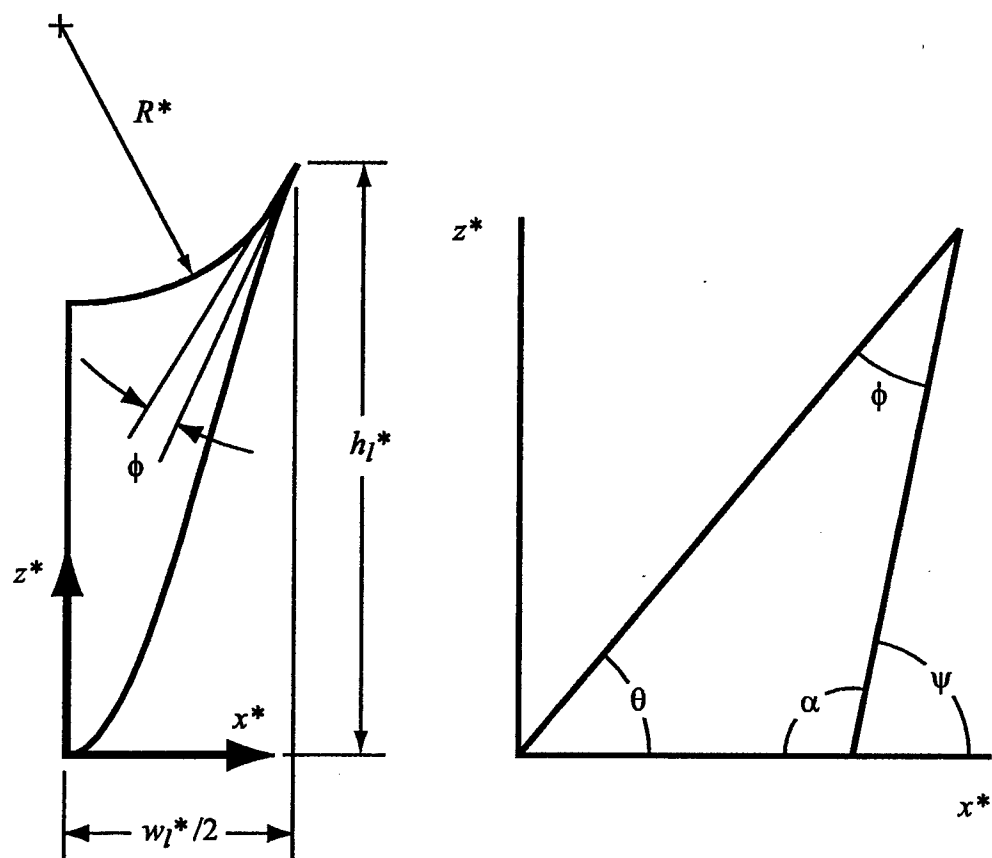


Figure 37: Definition of geometric parameters.

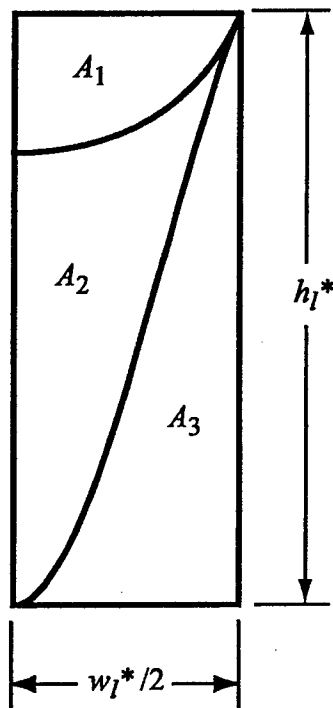


Figure 38: Determination of the cross-sectional area of the liquid.

4 Micro Capillary Pumped Loop Testing

4.1 Abstract

This project seeks to determine the operational characteristics of a micro-capillary pumped loop. This thermal management device is to be directly integrated into the silicon chips used in various devices. An experimental testbed has been constructed and calibrated while the test specimens were being manufactured. This chapter provides details concerning the experimental setup and preliminary calibration information, which will be used in the near future when a fully instrumented micro-capillary pumped loop will be tested.

4.2 Experimental Setup

The objective of these experiments was to determine the heat transfer capabilities of micro-Capillary Pumped Loops (μ CPLs) which are formed using a layer of borosilicate glass anodically bonded to a silicon wafer. These μ CPLs are being tested to determine their suitability for the thermal management of microprocessors.

Figure 39 shows two typical μ CPL designs. Several μ CPLs were manufactured on a 3.9-inch dia. silicon wafer at the University of California at Berkeley using photolithographic techniques. The individual μ CPLs were cut from the wafer using a diamond saw on a mini vertical mill. The μ CPLs consisted of a series of channels etched in the silicon wafer. These channels made up part of the evaporator section, the condenser section, and the interconnecting vapor and liquid lines. In addition, a hole was etched completely through the silicon to allow the installation of a fill tube, which would in turn be attached to a remote working fluid reservoir. A thin sheet of borosilicate glass was bonded to the front of the silicon. This glass had grooves etched into the sections that were positioned over the evaporator and condenser sections of the μ CPL. These grooves acted as a wick structure and provided the capillary pressure that was required for circulation of the working fluid. In an actual application, the glass would be replaced by another sheet of silicon, but for experimental purposes, glass was used to allow observation of the working fluid while the μ CPL was being tested. Another reason that glass was used was that, while silicon is virtually transparent to the CO₂ laser energy, the borosilicate glass absorbed a significant

portion of the incident laser light. This heated the glass and provided the source of thermal energy needed for testing the μ CPLs.

Figure 40 shows an overall schematic diagram of the experimental setup. This setup provided a means to input heat to the μ CPL evaporator section using a laser, extract heat from the condenser section using a calorimeter, insulate the μ CPL from parasitic heat losses, and record temperature data. In addition, photographic records of the tests could be collected.

The μ CPL wafer was enclosed in a stainless steel vacuum chamber to reduce natural convective heat losses from the surface. The chamber could be evacuated to a pressure of less than 10^{-3} Torr (Varian Turbo-V450 vacuum pump), which was measured using a thermocouple gauge and a more accurate ionization gauge (Varian Model 0571-K2471-303). In addition, multi-layer mylar radiation insulation was installed on the interior of the vacuum chamber to reduce thermal radiation heat transfer. The μ CPL was isolated from conductive heat transfer by using an acrylic holding fixture, as shown in Fig. 41. Grooves were machined in the upper and lower acrylic fixtures to hold the μ CPL. The fixtures were in turn mounted to an aluminum ring, which was held in the chuck of a micrometer stage. This stage could rotate the aluminum ring, as well as move it horizontally and vertically, to position the μ CPL in front of the ZnSe window in the end of the vacuum chamber.

Heat was applied to the μ CPL evaporator section by a 25-Watt CO₂ laser (Synrad Model J48-2W). Since the wavelength of this laser ($10.5\ \mu\text{m}$) is not in the visible range, a Helium-Neon laser (Uniphase Novette 1508-0) was used to determine the location of the CO₂ laser spot. Alignment was verified by placing a piece of paper in front of the vacuum chamber and burning it slightly with the CO₂ laser. After the CO₂ laser was deactivated, the removable mirror M1 (Fig. 40) was then installed, and the HeNe was activated. The HeNe laser beam was then aligned with the burn spot using adjusting screws on the removable mirror. Once the two beams were aligned, changing the angle of the turning mirror M2 would redirect both laser beams. In this way, the CO₂ laser beam could be aimed onto the μ CPL evaporator using the HeNe and the adjusting screws on the turning mirror M2. The CO₂ laser beam was turned, focused with a plano-convex lens (ZnSe, 1.5 inch dia., 30 ft focal length, AR coated for $9.2 - 10.6\ \mu\text{m}$), and passed through a window (ZnSe, AR coated for $9.2 - 10.6\ \mu\text{m}$) into the vacuum chamber. The focusing lens provided a means to control the diameter

of the beam at the surface of the test specimen, and therefore the heat flux applied to the evaporator of the μ CPL. The CO₂ laser beam was directed through a length of PVC pipe to reduce the possibility of foreign objects accidentally being placed in the path of the invisible beam, which would have caused a hazardous situation. There were also beam stops made of plexiglas, which is opaque to CO₂ laser light, along the sides of the beam path.

A water-cooled calorimeter was designed and manufactured to determine the heat rate transported by the μ CPL (Fig. 42). It consisted of a small block of copper with stainless steel tubing silver-soldered into holes which had been drilled into one face of the block. A hole was drilled into another face of the block, which simultaneously opened both tubes. This face was then adhered to the μ CPL using RTV sealant such that the coolant was in direct contact with the glass or silicon. The vacuum chamber had pass-through fittings to allow the coolant to flow to and from the calorimeter. Tygon tubing was used in the interior of the vacuum chamber to connect the calorimeter to the pass-through fittings. Type E thermocouples were placed in the coolant inlet and outlet lines within the vacuum chamber as close to the calorimeter as was practical. In this way, convective and conductive heat losses from the tygon tubing and along the length of the thermocouple wires to the ambient were mitigated. As shown in Fig. 40, an open reservoir was used to deliver coolant (water) at a constant mass flow rate to the calorimeter. The coolant line from the reservoir to the calorimeter was heavily insulated to reduce temperature swings when the room air conditioner cycled on and off. The mass flow rate of the water flowing through the calorimeter was calculated using a stopwatch and a Mettler scale (Model PC 4400).

Three electrical feedthroughs were mounted on the top of the chamber. One feedthrough supplied electrical power to the interior of the chamber. The other two were five-pair, Type E (Chromel/Constantan) thermocouple feedthroughs. The thermocouples that were used to make temperature measurements directly on the different points of the μ CPL were attached to the backside of the silicon using Kapton Tape or vacuum epoxy, as shown in Fig. 43.

A digital-capable video camera (Panasonic GP-KR222) with a long-range microscope lens and a monitor with a VCR were used to observe the μ CPLs while they were being tested. The camera was suspended just above the path of the CO₂ laser beam to reduce parallax. Image- and video-capturing software was used to store pictures and videos directly to a PC

during transient events such as start-up, boiling and dry-out.

4.2.1 Calibration

In order to accurately test the μ CPLs, the amount of laser power delivered to the wafer had to be quantified. The thermocouples used for sensing the temperature of the wafer and the coolant inlet and outlet had to be calibrated. This section gives a detailed description of the procedures used to achieve these calibrations.

Laser Controller Calibration

The CO₂ laser beam was attenuated and partially reflected as it passed through the vacuum chamber window, and partially reflected when it struck the μ CPL wafer. Therefore, it was necessary to calibrate to determine the above-mentioned losses. Power measurements were taken in front of and behind the vacuum chamber window. This provided a measure of the amount of attenuation/reflection caused by the window. The power output of the laser was measured by a calibrated optical power meter/disk thermopile combination (Newport Models 1815-C and 818T-10). A small blank wafer of the glass/silicon sandwich, instrumented with a water-cooled calorimeter inside the evacuated chamber, was used to determine the amount of power actually absorbed by the wafer. The amount of laser power incident on the window and the wafer, as well as the amount of power extracted by the calorimeter, were calibrated to the laser controller setting (LCS), which was in terms of the percentage of the full power output of the laser. In a preliminary setup, a ZnSe beam splitter was used with the power meter to directly measure the laser power output. However, it was determined that this arrangement caused the amount of laser power delivered to the wafer to fluctuate significantly, due to the dependence of the reflectivity of the beam splitter on the wavelength of the laser. Line hopping, or the variation of the wavelength of the CO₂ laser with respect to time, could not be avoided, so the beam splitter was removed from the system.

The following procedure was used to obtain the power readings in front of and behind the chamber:

1. Turn on the recirculating chiller, external pump and power supply for the CO₂ laser.

2. Using the HeNe laser, position the power meter in front of the chamber ("fore" position).
3. Remove the M1 mirror from the kinematic mount.
4. Set the laser controller setting to 1.0%.
5. Turn on the CO₂ laser.
6. After a short warm-up period, collect 500 data points using the power meter in front of the chamber.
7. Interrupt the beam with the laser aperture shutter on top of the laser.
8. Place the power meter behind the chamber ("aft" position).
9. Open the shutter on the laser.
10. Collect 500 data points using the power meter behind the chamber.
11. Using this method, alternate between the fore and aft positions until four calibration points (500 data points each) have been collected both in front of and behind the chamber.
12. Repeat steps 4 through 11, incrementing up through the desired controller settings.
13. Using the same procedure, start at the maximum LCS value and work back down through the specified settings. This will produce eight calibration points at each location (fore and aft) for each laser controller setting.

The procedure for determining the amount of power extracted by the water-cooled calorimeter on the blank wafer is as follows:

1. Turn on the recirculating chiller, external pump and power supply for the CO₂ laser.
2. Position the power meter in front of the vacuum chamber to validate the laser power setting.

3. Set the laser controller setting to 1.0%.
4. Turn on the CO₂ laser.
5. After a short warm-up period, collect 500 data points using the power meter in front of the chamber.
6. Interrupt the beam with the laser aperture shutter on top of the laser.
7. Remove the power meter.
8. Start the coolant flow rate to the calorimeter.
9. Open the shutter on the laser.
10. Adjust the coolant flow rate so the temperature increase across the calorimeter is approximately 2°C.
11. Allow the calorimeter temperatures to reach steady state (approximately 30 min.).
12. Take 8 sets of 600 data points for the calorimeter inlet and outlet temperatures. For each set, measure the mass flow rate through the calorimeter.
13. Reinstall the power meter in front of the vacuum chamber and collect 500 data points for the laser power at that location.
14. Repeat steps 3 through 13, incrementing up through the desired controller settings.

Figures 44(a) and 44(b) show typical traces obtained during calibration for the calorimeter temperature difference and the laser power versus time, respectively. In addition, Fig. 44(c) shows the results of the calibration with respect to the laser controller setting. It should be noted that the borosilicate glass melted at LCS = 30%, as indicated by the brackets surrounding this data. Tables 9—11 provide the actual values presented in Fig. 44(c). The linear best-fit equations for the data in Fig. 44(c) are as follows:

$$\dot{Q}_{\text{window}} = 0.2874 * \text{LCS} \quad (R^2 = 0.9997) \quad (110)$$

$$\dot{Q}_{\text{in}} = 0.2581 * \text{LCS} \quad (R^2 = 0.9992) \quad (111)$$

$$\dot{Q}_{\text{out}} = 0.2011 * \text{LCS} \quad (R^2 = 0.9974) \quad (112)$$

The linear equation for the power absorbed by the wafer does not include the data at LCS = 30%. In comparing eqns. (111) and (112), the amount of incident laser power absorbed by the borosilicate glass is approximately 78%.

Thermocouple Calibration

The thermocouples used for wall temperature measurements and calorimetry were calibrated using a recirculating chiller (Lauda Model RC20) with a serial interface (Lauda Model R61) and an RTD (Hart Scientific model 5691). The working bath of the chiller was filled with PAO oil to allow for more stable temperatures. In the bath, there was a length of copper pipe with a flat sheet of copper silver-soldered over one end. Copper was chosen for its high thermal conductivity. This sheet of copper acted as a cap and a base. The other end of the copper pipe was left open. This allowed it to be filled with water and immersed in the oil bath, keeping the open end of the tube above the surface of the oil. The RTD and thermocouples were placed in the water in this copper tube, to protect them from the oil in the bath. The thermocouples were attached to the RTD, and the RTD was supported using a lab clamp to insure that it did not contact the sides or the base of the copper tube. The target temperature of the bath was set by a PC, which also read the RTD temperature and received information on the thermocouple temperatures from a data acquisition unit (Hewlett Packard Model HP34970A). The data acquisition and temperature settings were controlled by an Excel/Visual Basic for Applications program. A test program was written to determine the length of time necessary for the RTD and thermocouple readings inside the water-filled copper tube to reach steady state. The temperature of the bath was set to 38°C, and allowed to stabilize for 30 min. The program then set the target bath temperature to 40°C, and began taking data from the bath temperature sensor, the RTD, and a thermocouple. Scans were recorded continuously for approximately 2 hr as shown in Fig. 45. It was determined that the readings of the RTD and the thermocouple in the water reached steady state after approximately 30 min.

After the time taken to reach steady state was known, the actual calibration tests could be performed. A new program was written which initially set the bath temperature to 10°C, waited for 60 min., and then took 100 data points of 5 scans each. The 60-min. interval was

decided on because it should have given more than enough time for the readings to reach steady state. The program then incremented the temperature to 15°C, waited one hr, and recorded data again. It continued in this manner from 10°C to 95°C, in 5°C increments. After it had been set at 95°C for one hr and had taken the data for that temperature, it then went down to 92.5°C. From there, it went down in the same manner (5°C intervals with 60-min. time intervals) to 12.5°C. When the program was finished, there were 500 data points for each temperature from 10°C to 95°C in increments of 2.5°C. This raw data was used to determine the calibration curves for the twelve thermocouples. The temperature reading of each thermocouple was plotted against the reading of the RTD. A linear best-fit line was determined in the form $T_{\text{actual}} = mT_{\text{reading}} + b$, as shown in Fig. 46(a). Next, all of the temperature measurements for a specific thermocouple were evaluated by its respective best-fit equation. The difference between the value from the equation and the corresponding RTD value was calculated as shown in Fig. 46(b). This difference plus the stated NIST-traceable uncertainty of the RTD ($\pm 0.005^\circ\text{C}$) was the final uncertainty for any subsequent temperature measurements for a given thermocouple (Table 12). Thermocouples 211 and 212 were used in the calorimeter. Since the coolant temperature was not anticipated to rise above 40°C, only the calibration data between 10°C and 40°C were used when calibrating these two thermocouples. There were some outlying data points that were disregarded when reporting the maximum errors in Table 12. There were no more than 10 out of 3500 of these points dropped from each graph.

4.2.2 Uncertainty Analysis

The formula used for finding the mass flow rate of coolant flowing through the calorimeter is

$$\dot{m} = \frac{m}{t} \quad (113)$$

The root-sum-square uncertainty for the mass flow rate is

$$\begin{aligned} \Delta\dot{m} &= \sqrt{\left(\frac{\partial\dot{m}}{\partial m}\Delta m\right)^2 + \left(\frac{\partial\dot{m}}{\partial t}\Delta t\right)^2} \\ &= \sqrt{\left(\frac{1}{t}\Delta m\right)^2 + \left(\frac{-m}{t^2}\Delta t\right)^2} \end{aligned} \quad (114)$$

The amount of heat removed from the μCPL by the calorimeter can be expressed by

$$\dot{Q}_{\text{out}} = \dot{m}C_p(T_{\text{out}} - T_{\text{in}}) \quad (115)$$

The uncertainty for values found using this equation is

$$\begin{aligned} \Delta\dot{Q}_{\text{out}} &= \sqrt{\left(\frac{\partial\dot{Q}_{\text{out}}}{\partial\dot{m}}\Delta\dot{m}\right)^2 + \left(\frac{\partial\dot{Q}_{\text{out}}}{\partial C_p}\Delta C_p\right)^2 + \left(\frac{\partial\dot{Q}_{\text{out}}}{\partial T_{\text{out}}}\Delta T_{\text{out}}\right)^2 + \left(\frac{\partial\dot{Q}_{\text{out}}}{\partial T_{\text{in}}}\Delta T_{\text{in}}\right)^2} \\ &= \sqrt{[C_p(T_{\text{out}} - T_{\text{in}})\Delta\dot{m}]^2 + [\dot{m}(T_{\text{out}} - T_{\text{in}})\Delta C_p]^2 + (\dot{m}C_p\Delta T_{\text{out}})^2 + (\dot{m}C_p\Delta T_{\text{in}})^2} \end{aligned} \quad (116)$$

The thermal resistances based on incident laser power and power extracted by the calorimeter, respectively, are

$$R_{\text{th,in}} = \frac{(T_{\text{v,e}} - T_{\text{v,c}})}{\dot{Q}_{\text{in}}} \quad (117)$$

$$R_{\text{th,out}} = \frac{(T_{\text{v,e}} - T_{\text{v,c}})}{\dot{Q}_{\text{out}}} \quad (118)$$

The uncertainties for these thermal resistance equations are

$$\begin{aligned} \Delta R_{\text{th,in}} &= \sqrt{\left(\frac{\partial R_{\text{th,in}}}{\partial T_{\text{v,e}}}\Delta T_{\text{v,e}}\right)^2 + \left(\frac{\partial R_{\text{th,in}}}{\partial T_{\text{v,c}}}\Delta T_{\text{v,c}}\right)^2 + \left(\frac{\partial R_{\text{th,in}}}{\partial \dot{Q}_{\text{in}}}\Delta \dot{Q}_{\text{in}}\right)^2} \\ &= \sqrt{\left(\frac{\Delta T_{\text{v,e}}}{\dot{Q}_{\text{in}}}\right)^2 + \left(\frac{\Delta T_{\text{v,c}}}{\dot{Q}_{\text{in}}}\right)^2 + \left(\frac{(T_{\text{v,e}} - T_{\text{v,c}})}{\dot{Q}_{\text{in}}^2}\Delta \dot{Q}_{\text{in}}\right)^2} \end{aligned} \quad (119)$$

$$\begin{aligned} \Delta R_{\text{th,out}} &= \sqrt{\left(\frac{\partial R_{\text{th,out}}}{\partial T_{\text{v,e}}}\Delta T_{\text{v,e}}\right)^2 + \left(\frac{\partial R_{\text{th,out}}}{\partial T_{\text{v,c}}}\Delta T_{\text{v,c}}\right)^2 + \left(\frac{\partial R_{\text{th,out}}}{\partial \dot{Q}_{\text{out}}}\Delta \dot{Q}_{\text{out}}\right)^2} \\ &= \sqrt{\left(\frac{\Delta T_{\text{v,e}}}{\dot{Q}_{\text{out}}}\right)^2 + \left(\frac{\Delta T_{\text{v,c}}}{\dot{Q}_{\text{out}}}\right)^2 + \left(\frac{(T_{\text{v,e}} - T_{\text{v,c}})}{\dot{Q}_{\text{out}}^2}\Delta \dot{Q}_{\text{out}}\right)^2} \end{aligned} \quad (120)$$

4.3 Summary and Future Work

This report documents the status of the project as of the end of Summer 2001. A great deal of the experimental setup is complete and has been thoroughly calibrated. A new generation of μCPLs have been fabricated, and are in the process of being diced and instrumented. A major problem in the past has been making sure that the μCPL is hermetically sealed. To

address this problem, the vacuum-tightness of the μ CPL will be evaluated using a helium leak detection unit. The μ CPL will then be charged and tested in the vacuum chamber to determine the operating characteristics for various power input levels. Problems are anticipated with respect to the start-up behavior. The interaction between the μ CPL and the working fluid reservoir is unknown at present, but will be controllable with an electrical heater tape mounted to the reservoir.

Table 9: Laser calibration data.

LCS (%)	$\dot{Q}_{\text{window}} \pm \sigma$ (W)	$\dot{Q}_{\text{in}} \pm \sigma$ (W)	$\dot{Q}_{\text{out}} \pm \Delta\dot{Q}_{\text{out}}$ (W)
1	0.295 ± 0.0034	0.265 ± 0.011	$0.123 \pm 9\%$
1	0.292 ± 0.0025	0.261 ± 0.0080	$0.120 \pm 9\%$
1	0.293 ± 0.0044	0.253 ± 0.0026	$0.126 \pm 8\%$
1	0.290 ± 0.0063	0.256 ± 0.0043	$0.124 \pm 9\%$
1	0.290 ± 0.0010	0.273 ± 0.0054	$0.123 \pm 7\%$
1	0.291 ± 0.0042	0.271 ± 0.0043	$0.122 \pm 8\%$
1	0.294 ± 0.0023	0.268 ± 0.0019	$0.118 \pm 7\%$
1	0.307 ± 0.0028	0.287 ± 0.0036	$0.113 \pm 8\%$
1.5	0.411 ± 0.0077	0.360 ± 0.012	$0.186 \pm 8\%$
1.5	0.408 ± 0.0060	0.356 ± 0.0058	$0.183 \pm 6\%$
1.5	0.409 ± 0.0054	0.362 ± 0.014	$0.177 \pm 7\%$
1.5	0.409 ± 0.0053	0.358 ± 0.0099	$0.177 \pm 6\%$
1.5	0.408 ± 0.0012	0.380 ± 0.0057	$0.173 \pm 6\%$
1.5	0.404 ± 0.0079	0.380 ± 0.0081	$0.173 \pm 6\%$
1.5	0.396 ± 0.0019	0.376 ± 0.0071	$0.172 \pm 6\%$
1.5	0.397 ± 0.0023	0.370 ± 0.0057	$0.166 \pm 6\%$
2	0.529 ± 0.0011	0.489 ± 0.0060	$0.303 \pm 8\%$
2	0.526 ± 0.0037	0.490 ± 0.0041	$0.305 \pm 7\%$
2	0.531 ± 0.0047	0.489 ± 0.0038	$0.310 \pm 7\%$
2	0.532 ± 0.0045	0.489 ± 0.0049	$0.309 \pm 7\%$
2	0.545 ± 0.0052	0.502 ± 0.0093	$0.315 \pm 7\%$
2	0.549 ± 0.0016	0.495 ± 0.0084	$0.307 \pm 7\%$
2	0.547 ± 0.0025	0.484 ± 0.0037	$0.316 \pm 7\%$
2	0.547 ± 0.0035	0.479 ± 0.0029	$0.323 \pm 6\%$
3	0.894 ± 0.0089	0.777 ± 0.0033	$0.580 \pm 8\%$
3	0.892 ± 0.0055	0.795 ± 0.015	$0.593 \pm 8\%$
3	0.890 ± 0.0032	0.795 ± 0.016	$0.585 \pm 9\%$
3	0.890 ± 0.0014	0.810 ± 0.012	$0.589 \pm 7\%$
3	0.915 ± 0.0031	0.811 ± 0.0049	$0.586 \pm 9\%$
3	0.921 ± 0.0027	0.812 ± 0.0059	$0.588 \pm 7\%$
3	0.922 ± 0.0032	0.809 ± 0.0032	$0.585 \pm 8\%$
3	0.921 ± 0.0037	0.807 ± 0.0031	$0.594 \pm 8\%$
4	1.15 ± 0.0079	1.05 ± 0.0054	$0.811 \pm 8\%$
4	1.14 ± 0.0086	1.01 ± 0.013	$0.796 \pm 8\%$
4	1.14 ± 0.0082	1.01 ± 0.0056	$0.811 \pm 8\%$
4	1.14 ± 0.012	1.02 ± 0.019	$0.790 \pm 8\%$
4	1.14 ± 0.0018	1.06 ± 0.0017	$0.803 \pm 8\%$
4	1.15 ± 0.0061	1.06 ± 0.0015	$0.808 \pm 9\%$
4	1.16 ± 0.011	1.08 ± 0.0040	$0.789 \pm 8\%$
4	1.17 ± 0.0027	1.08 ± 0.0064	$0.820 \pm 9\%$

Table 10: Laser calibration data, continued.

LCS (%)	$\dot{Q}_{\text{window}} \pm \sigma$ (W)	$\dot{Q}_{\text{in}} \pm \sigma$ (W)	$\dot{Q}_{\text{out}} \pm \Delta\dot{Q}_{\text{out}}$ (W)
5	1.49 ± 0.015	1.33 ± 0.016	$1.01 \pm 6\%$
5	1.48 ± 0.0031	1.32 ± 0.0024	$1.01 \pm 6\%$
5	1.48 ± 0.0030	1.34 ± 0.015	$1.03 \pm 7\%$
5	1.49 ± 0.013	1.36 ± 0.0058	$1.02 \pm 5\%$
5	1.50 ± 0.0024	1.39 ± 0.0018	$1.01 \pm 5\%$
5	1.49 ± 0.0066	1.38 ± 0.0059	$1.03 \pm 5\%$
5	1.49 ± 0.0045	1.38 ± 0.0064	$1.02 \pm 5\%$
5	1.49 ± 0.0018	1.38 ± 0.0034	$1.02 \pm 5\%$
10	2.96 ± 0.010	2.66 ± 0.036	$2.08 \pm 4\%$
10	2.97 ± 0.016	2.64 ± 0.024	$2.07 \pm 3\%$
10	2.97 ± 0.012	2.72 ± 0.039	$2.09 \pm 4\%$
10	2.97 ± 0.0045	2.67 ± 0.042	$2.08 \pm 4\%$
10	3.02 ± 0.044	2.72 ± 0.0042	$2.06 \pm 3\%$
10	2.97 ± 0.0055	2.73 ± 0.0035	$2.10 \pm 4\%$
10	2.96 ± 0.0042	2.73 ± 0.0045	$2.04 \pm 4\%$
10	2.96 ± 0.0026	2.72 ± 0.0040	$2.03 \pm 6\%$
15	4.31 ± 0.024	3.90 ± 0.057	$3.07 \pm 5\%$
15	4.30 ± 0.014	3.91 ± 0.0046	$3.12 \pm 5\%$
15	4.32 ± 0.030	3.91 ± 0.0040	$3.10 \pm 6\%$
15	4.31 ± 0.028	3.83 ± 0.083	$3.06 \pm 5\%$
15	4.37 ± 0.032	3.92 ± 0.069	$3.00 \pm 8\%$
15	4.35 ± 0.016	3.98 ± 0.0065	$3.11 \pm 6\%$
15	4.35 ± 0.017	3.98 ± 0.0047	$3.12 \pm 4\%$
15	4.35 ± 0.012	3.98 ± 0.0085	$3.06 \pm 5\%$
20	5.75 ± 0.076	5.18 ± 0.11	$4.05 \pm 6\%$
20	5.70 ± 0.0051	5.22 ± 0.14	$4.05 \pm 7\%$
20	5.75 ± 0.093	5.10 ± 0.0032	$4.08 \pm 7\%$
20	5.76 ± 0.10	5.16 ± 0.11	$4.15 \pm 7\%$
20	5.74 ± 0.0038	5.22 ± 0.0059	$4.16 \pm 7\%$
20	5.73 ± 0.0046	5.22 ± 0.0040	$4.16 \pm 7\%$
20	5.73 ± 0.0057	5.22 ± 0.0038	$4.10 \pm 6\%$
20	5.73 ± 0.0049	5.22 ± 0.0056	$4.18 \pm 8\%$

Table 11: Laser calibration data, continued.

LCS (%)	$\dot{Q}_{\text{window}} \pm \sigma$ (W)	$\dot{Q}_{\text{in}} \pm \sigma$ (W)	$\dot{Q}_{\text{out}} \pm \Delta\dot{Q}_{\text{out}}$ (W)
25	7.08 ± 0.12	6.36 ± 0.14	$4.88 \pm 6\%$
25	7.06 ± 0.0063	6.26 ± 0.039	$4.81 \pm 7\%$
25	7.07 ± 0.0058	6.29 ± 0.014	$4.88 \pm 8\%$
25	7.10 ± 0.039	6.28 ± 0.0068	$4.91 \pm 5\%$
25	7.10 ± 0.040	6.32 ± 0.052	$4.99 \pm 6\%$
25	7.09 ± 0.020	6.30 ± 0.035	$4.85 \pm 7\%$
25	7.11 ± 0.039	6.40 ± 0.0089	$4.92 \pm 6\%$
25	7.15 ± 0.061	6.41 ± 0.0052	$5.02 \pm 6\%$
30	8.65 ± 0.028	7.68 ± 0.0091	$6.13 \pm 7\%$
30	8.67 ± 0.029	7.78 ± 0.099	$6.23 \pm 6\%$
30	8.68 ± 0.038	7.88 ± 0.025	$6.30 \pm 8\%$
30	8.69 ± 0.035	7.86 ± 0.0078	$6.16 \pm 8\%$
30	8.62 ± 0.052	7.67 ± 0.023	$6.30 \pm 5\%$
30	8.63 ± 0.036	7.67 ± 0.028	$6.21 \pm 6\%$
30	8.61 ± 0.0050	7.69 ± 0.048	$6.27 \pm 6\%$
30	8.64 ± 0.034	7.72 ± 0.060	$6.14 \pm 6\%$
1	0.306 ± 0.0015	—	—
1	0.312 ± 0.0011	—	—
1.5	0.406 ± 0.0057	—	—
1.5	0.429 ± 0.0011	—	—
2	0.549 ± 0.0012	—	—
2	0.546 ± 0.0012	—	—
3	0.903 ± 0.0030	—	—
3	0.909 ± 0.0071	—	—
4	1.17 ± 0.0032	—	—
4	1.17 ± 0.0030	—	—
5	1.52 ± 0.0021	—	—
5	1.50 ± 0.0024	—	—
10	3.00 ± 0.0074	—	—
10	3.02 ± 0.0082	—	—
15	4.35 ± 0.0048	—	—
15	4.34 ± 0.0050	—	—
20	5.81 ± 0.0066	—	—
20	5.77 ± 0.010	—	—
25	7.14 ± 0.044	—	—
25	7.14 ± 0.039	—	—

Table 12: Thermocouple calibration equations: $T_{\text{actual}} = mT_{\text{reading}} + b$ (Valid ranges: TCs 201–210, $10^{\circ}\text{C} \leq T_{\text{reading}} \leq 95^{\circ}\text{C}$; TCs 211 and 212, $10^{\circ}\text{C} \leq T_{\text{reading}} \leq 40^{\circ}\text{C}$).

TC Number	m	b ($^{\circ}\text{C}$)	Max Error ($^{\circ}\text{C}$)
201	0.9952	1.2794	0.30
202	0.9962	1.0023	0.30
203	0.9956	0.9031	0.30
204	0.9952	0.6704	0.30
205	0.9958	0.4097	0.30
206	0.9965	0.1150	0.25
207	0.9935	0.1410	0.40
208	0.9968	0.0079	0.15
209	0.9965	-0.0507	0.25
210	0.9964	0.0122	0.15
211	0.9936	0.1318	-0.093
212	0.9947	-0.0919	-0.054

4.4 Nomenclature

C_p	specific heat, J/(kg-K)
LCS	laser controller setting, %
m	mass, kg
\dot{m}	mass flow rate, kg/s
\dot{Q}	rate of heat transfer, W
\dot{Q}_{in}	laser power incident on the blank wafer, W
\dot{Q}_{out}	power removed by the calorimeter mounted to the blank wafer, W
\dot{Q}_{window}	laser power incident on the window of the vacuum chamber, W
$R_{\text{th,in}}$	thermal resistance based on incident power, K/W
$R_{\text{th,out}}$	thermal resistance based on power removed by the calorimeter, K/W
t	time, s
T_{in}	calorimeter inlet temperature, K
T_{out}	calorimeter outlet temperature, K
$T_{\text{v,e}}$	vapor line temperature at the evaporator, K
$T_{\text{v,c}}$	vapor line temperature at the condenser, K

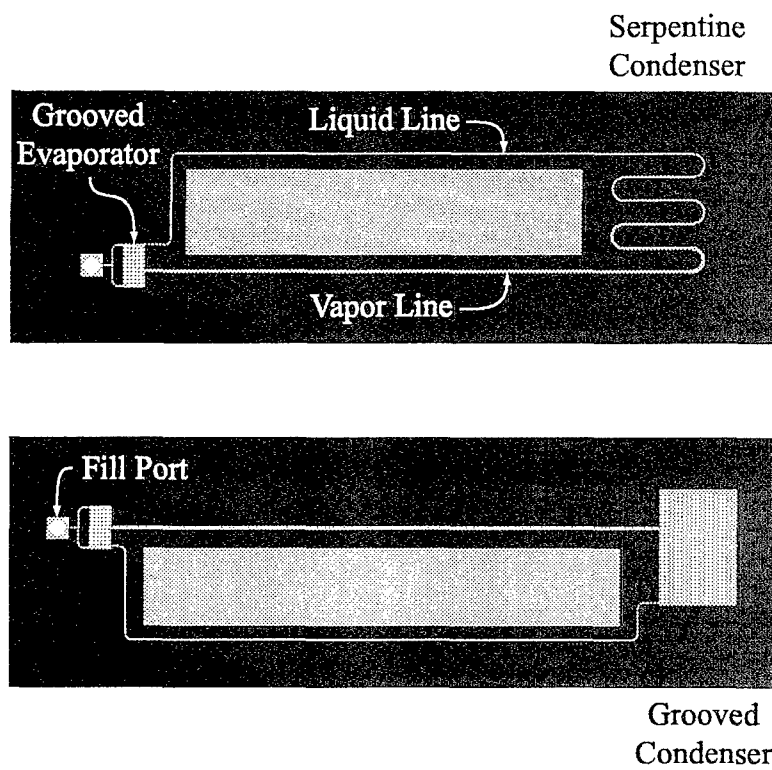


Figure 39: Variations of the basic μ CPL design.

BEST AVAILABLE COPY

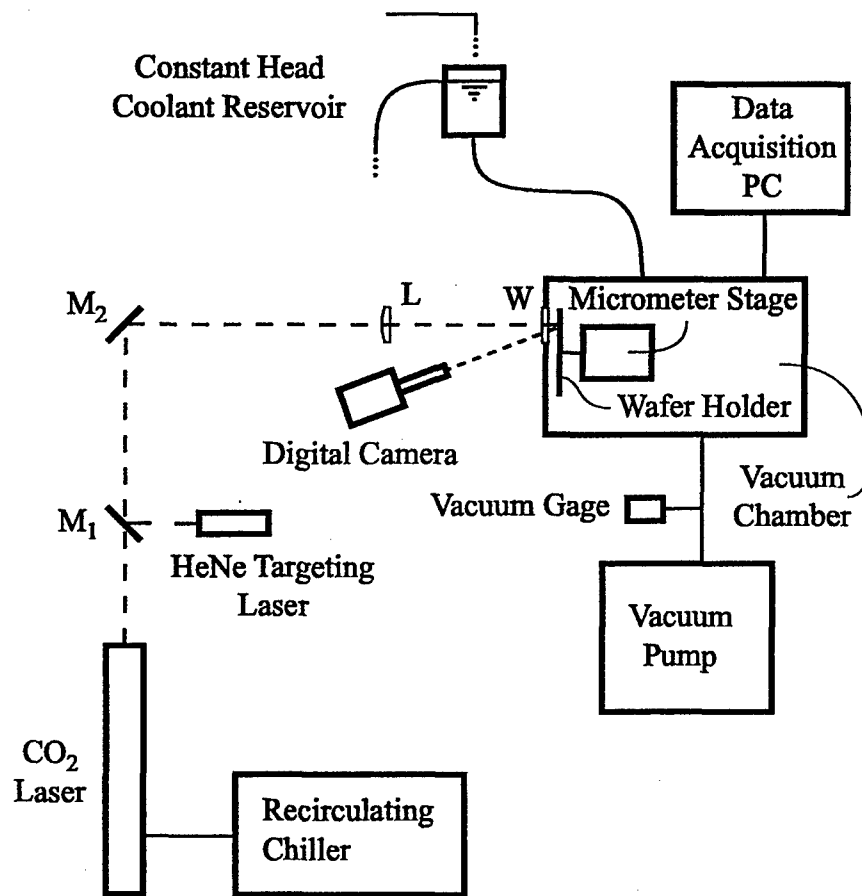


Figure 40: Schematic of μ -CPL test setup.

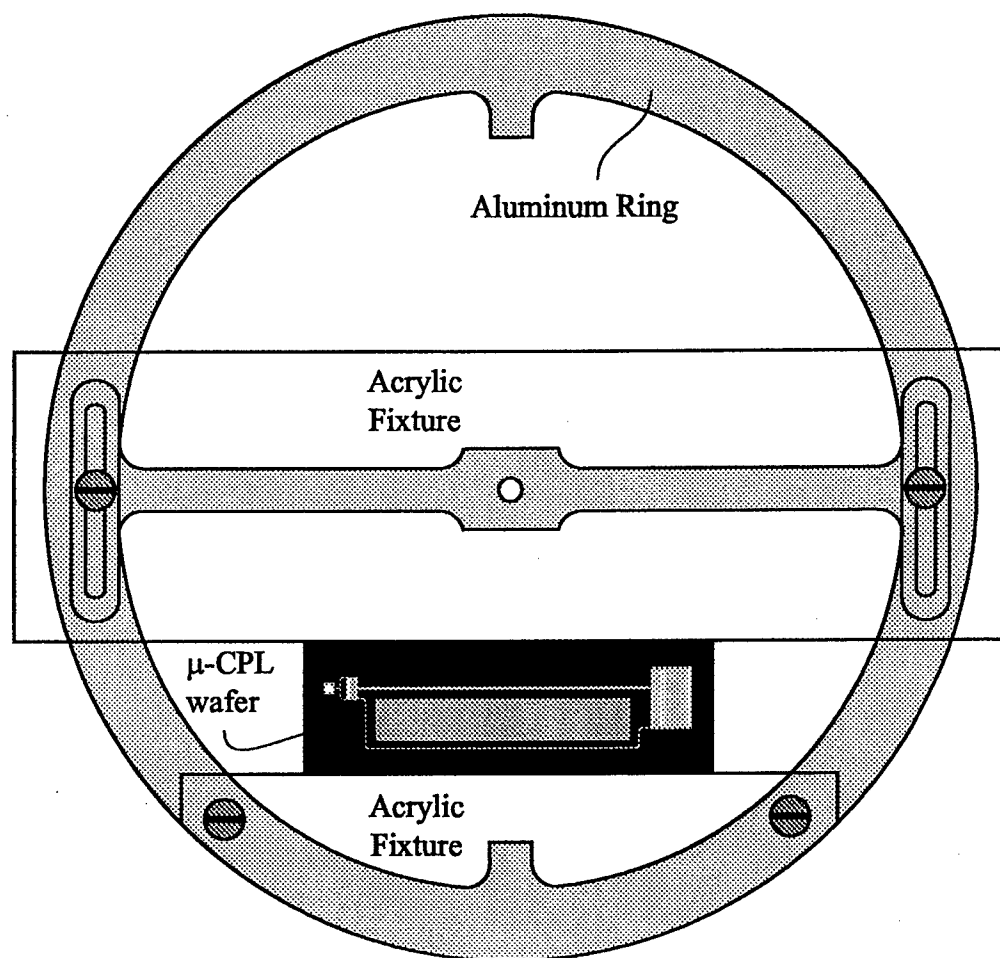


Figure 41: Mounting fixture for the μ CPL.

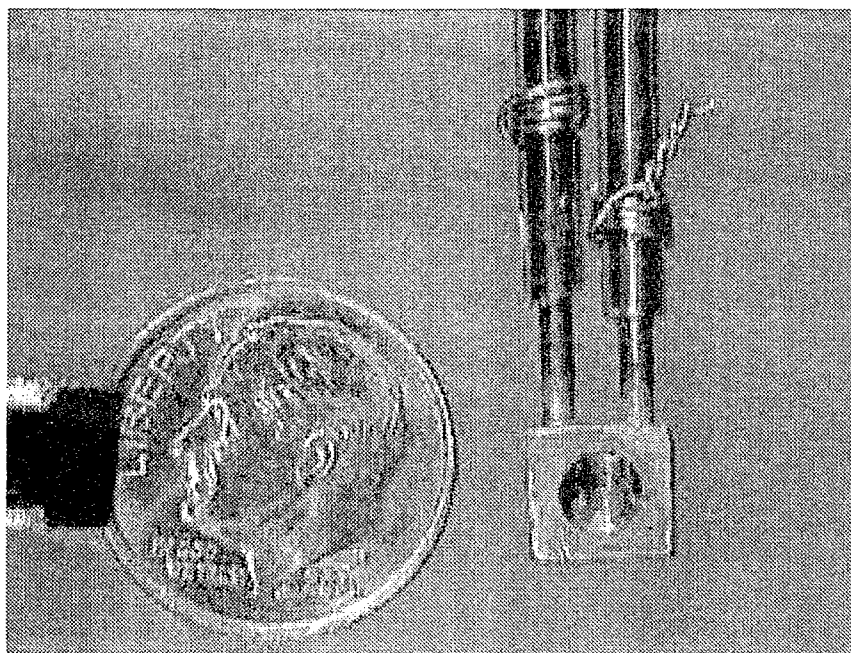


Figure 42: Photograph of the copper calorimeter.

BEST AVAILABLE COPY

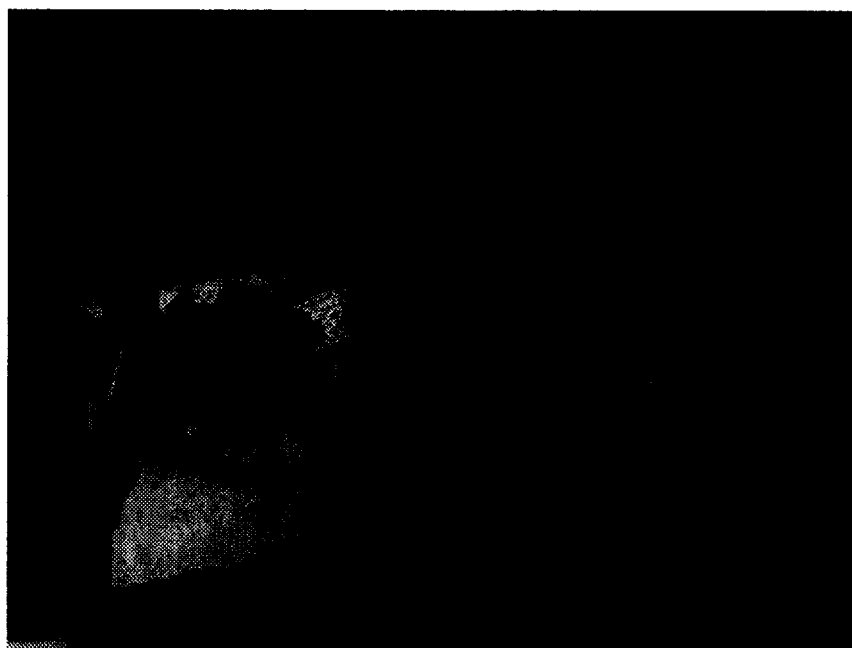


Figure 43: Photograph showing thermocouples adhered to the back of the μ CPL wafer with vacuum epoxy. The stainless steel fill tube is on the left-hand side.

BEST AVAILABLE COPY

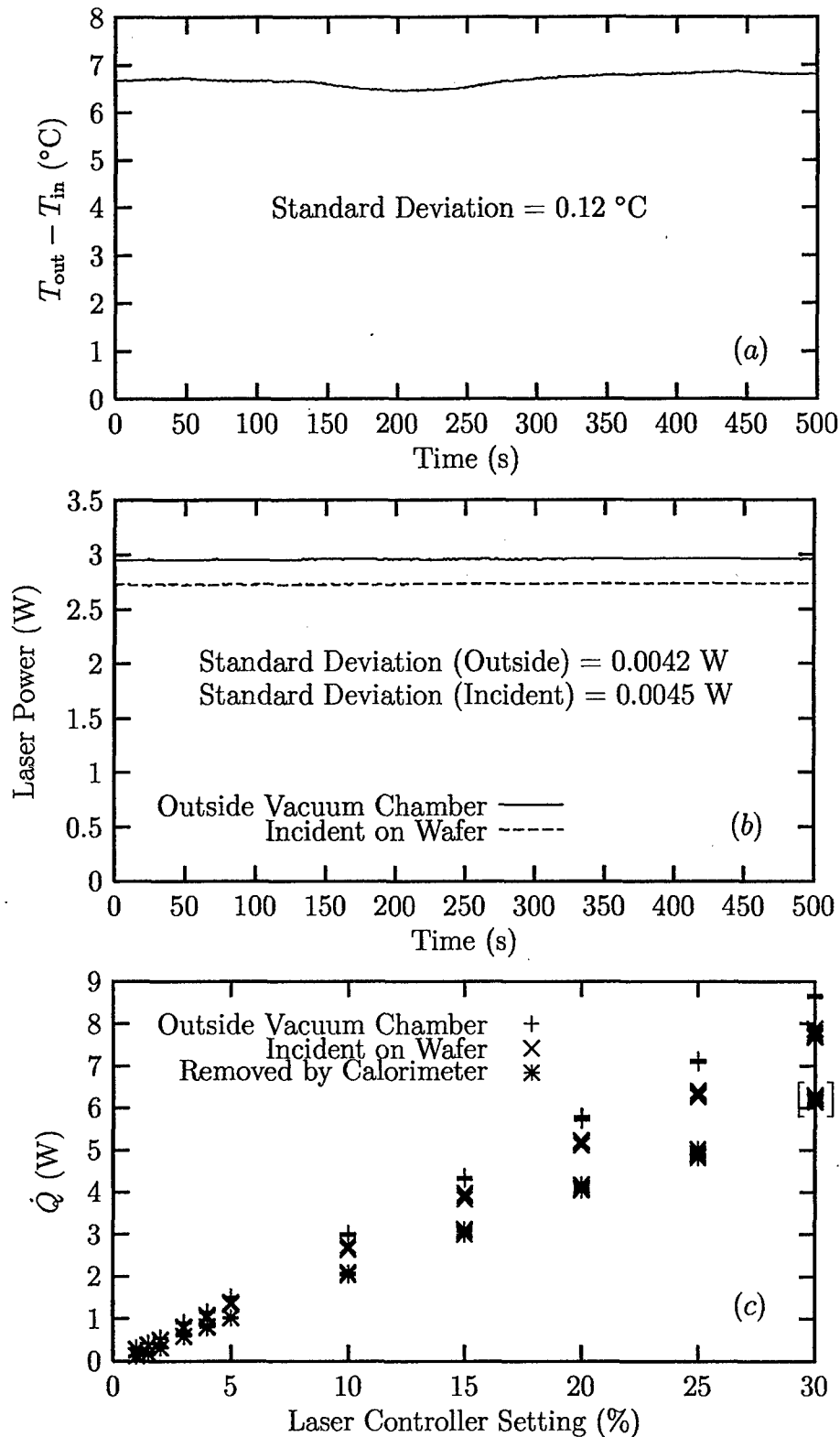


Figure 44: CO₂ laser calibration: (a) Typical calorimeter temperature increase trace (LCS = 10%); (b) Typical laser power measurement traces (LCS = 10%); (c) Heat rates versus LCS (Data points in square brackets were taken when the borosilicate glass melted on the wafer).

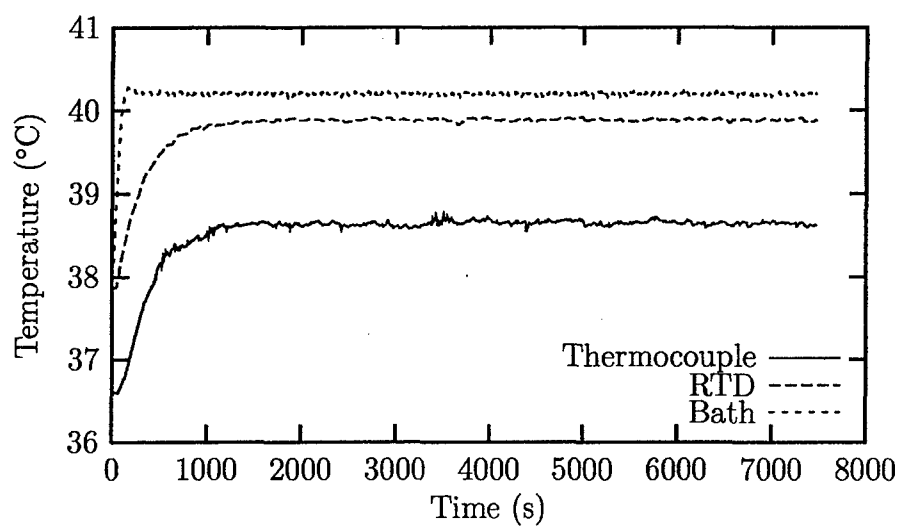


Figure 45: Temperature responses of a typical thermocouple, the resistance temperature detector, and the recirculating chiller bath.

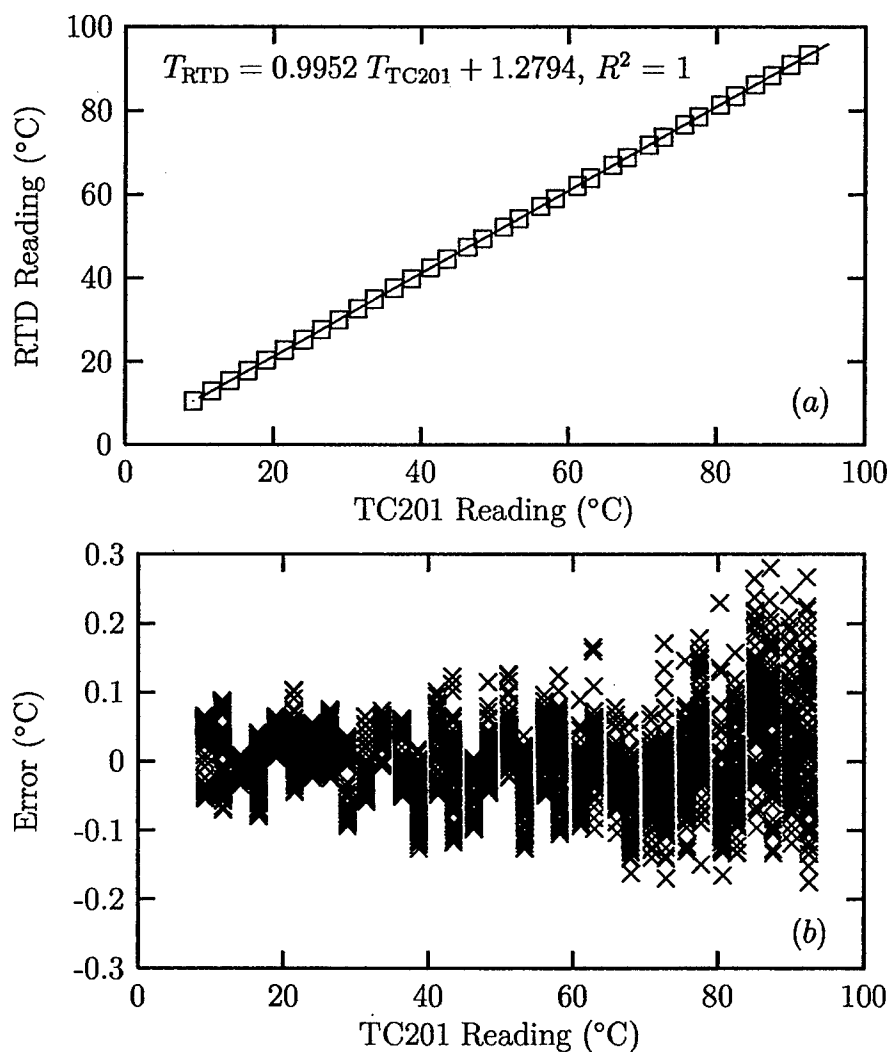


Figure 46: Temperature reading obtained during calibration (Thermocouple 201): (a) Temperature obtained by RTD vs. temperature reading from TC201; (b) Error obtained when substituting raw data into the linear best-fit equation for TC201.

5 Design and Testing of a Thermodynamic Filling Station for Miniature Heat Pipes

5.1 Abstract

An experimental investigation was conducted to determine the feasibility of a thermodynamic process to fill miniature heat pipes. A heat pipe filling station has been designed and constructed, which consists of a vacuum pump, pressure gauges, thermocouples, a manifold of valves, a large evacuated volume, and an environmental test chamber. A general filling procedure has been formulated. The filling station has been tested and preliminary results have been obtained using a heat pipe. The target range for the working fluid fill amount for the present project is 0.01 to $0.5\text{ g} \pm 10\%$. Preliminary results presented herein show that the current process is capable of filling miniature heat pipes with a mass of approximately 0.7 g with a repeatability of $\pm 12\%$. An analytical model that includes the effect of air within the fill station is presented. The analytical model overpredicts the experimental results by approximately 26% .

5.2 Introduction

Suitably filling a heat pipe with a working fluid is a critical process in ensuring proper performance. The steps involved in any filling process include thoroughly cleaning the heat pipe, evacuating the heat pipe to remove all non-condensable gases, dispensing the proper amount of high purity working fluid, and finally, sealing the heat pipe. Variations from the optimal charge can adversely affect the performance of the heat pipe (Castle et al., 2000).

The performance of the heat pipe is very sensitive to the quantity of working fluid charged. A small variation in the fill amount can degrade the heat pipe performance, possibly preventing it from functioning. Undercharging can cause several effects, one of the more serious being premature dry-out at the evaporator section due to an unsaturated wick structure. This dry-out can cause an increase in local temperature, resulting in failure of the component being cooled due to inadequate heat removal (Gao et al., 2000). It is common to spend a considerable amount of time calculating the amount of charge required, then deliberately overcharging by $10\text{-}20\%$ to prevent the possibility of undercharging (Peterson, 1994).

Overcharging the heat pipe will also reduce performance by partially blocking the condenser section due to the presence of a puddle of liquid.

There are several methods for filling heat pipes. However, few of these common practices are feasible for the 0.01 to 0.5 g fill quantities required for miniature heat pipes. One traditional method requires initially overfilling the heat pipe, heating it up to a desired operating temperature, venting off non-condensable gases, and then sealing the heat pipe once isothermal operation is attained. With miniature heat pipes, the fill quantities are too small and all the working fluid would probably be lost in this process.

Another method involves an evacuation and back-filling procedure (Castle et al., 2000). The heat pipe is attached to the heat pipe fill station, and both are then evacuated. The working fluid is then degassed using a freeze-thaw cycle or by boiling. Finally, the desired amount of working fluid is drawn into the heat pipe via a dispensing burette, and the heat pipe is sealed. The estimated uncertainties are well over 50% for this process applied to the small fill quantities of miniature heat pipes. The fill range for this process as tested by Castle et al. was $1.47 \text{ to } 4.38 \text{ g} \pm 5\%$.

Gao et al. (2000) developed three different methods for filling miniature heat pipes. The first process proposed was a micro syringe method similar to the evacuation/back-filling procedure mentioned above. This method requires a micro syringe, a T-junction, and a vacuum pump. The syringe is filled with working fluid. The filling needle is then replaced with a new dry needle. The syringe and heat pipe are connected to the T-junction and the vacuum system. The heat pipe is then evacuated. Lastly, the syringe plunger is depressed, displacing all working fluid into the heat pipe. The main drawback of this process is that a certain amount of air inevitably enters the heat pipe.

The second and third methods are quite similar in theory and process. The thermodynamic equilibrium and capillary tubing method both include a vacuum system, working fluid source, and either a vacuum chamber (thermodynamic) or capillary tubing (capillary). The process starts by evacuating the system and all components. Next, the heat pipe is completely filled with working fluid and then attached to the filling station. A valve is opened and the heat pipe is exposed to the chamber/tubing, which results in the evaporation of some of the working fluid. A sudden drop in temperature occurs due to the evaporation

process. The pressure then rises and an equilibrium point is achieved with the ambient. The amount of liquid evaporated is determined by the chamber/tubing volume. In the capillary tubing method, the liquid removal is aided by pushing the extra liquid into the capillary tubing, but not by flashing. Fill ranges for the chamber process were given for two chambers sizes: Chamber 1 (1850 ml) 0.080 to 0.117 g (−16.8 to 21.0%); Chamber 2 (500 ml) 0.132 to 0.165 g (−11.1 to 11.2%).

The thermodynamic method mentioned by Gao et al. (2000) is very similar to the process chosen and implemented in the present research and experimentation. The objectives of the present experiment are to reduce the minimum fill amount beyond that given by Gao et al. by an order of magnitude (while maintaining an uncertainty of approximately 10%), and to compare the results of the present experiment with an analytical model of the thermodynamic process.

5.3 Analytical Model

The current heat pipe fill station is shown in Fig. 47(a), which can be divided into three volumes for analysis. The vacuum chamber volume extends to valves V1 and V2, and includes the tubing for the dial pressure gage, the thermocouple pressure gage, and the thermocouple probe. The manifold volume includes tubing from valves V2 and V3, the critical orifice, and the tubing and fittings up to the point at which the heat pipe is attached. The heat pipe volume includes the heat pipe envelope and the fill tube. During the filling process, the heat pipe is charged with liquid and attached to the fill station. The vacuum chamber is evacuated, but the manifold and heat pipe are at atmospheric pressure. Valve V2 is then opened, exposing the liquid in the heat pipe to the vacuum chamber. After a portion of the liquid evaporates, the system reaches a steady state condition. At this point, the heat pipe fill tube is sealed. The objective of this analysis is to determine the amount of liquid in the heat pipe at the final state by accounting for the presence of air within the system.

The mass of air initially within the vacuum chamber is given by the perfect gas relation.

$$m_{a,vc} = \frac{P_{vc,1}V_{vc}}{R_a T_1} \quad (121)$$

The initial pressure within the manifold is atmospheric since it is open to ambient conditions when the heat pipe is attached to the fill station. The mass of air within the manifold is

$$m_{a,m} = \frac{P_{atm} V_m}{R_a T_1} \quad (122)$$

In general, the heat pipe volume at the initial state is taken up by the working fluid (liquid and vapor) at saturated conditions, which is in equilibrium with any air that may be present within the heat pipe. The mass of air within the heat pipe is dependent upon the method used for introducing the initial liquid charge. If the liquid is installed using a syringe, for instance, the amount of air is unknown. Therefore, the mass of air originally in the heat pipe will be varied from zero to the maximum value possible to determine the effect on the final conditions within the fill station. The maximum mass of air possible within the heat pipe can be determined by assuming that no vapor is present

$$m_{a,hp,max} = \frac{P_{atm} (V_{hp} - V_{l,1})}{R_a T_1} \quad (123)$$

where the volume of the liquid is based on the initial amount metered into the heat pipe.

$$V_{l,1} = m_{l,1} v_f \quad (124)$$

The total mass of air within the system is

$$m_{a,t} = m_{a,vc} + m_{a,m} + m_{a,hp} \quad (125)$$

After the heat pipe is connected to the fill station, valve V2 is opened and the evaporation process begins. It is assumed that the evaporation of the working fluid sweeps all of the air out of the heat pipe and into the manifold and vacuum chamber volumes. It is also assumed that the wick structure and the vertical orientation of the heat pipe prevent liquid droplets from being ejected from the heat pipe when it is mounted to the fill station. Finally, it is assumed that temperature for State 2 is equal to the initial temperature (prior to opening the valve V2). The final pressure in the system is the partial pressure of the working fluid at the ambient temperature. The final volume of air is

$$V_{a,2} = \frac{m_{a,t} R_a T_1}{P_{v,2}} \quad (126)$$

The volume occupied by the working fluid is

$$V_{wf,2} = V_t - V_{a,2} \quad (127)$$

Using the definition of quality, the mass of working fluid in the vapor state is

$$m_{v,2} = \frac{V_{wf,2} - m_{l,1}v_f}{v_{fg}} \quad (128)$$

The mass of working fluid in the liquid state is determined using the continuity equation.

$$m_{l,2} = m_{l,1} - m_{v,2} = m_{l,1} - \left(\frac{V_{wf,2} - m_{l,1}v_f}{v_{fg}} \right) \quad (129)$$

5.4 Experimental Setup

The current filling station is shown schematically in Fig. 47(a) and Fig. 48. The station consists of an aluminum vacuum chamber, a stainless steel manifold of valves and interconnecting tubing, a critical orifice plate and a mechanical vacuum pump. Initially, the open heat pipe container is charged with liquid working fluid, which is measured using a precision scale (Ohaus Explorer Model E01140). The heat pipe is then attached to the filling station as shown in Fig. 47(a). The vacuum chamber is evacuated and subsequently isolated from the vacuum pump. Valve V2 is then opened to expose the working fluid in the heat pipe to the reduced pressure within the vacuum chamber. This initiates evaporation of the liquid working fluid, which halts when the system reaches a steady state condition with the ambient. The ambient temperature is controlled by placing the entire filling station into an environmental chamber (Thermotron, $\Delta T_\infty \simeq 1.0^\circ\text{C}$). Temperatures within the vacuum chamber and on the surface of the heat pipe were measured using Type T thermocouples and a data acquisition system (Fluke 2286A Data Logging System). The pressure within the vacuum chamber was tracked using a thermocouple vacuum gauge and reader (Varian Model 0531 and Model 804-A) and a dial absolute pressure gauge (Wallace and Tiernan). A mechanical vacuum pump (Duo Seal Model 1397) was employed to evacuate the system.

As the preliminary testing of the system progressed, it was found that a device was needed to control the flow of working fluid from the heat pipe to the vacuum chamber. When the valve V2 is initially opened, a portion of the liquid could flash off into the vacuum chamber, which could result in a slug of liquid being ejected from the heat pipe container. A critical

orifice design was implemented to slow the evaporation process by restricting the maximum mass flow rate of the vapor from the heat pipe. The cross-sectional area of the hole in the orifice plate was calculated using the following expression, which is based on the assumption that the flow is choked at the throat.

$$A^* = \dot{m} \left[P_0 \sqrt{\frac{k}{R_v T_0}} \left(\frac{2}{k+1} \right)^{\left(\frac{k+1}{2(k-1)} \right)} \right]^{-1} \quad (130)$$

Once the area was known, the orifice plate was constructed using copper plate and placed in between two flanges (Fig. 49(a)). Three orifice plates were made with three different orifice diameters for experimentation: $D_o = 0.203$ mm (0.008 in.), 0.381 mm (0.015 in.) and 0.762 mm (0.0300 in.). A photograph of the orifice plate installed in the filling station is shown in Fig. 49(b).

It was necessary to accurately determine all of the volumes of the fill station, which included all of the components, the chamber, and the heat pipe, for the calculations made in the mathematical model. All volumes were found either by calculations or by given values in the manufacturer manuals. Since all of the volumes were cylindrical, the uncertainty of the volume ΔV was found by using the root-sum-square method

$$\Delta V = \sqrt{\left(\frac{\partial V}{\partial r} \Delta r \right)^2 + \left(\frac{\partial V}{\partial h} \Delta h \right)^2} \quad (131)$$

$$= \sqrt{(2\pi r h \Delta r)^2 + (\pi r^2 \Delta h)^2} \quad (132)$$

where the uncertainties of the measured values, Δr and Δh , were comprised of the readability or the uncertainty of the measurement tool. The dial caliper used had a readability of 0.0254 mm (0.001 in.), and a readability per measurement of 0.0254 mm (0.001 in.). The scale used had a readability of 0.396 mm (1/64 in.) and a readability of 0.793 mm (2/64 in) per measurement. The measured values for all of the components and the total volumes are given in Table 13.

5.5 Results and Discussion

Results of preliminary tests are shown in Fig. 50, where the experimental data are compared to the analytical model. While the model significantly over-predicts the experimental

data (approximately 26%), the model matches the slope of the linear best-fit curve for the experimental data fairly well. The curve labelled "Analytical, No Air" shows the results when no air is present in the system; i.e., the vacuum chamber, manifold and heat pipe are completely evacuated. Under this condition, the amount of liquid left in the heat pipe is less than with air present, as expected. It was determined that assuming the heat pipe did not contain any air at the start of the process had a negligible effect on the results. The data points presented fit the linear curve to within $\pm 12\%$, but more data points are needed to fully evaluate the repeatability of the system.

5.6 Conclusions and Future Directions

Initial testing of the heat pipe filling station has verified the viability of the thermodynamic process. Inconsistencies between the analytical model and the experimental data will require further investigations into methods of improving the agreement. In order to reduce the amount of air within the system, a combined filling station is proposed as shown in Fig. 47(b), where a conventional back-filling station is attached to the current thermodynamic filling station. The merits and drawbacks of this combined station still need to be evaluated.

5.7 References

Castle, R., Thomas, S., and Yerkes, K., 2000, "The Effect of Working Fluid Inventory on the Performance of Revolving Helically-Grooved Heat Pipes," *ASME Journal of Heat Transfer*, Vol. 123, pp. 120-129.

Cengel, Y., and Boles, M., 2002, *Thermodynamics: An Engineering Approach*, 4th Edn., McGraw-Hill, Boston.

Gao, M., and Cao, Y., Jones, K., and Zampino, M., 2000, "Ceramic Miniature Heat Pipes and Liquid Charging Methods," *Proceedings of the ASME National Heat Transfer Division-2000* Vol. 4. pgs. 429-434.

Miller, R., 1989, *Flow Measurement Engineering Handbook*, 2nd Edn., McGraw-Hill, New York.

Peterson, G., 1994, *An Introduction to Heat Pipes: Modeling, Testing and Applications*, Wiley.

5.8 Nomenclature

A^*	cross-sectional area of the critical orifice throat, m^2
h	cylinder height, m
k	ratio of specific heats
$m_{a, hp}$	mass of air in the heat pipe, kg
$m_{a, hp, max}$	maximum possible mass of air in the heat pipe, kg
$m_{a, m}$	mass of air in the manifold, kg
$m_{a, t}$	total mass of air in the filling station, kg
$m_{a, vc}$	mass of air in the vacuum chamber, kg
$m_{l, 1}$	initial mass of liquid working fluid in the heat pipe, kg
$m_{l, 2}$	mass of saturated working fluid liquid in the heat pipe at State 2, kg
$m_{v, 2}$	mass of saturated working fluid vapor in the filling station at State 2, kg
\dot{m}	mass flow rate, kg/s
P_{atm}	atmospheric pressure, Pa
$P_{v, 2}$	partial pressure of the saturated working fluid vapor at State 2, Pa
$P_{vc, 1}$	air pressure in the vacuum chamber at State 1, Pa
P_0	stagnation pressure, Pa
r	cylinder radius, m
R_a	particular gas constant of air, $J/(kg \cdot K)$
T_0	stagnation temperature, K
T_1	initial system temperature, K
v_f	specific volume of saturated liquid, m^3/kg
v_{fg}	$v_g - v_f$, m^3/kg
v_g	specific volume of saturated vapor, m^3/kg
V	volume, m^3
$V_{a, 2}$	volume of air at State 2, m^3
V_{hp}	heat pipe volume, m^3
$V_{l, 1}$	initial volume of liquid working fluid in the heat pipe, m^3
V_m	manifold volume, m^3

V_t	total volume of the filling station and heat pipe, m ³
V_{vc}	vacuum chamber volume, m ³
$V_{wf,2}$	volume occupied by the working fluid at State 2, m ³
Δh	uncertainty in measured height, m
Δr	uncertainty in measured radius, m
ΔV	uncertainty in measured volume, m

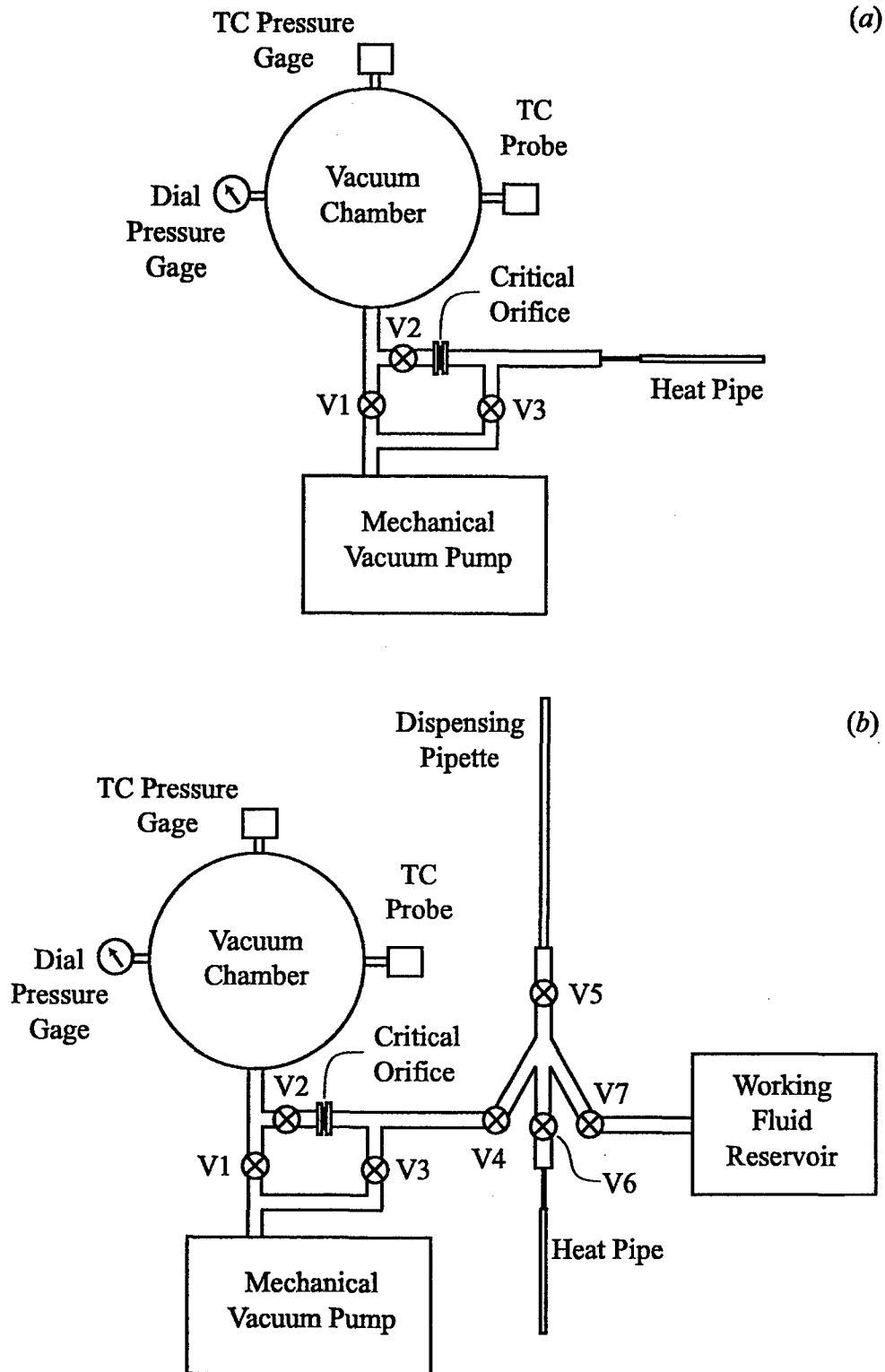


Figure 47: Schematic of the heat pipe filling station: (a) Current system; (b) System incorporating a standard filling station.

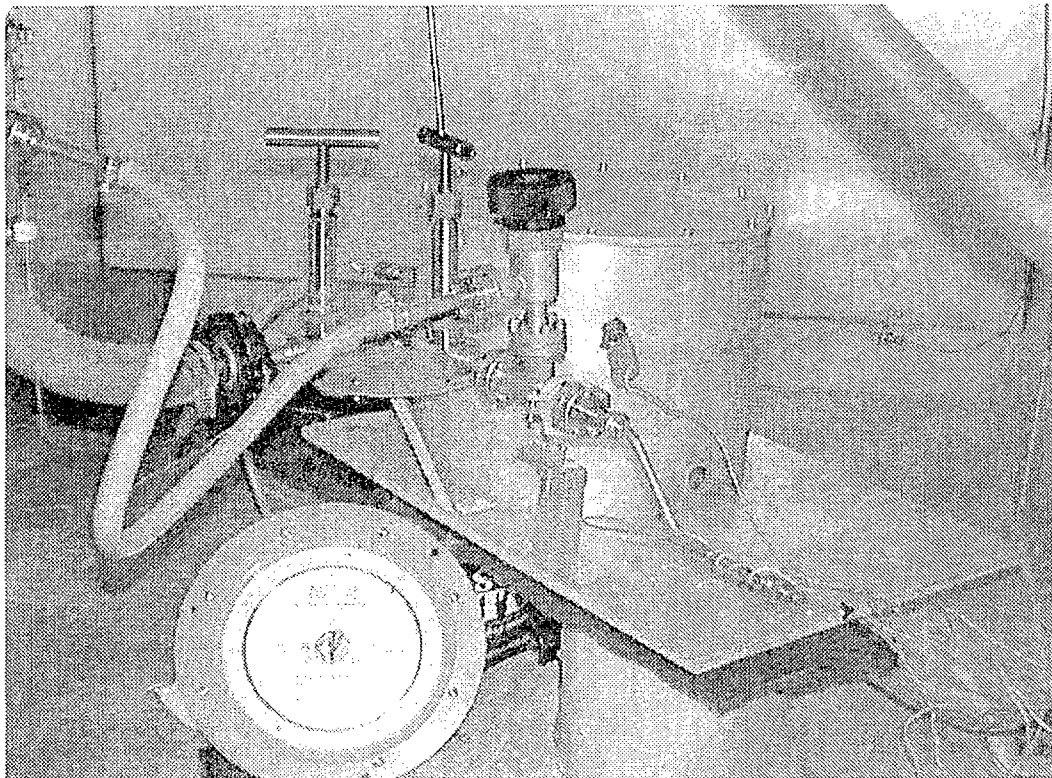


Figure 48: Thermodynamic heat pipe filling station.

BEST AVAILABLE COPY

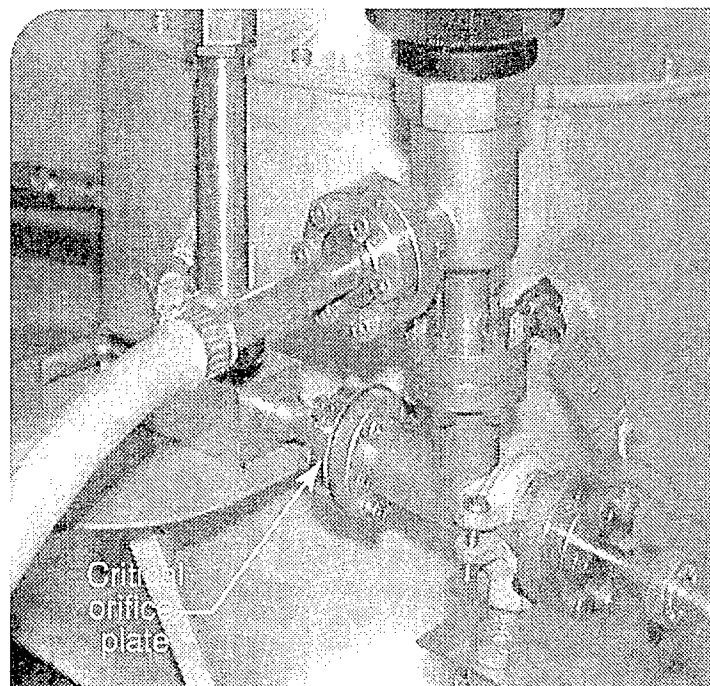
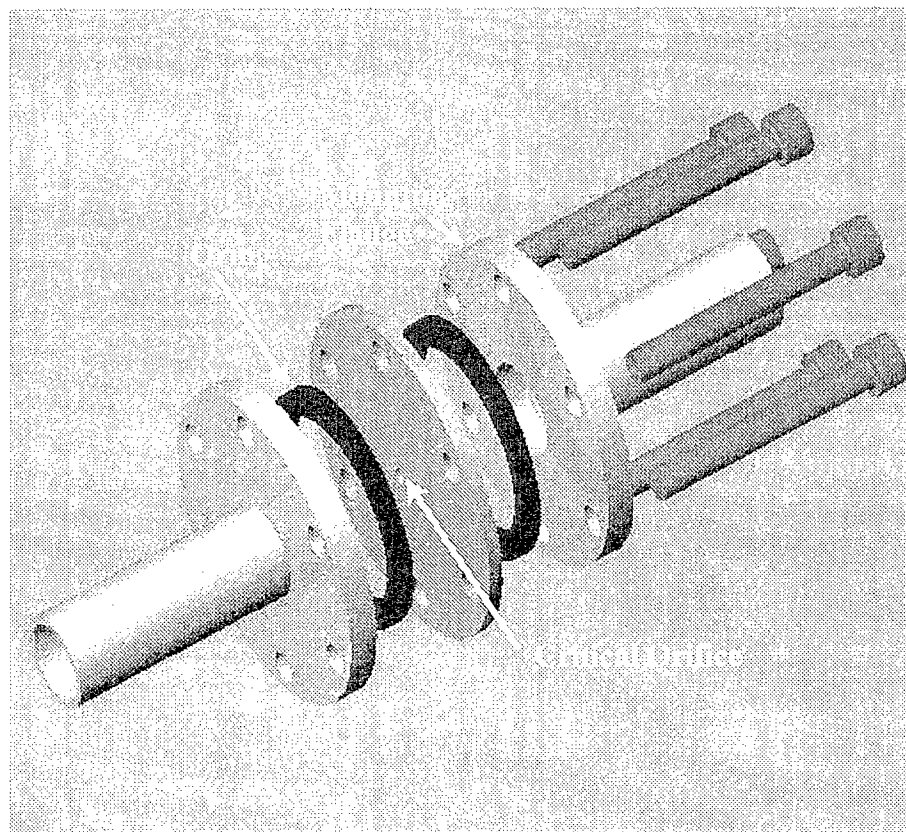


Figure 49: Critical orifice plate: (a) Internal design; (b) Installation in the filling station.

BEST AVAILABLE COPY

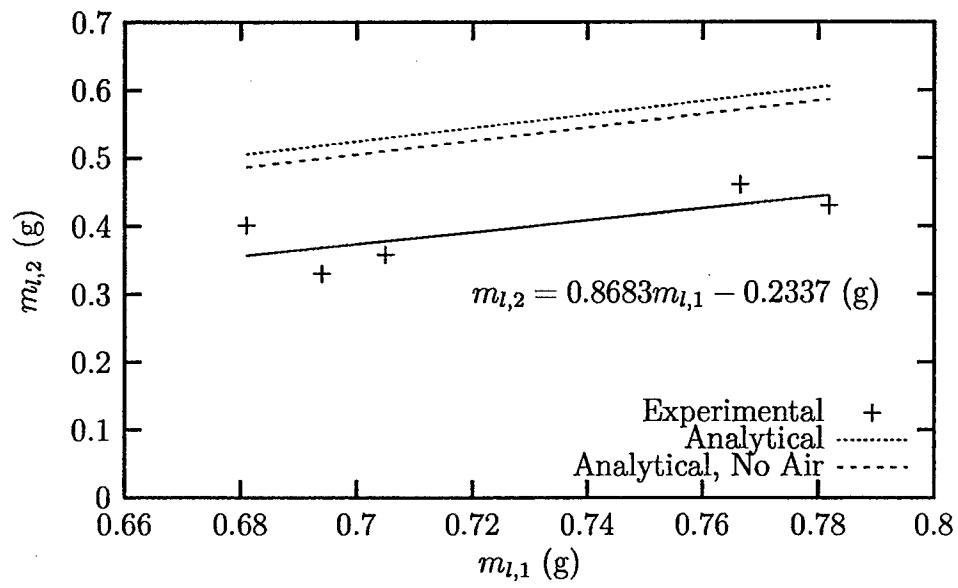


Figure 50: Mass of liquid in the heat pipe at State 2 versus initial liquid charge ($m_{a,hp} = 0$, $P_{vc,1} = 30 \text{ mTorr}$, $T_1 = 25^\circ\text{C}$, $P_{atm} = 10^5 \text{ Pa}$).

6 Acceleration Testing of Three Raytheon Heat Pipes using the AFRL/PRPS Centrifuge Table

6.1 Abstract

The purpose of this experiment was to determine the effect of adverse longitudinal acceleration on the operation of three heat pipes provided by Raytheon. The heat pipe assembly (as delivered) was mounted to a centrifuge table such that the evaporator sections were closer to the center of the table than the condenser sections, which resulted in an adverse acceleration condition. The start-up test is described as follows: Rotate the centrifuge table for five min. at the prescribed acceleration level (5-g or 10-g), stop the rotation, wait for 5 s, then apply a fixed power input to the evaporator. The burst test consists of the following: Apply a fixed power input to the evaporator, allow the heat pipe to reach steady-state operation, rotate the centrifuge table at the prescribed acceleration level (5-g or 10-g) for 5 s, then stop the rotation. During the start-up tests, it was found that the 3-inch and 6-inch heat pipes (3IHP and 6IHP) were not affected, but the 9-inch heat pipe (9IHP) showed signs of a deprime condition. The burst tests resulted in the 3IHP and 9IHP becoming deprimed to a significant degree. The response time of the 9IHP to the initial start-up was significantly longer than the other heat pipes.

6.2 Experimental Setup

The heat pipe experiments were carried out on an eight-foot diameter horizontal centrifuge table at Wright-Patterson Air Force Base (AFRL/PRPS). This table was driven by a 20-hp DC motor (General Electric) and was controlled remotely for safety. A data acquisition unit (Keithley Model 500A) with a personal computer running data logging software (Viewdac) was used to collect temperature and acceleration profiles. The heat pipe assembly was attached to the centrifuge table as shown in Figs. 51 and 52. An accelerometer (Columbia Research Laboratories Model SA-307IIPTX) was used to measure the acceleration at the lengthwise center of the heat pipes. Temperature signals were conditioned and amplified on the centrifuge table. These signals were transferred off the table through the instrumentation slip ring assembly, which was completely separate from the power slip ring

Name	r (in)	h (in)	V (in ³)	ΔV (in ³)	Percent Error
Large Cylinder	4.516	8.031	514.6	7.4	1.4
Cylinder Weld	4.516	0.312	-1.385	0.013	0.94
Hole	0.233	0.300	0.051	0.0005	0.98
Hole	0.213	0.150	0.021	0.0002	0.95
Hole	0.200	0.285	0.036	0.0004	1.1
Hole	0.218	0.160	0.024	0.0003	1.2
Hole	0.225	0.145	0.023	0.0003	1.3
Hole	0.183	0.170	0.018	0.0002	1.1
Hole	0.168	0.340	0.030	0.0004	1.3
Stainless Tubing	0.125	1.375	0.068	0.0019	2.8
Stainless Tubing	0.125	3.25	0.160	0.003	1.9
Dial Gauge Tubing	0.063	21.0	0.258	0.0083	3.2
Male Extension	0.093	1.325	0.036	0.0011	3.1
TC Vacuum Gauge	0.132	2.00	0.110	0.0024	2.2
TC Probe Fitting	0.125	0.250	0.012	0.0015	12
Reducing Bushing	0.140	0.188	0.012	0.0019	16
Swagelok	0.125	0.50	0.025	0.0016	6.4
Swagelok to Pipe	0.125	1.00	0.049	0.0017	3.5
Bellows Valve	N/A	N/A	0.153	0.0015	0.98
Stainless Tubing	0.125	1.50	0.074	0.0019	2.6
O-ring Fitting	0.093	0.375	0.010	0.0009	9.0
Mini T Jcn	0.313	3.00	0.920	0.0113	1.2
Mini T Jcn	0.313	1.125	0.345	0.0098	2.8
Varian Valve	0.188	1.50	0.166	0.0039	2.3
Bellows Valve	N/A	N/A	0.076	0.0015	2.0
Heat Pipe	N/A	N/A	0.047	0.001	2.1

Table 13: Heat pipe filling station volume data ($V_{vc} = 514.3 \text{ in}^3 = 8.428 \times 10^{-3} \text{ m}^3$, $V_m = 1.591 \text{ in}^3 = 2.607 \times 10^{-5} \text{ m}^3$, $V_{hp} = 0.047 \text{ in}^3 = 7.702 \times 10^{-7} \text{ m}^3$, $V_t = 8.455 \times 10^{-3} \text{ m}^3$).

assembly to reduce electronic noise. Conditioning the temperature signals on the centrifuge table eliminated difficulties associated with creating additional junctions within the slip ring assembly.

Power was supplied to the heat pipe evaporator section by a precision power supply (Kepco Model ATE 150-7M) through power slip rings to the table. The input power was calculated using the current and voltage readings. While the current reading could be made directly using a precision ammeter, the voltage across the electric heater had to be measured on the rotating table because voltage drops were noted between the control room and the table, regardless of the size of wire used. Therefore, the voltage at the heater was obtained through the instrumentation slip ring assembly and measured by a precision voltmeter (Hewlett Packard Model 3478A).

6.3 Experimental Procedure

Two separate procedures were developed to examine the performance of the heat pipes under adverse acceleration conditions. The start-up test and the burst test are discussed in this section. In all of the experiments, the table was allowed to rotate slowly to prevent damage to the instrumentation and power slip rings. This baseline rotational speed was $\omega = 0.0329$ rad/s, which imposed a radial acceleration of $a_r = 1.24 \times 10^{-4}$ -g. While a baseplate heater was present on the heat pipe assembly, it was not used during these tests. In addition to recording the temperatures and accelerations to computer data files continuously during the test, the temperature, acceleration, and heater power information (voltage and current) were recorded into a logbook at intervals during the testing. For all tests, the electrical power input to the evaporator heater was approximately 17 W. To prevent damage to the heater mounted to the heat pipe evaporator section, a maximum evaporator temperature of 115°C was imposed. Each test was run three times to evaluate the repeatability of the experimental procedure.

Burst test procedure

1. Turn on the data logging software to record baseline readings.
2. Turn on the power to the heater.

3. Allow the heat pipe to reach steady-state operation.
4. After about 25 min. of steady-state operation, bring the table rapidly to the desired radial acceleration by increasing the rotational speed.
5. Hold this acceleration for 5 s.
6. Rapidly decelerate the table back to the baseline rotational speed.
7. Monitor the temperatures in case of evaporator dry-out.
8. If the pipe returns to steady-state operation, record data for about 20 min.
9. Repeat steps 4 through 7, using the same acceleration.
10. If the heat pipe returns to steady-state operation after the second burst, record data for about 20 min.
11. Shut off the heater power.
12. Record the cool down process for several minutes.
13. Turn off the data acquisition software and download the data files.

Start-up test procedure

1. Start the data logging software to record baseline data.
2. Increase the rotational speed of the table to reach the desired radial acceleration. Allow the table to rotate at this speed for 5 min.
3. Bring the table rapidly back down to its baseline speed.
4. Wait 5 s and then turn on the evaporator heater.
5. Allow the heat pipe to reach steady-state operation.
6. Run the heat pipe at steady-state condition for about 30 min.
7. Turn off the power to the heater.

8. Record the cool down process for several minutes.
9. Stop the data logging software and download the data files.

For each test, plots were generated of temperature vs. time and radial acceleration vs. time.

6.4 Results and Discussion

Three heat pipes have been tested to determine their thermal performance characteristics when subjected to adverse acceleration conditions. The heat pipe assembly was mounted to a centrifuge table at AFRL/PRPS to impose a radial acceleration along the axial direction of the heat pipes. Included in this section are typical temperature-time traces, steady-state measurements of the temperature difference between the evaporator and middle (adiabatic) thermocouples, and initial start-up times, both for stationary start-ups and start-ups following long periods of acceleration.

Figure 53 presents typical temperature-time traces during a 5-g start-up test. All three heat pipes reached the steady state in a relatively short time. This steady-state condition was maintained for approximately 30 min., and then the heater power was turned off. For the 3IHP and 6IHP, the temperature difference between the evaporator and adiabatic sections (ΔT_{ea}) was lower than that for the 9IHP. This temperature difference was chosen as an indicator of wick priming based on previous experience with heat pipes ([1]–[8]). The evaporator-adiabatic temperature differences for all of the start-up tests are shown in Fig. 54, where ΔT_{ea} was significantly higher and more scattered for the 9IHP. Both of these points indicate that the wick was poorly primed prior to start-up for the 9IHP.

Figure 55 shows the results for four burst tests. In Fig. 55(a), the 3IHP was allowed to reach a steady-state condition while the centrifuge table was rotating at its baseline speed. At approximately $t = 2500$ s, the rotational speed was increased such that $a_r = 5.0$ -g for 5 s, and then the speed was reduced to the baseline. While the adiabatic and condenser temperatures remained fairly constant, the evaporator temperature increased significantly, indicating a partial dry-out event. The heat pipe was again allowed to reach another steady-state condition, and another burst test was carried out at approximately $t = 4500$ s. The

evaporator temperature increased further, and the power to the heater was shut off due to a run-away dry-out situation.

Figures 55(b) and 55(c) compare two burst tests for the 6IHP. Of particular interest is the initial start-up period shown in Fig. 55(b), where a wick priming event occurred at approximately $t = 600$ s. In this event, the temperature difference between the evaporator and adiabatic sections was initially high ($\Delta T_{ea} \simeq 23^\circ\text{C}$). After the wick primed, the adiabatic temperature increased dramatically, which decreased the temperature difference to $\Delta T_{ea} \simeq 11^\circ\text{C}$. Two burst tests were carried out in Fig. 55(b) at $t = 2500$ and 4000 s, and the 6IHP did not deprime in either case. In Fig. 55(c), the wick did not prime during start-up, and the temperature difference remained at $\Delta T_{ea} \simeq 22^\circ\text{C}$ prior to the acceleration burst. Again, two burst tests were performed ($t = 2500$ and 4500 s). In each of these tests, the temperature difference actually decreased slightly, showing that the heat pipe wick structure was partially primed by the acceleration burst.

Figure 55(d) shows the performance of the 9IHP during a burst test with bursts at $t = 2500$ and 4000 s. Initially, the heat pipe was primed with a very low temperature difference ($\Delta T_{ea} \simeq 7^\circ\text{C}$). After the first burst test, the adiabatic temperature decreased significantly which resulted in $\Delta T_{ea} \simeq 25^\circ\text{C}$. The second burst test resulted in a run-away dry-out situation, so the test was halted.

Figure 56 shows the steady-state data for all of the burst tests, except for the run-away dry-out situations, since steady-state data could not be collected. This test had a detrimental impact on the wick priming for the 3IHP and the 9IHP, where ΔT_{ea} increased after the burst test. The 6IHP was less sensitive to the burst-test conditions in comparison to the other heat pipes.

The response times of the heat pipes to the initial application of the heat load are displayed in Fig. 57. These times were calculated using the 63% time-constant method, where the time constant is defined as the time required for the evaporator temperature to reach 63% of its steady-state value. These data include the initial start-up responses for both the start-up tests and the burst tests, where the power to the evaporator is first energized. The responses due to the actual burst tests (immediately after the radial acceleration was increased and then decreased) were not included due to difficulties in defining an appropriate

time constant. The time constants for all three heat pipes were very repeatable, with the time constant for the 9IHP being more than twice as long as those of the other heat pipes.

It is believed that the 3IHP was not properly charged based on the following observations.

1. During the start-up tests, ΔT_{ea} was higher for the 3IHP than the 6IHP (Fig. 54).
2. For the burst tests, ΔT_{ea} for the 3IHP was greater than both the 6IHP and the 9IHP (Fig. 56).
3. The response time for the 3IHP (52 s) was higher than the 6IHP (44 s) (Fig. 57).

It was expected that the 3IHP would perform with a lower ΔT_{ea} and with a shorter response time than the 6IHP due to the shorter effective heat pipe length of the 3IHP.

6.5 Conclusions

Based on the experiments described above, the following conclusions have been made concerning the performance of the three heat pipes under adverse longitudinal acceleration conditions:

1. During the start-up tests, the 9IHP showed signs of a deprimed wick structure.
2. The burst tests caused the 3IHP and the 9IHP to become deprimed.
3. The start-up response time for the 9IHP was significantly higher than the other heat pipes (more than double).
4. The 3IHP may not have been properly charged with working fluid.

References

- [1] Castle, M., Thomas, S., and Yerkes, K., 2001, "The Effect of Working Fluid Inventory on the Performance of Revolving Helically-Grooved Heat Pipes," *ASME Journal of Heat Transfer*, Vol. 123, pp. 120-129.
- [2] Klasing, K., Thomas, S., and Yerkes, K., 1999, "Prediction of the Operating Limits of Revolving Helically-Grooved Heat Pipes," *ASME Journal of Heat Transfer*, Vol. 121, pp. 213-217.

- [3] Thomas, S., Klasing, K., and Yerkes, K., 1998, "The Effects of Transverse Acceleration-Induced Body Forces on the Capillary Limit of Helically-Grooved Heat Pipes," *ASME Journal of Heat Transfer*, Vol. 120, pp. 441-451.
- [4] Thomas, S., and Yerkes, K., 1997, "Quasi-Steady State Performance of a Heat Pipe Subjected to Transient Acceleration Loadings," *AIAA Journal of Thermophysics and Heat Transfer*, Vol. 11, pp. 306-309.
- [5] Klasing, K., Thomas, S., and Yerkes, K., 1997, "CAPLIM: A VISUAL BASIC Program to Calculate the Capillary Limit of an Axially-Grooved Heat Pipe," *Proceedings of the 32nd Intersociety Energy Conversion Engineering Conference*, Vol. 2, pp. 1514-1518, Honolulu, HI.
- [6] Wirsch, P., and Thomas, S., 1996, "Performance Characteristics of a Stainless Steel/Ammonia Loop Heat Pipe," *AIAA Journal of Thermophysics and Heat Transfer*, Vol. 10, pp. 326-333.
- [7] Faghri, A., Gogineni, S., and Thomas, S., 1993, "Vapor Flow Analysis of an Axially Rotating Heat Pipe," *International Journal of Heat and Mass Transfer*, Vol. 36, pp. 2293-2303.
- [8] Faghri, A., and Thomas, S., 1989, "Performance Characteristics of a Concentric Annular Heat Pipe: Part I—Experimental Prediction and Analysis of the Capillary Limit," *ASME Journal of Heat Transfer*, Vol. 111, pp. 844-850.

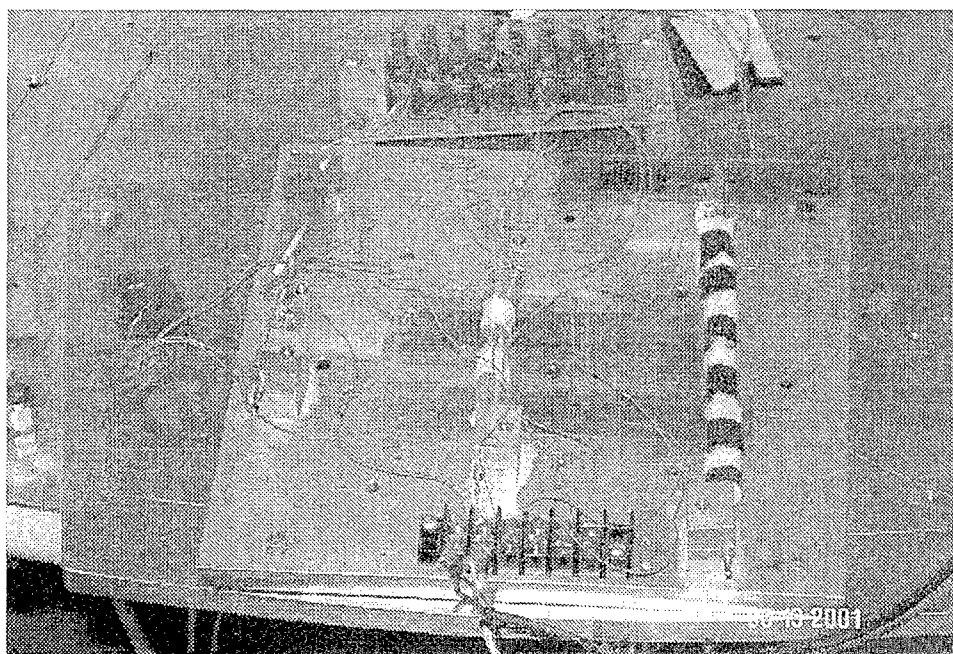


Figure 51: Close-up view of the heat pipe assembly mounted to the centrifuge table.

BEST AVAILABLE COPY

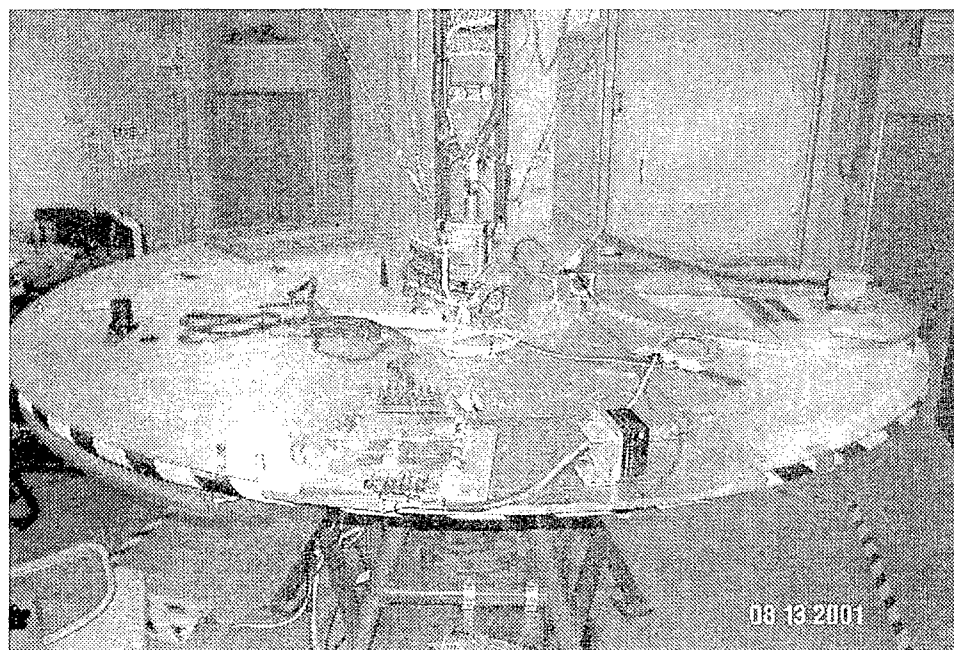
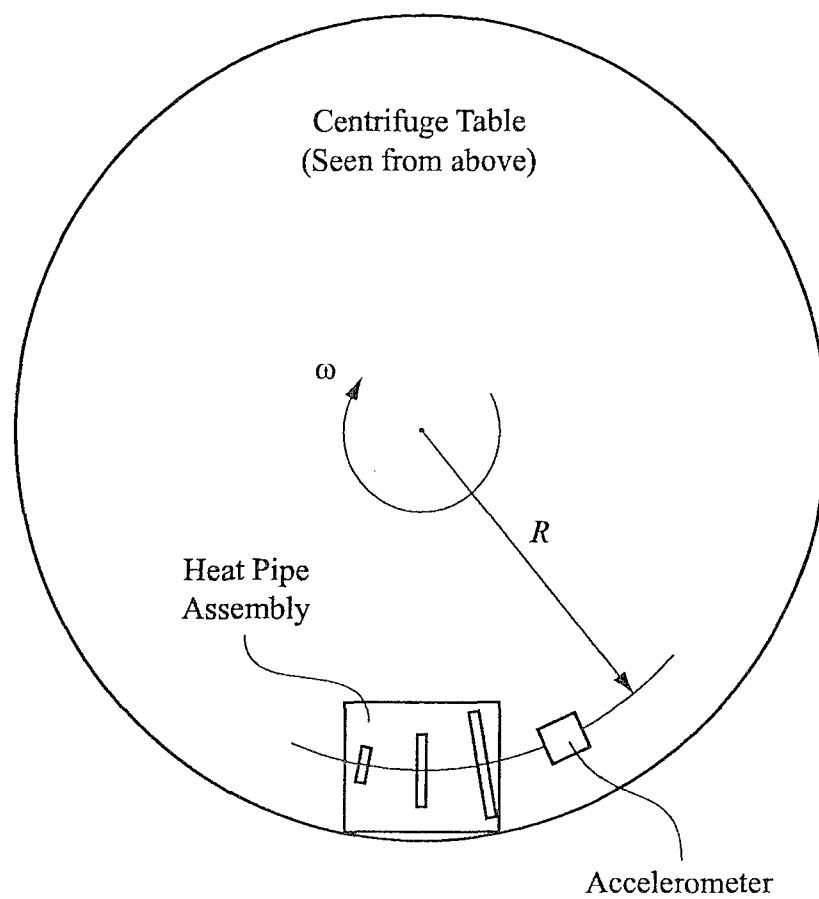


Figure 52: Placement of the heat pipe assembly on the centrifuge table ($R = 44.5$ inches).

BEST AVAILABLE COPY

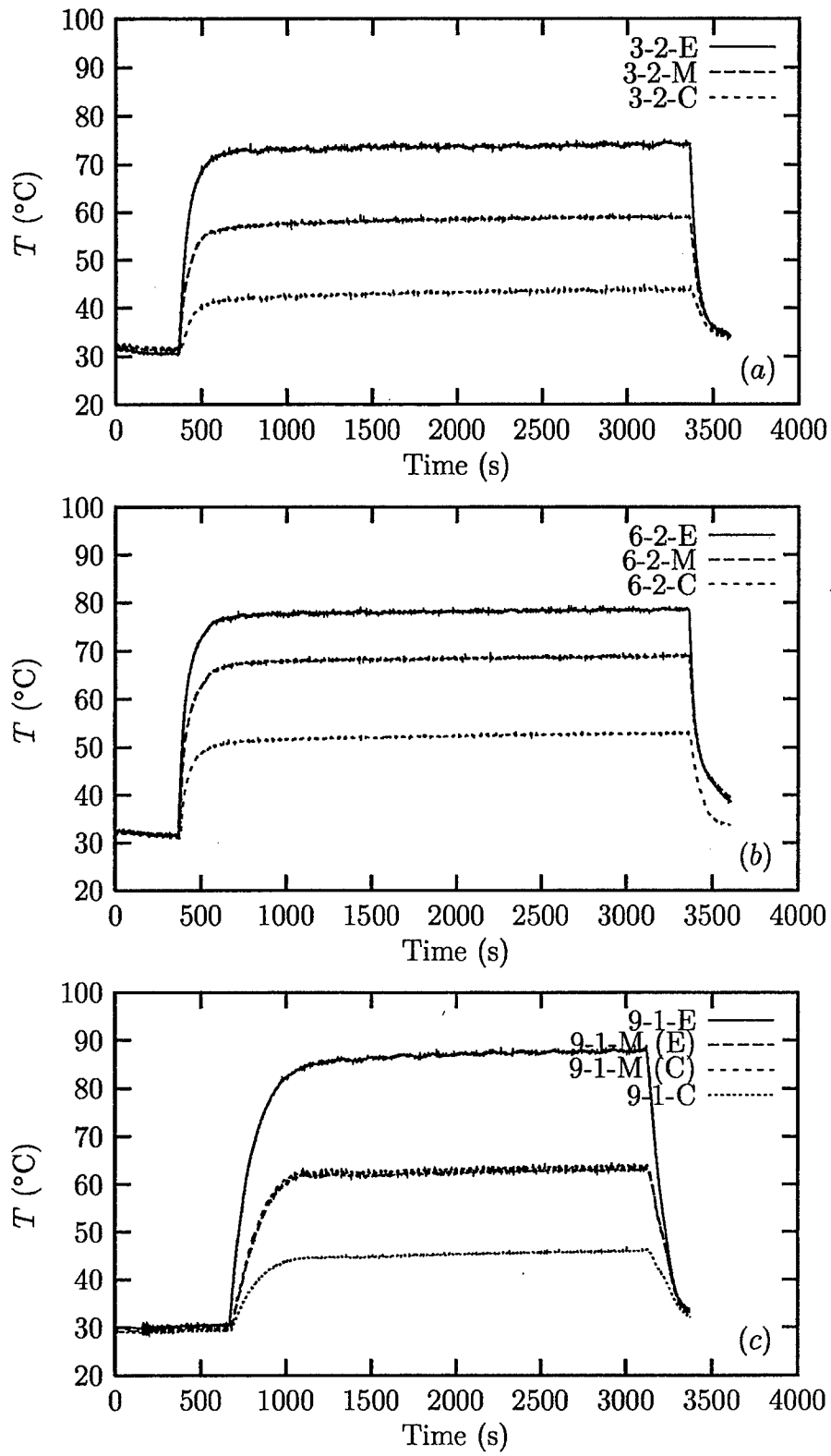


Figure 53: Typical start-up test results for $a_r = 5.0$ -g: (a) 3IHP (RAY33); (b) 6IHP (RAY22); (c) 9IHP (RAY9).

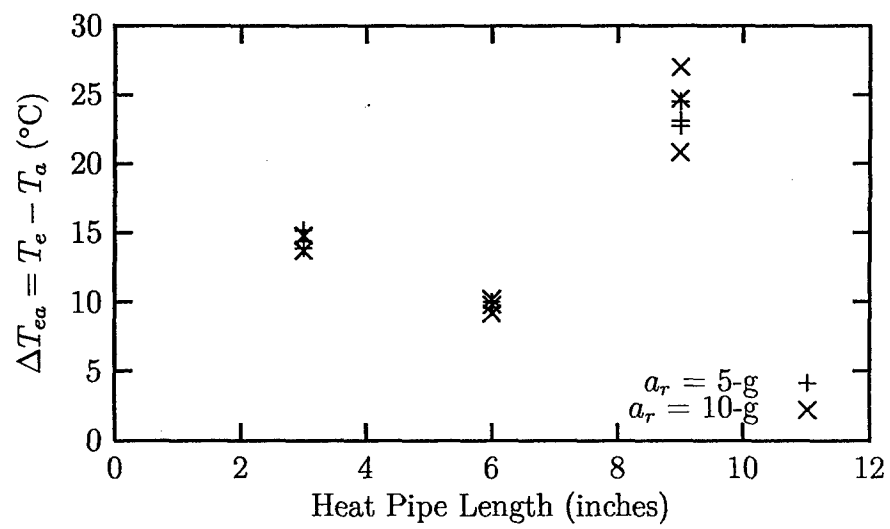


Figure 54: Temperature differences between the evaporator and adiabatic sections for the start-up tests.

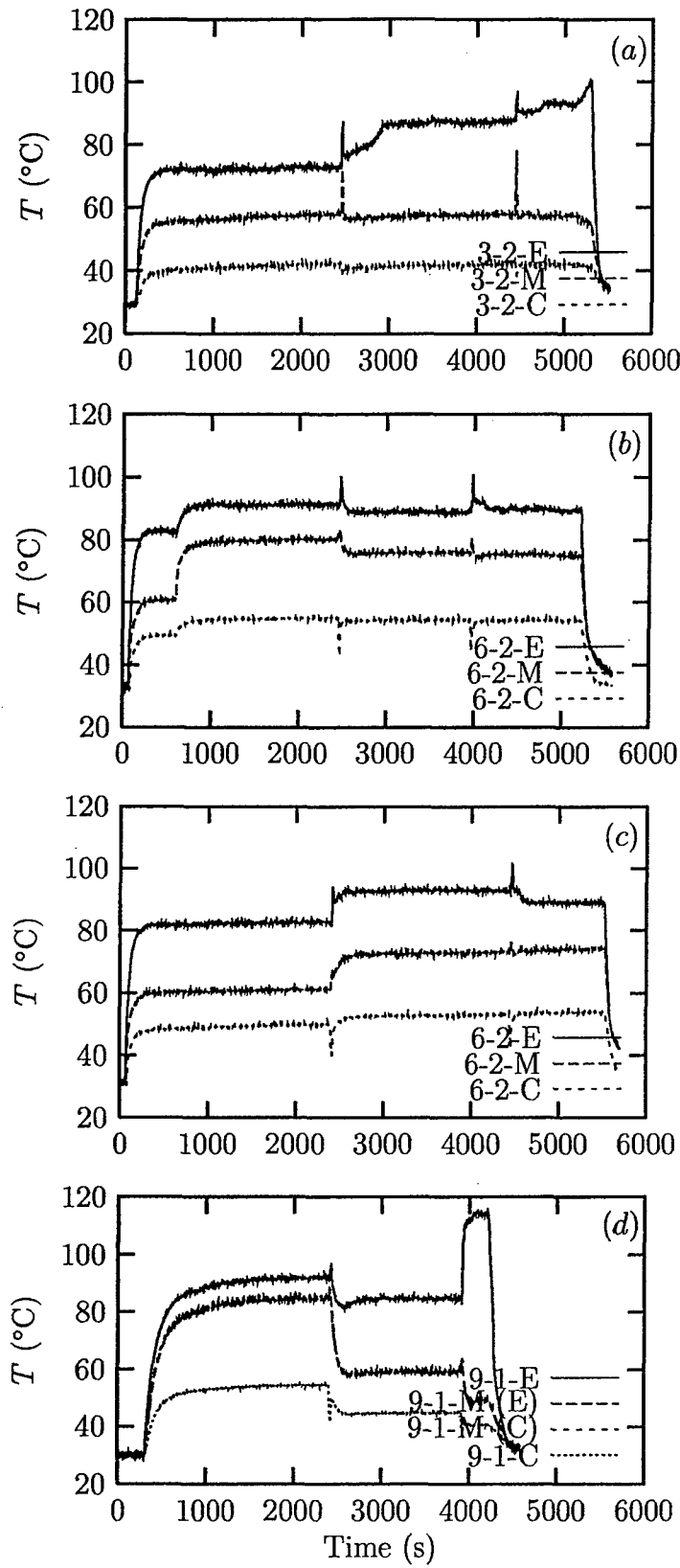


Figure 55: Typical burst test results for $a_r = 5.0\text{-g}$: (a) 3IHP (RAY28); (b) 6IHP (RAY16); (c) 6IHP (RAY17); (d) 9IHP (RAY2).

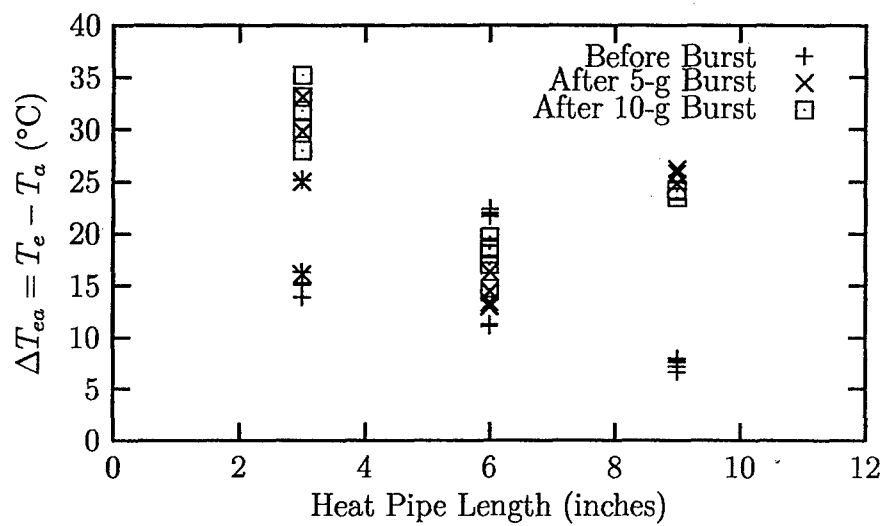


Figure 56: Temperature differences between the evaporator and adiabatic sections for the burst tests.

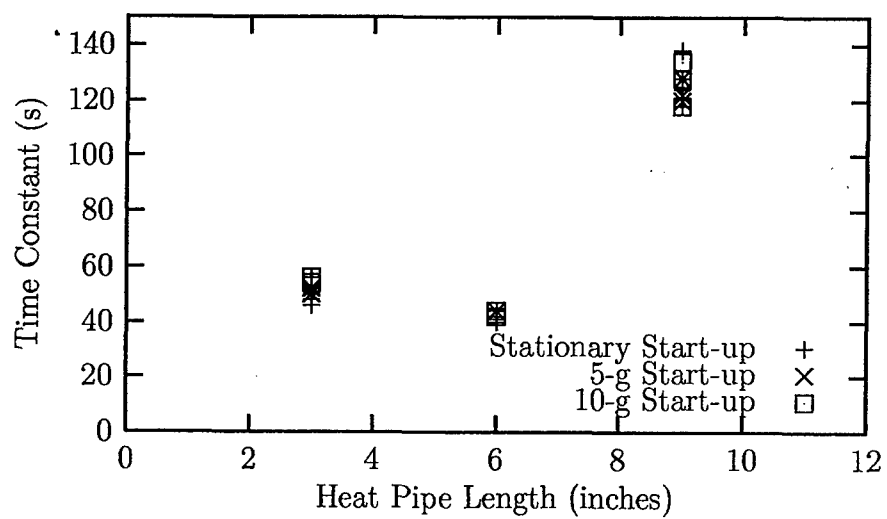


Figure 57: Start-up response characteristics.

Table 14: Temperature differences between the evaporator and adiabatic sections for the start-up tests (Fig. 54).

Heat Pipe Length (inches)	ΔT_{ea} (°C)	
	$a_r = 5.0\text{-g}$	$a_r = 10.0\text{-g}$
3	14.4	13.7
3	15.2	13.7
3	13.9	14.8
6	9.6	9.8
6	10.0	9.2
6	9.6	10.2
9	22.7	20.8
9	23.1	24.7
9	24.5	27.0

Table 15: Temperature differences between the evaporator and adiabatic sections for the burst tests (Fig. 56).

Heat Pipe Length (inches)	ΔT_{ea} (°C)		
	Before Burst	After 5.0-g Burst	After 10.0-g Burst
3	25.2	25.0	x
3	16.3	16.1	x
3	15.1	29.8	x
3	15.2	x	35.2
3	13.9	x	31.8
3	15.3	x	30.1
3	x	29.8	x
3	x	33.1	x
3	x	x	33.1
3	x	x	28.0
6	11.3	13.0	x
6	21.7	14.4	x
6	11.1	13.1	x
6	21.9	x	19.7
6	22.0	x	18.5
6	22.4	x	18.7
6	x	13.4	x
6	x	16.3	x
6	x	14.5	x
6	x	x	14.7
6	x	x	18.0
6	x	x	17.0
9	6.6	24.8	x
9	7.2	25.8	x
9	7.6	26.2	x
9	7.7	x	24.2
9	8.0	x	23.5
9	7.9	x	24.1

Table 16: Start-up response characteristics (Fig. 57).

Heat Pipe Length (inches)	Start-Up Time Constant (s)		
	Stationary	$a_r = 5.0\text{-g}$	$a_r = 10.0\text{-g}$
3	x	50	x
3	52	52	x
3	50	52	x
3	56	x	54
3	48	x	54
3	46	x	56
6	x	44	x
6	44	44	x
6	40	44	x
6	42	x	42
6	40	x	44
6	42	x	44
9	x	122	x
9	138	120	x
9	124	128	x
9	128	x	134
9	118	x	118
9	118	x	128